

# Many-body effects on dense matter with hyperons at finite temperature

Rafael Bán Jacobsen,<sup>1,2</sup> Ricardo Luciano Sonego Farias,<sup>1,2</sup> and Veronica Dexheimer<sup>2</sup>

<sup>1</sup>Departamento de Física, Universidade Federal de Santa Maria, 97105-900 Santa Maria, RS, Brazil

<sup>2</sup>Center for Nuclear Research, Department of Physics, Kent State University, Kent, OH 44242 USA

(Dated: February 9, 2026)

In this work, we present the first extension of the Many-Body Forces (MBF) Model to finite temperature. The MBF Model describes nuclear matter in a relativistic quantum hadrodynamics formalism that takes many-body forces into account through a field dependence of the nuclear interaction coupling constants. Assuming nuclear matter to be charge neutral, beta-equilibrated, and populated by the baryon octet, electrons, and muons, we explore the parameters of the model, three different hyperon coupling schemes (also introduced here for the first time in MBF), and temperature effects to describe basic properties of nuclear matter, including the speed of sound, compressibility, and adiabatic index. We also investigate the mass-radius relation of compact stars by solving the Tolman-Oppenheimer-Volkoff equations at zero and finite temperature, including scenarios with fixed entropy per baryon. Our original results at finite temperature open the path to a new description of proto-neutron stars.

## I. INTRODUCTION

### A. The search for the nuclear matter EoS

Advances in high-energy physics and astrophysics in recent years have made it possible to investigate the behavior of matter under increasingly extreme conditions with unprecedented detail. The study of new states of matter, generated under ever increasing conditions of temperature and density, is considered one of the great challenges of current physics and involves theoretical and phenomenological aspects of nuclear physics, particle physics, astronomy and astrophysics.

Currently, with the knowledge of the existence of *quarks* [1, 2], the nuclear force is considered a residue of the strong interaction between them. This interaction is mediated by *gluons* and described by *quantum chromodynamics* (QCD), a theory that describes the most essential aspects of the interaction between quarks and is therefore considered the fundamental theory of the strong interaction. For this reason, QCD provides the formalism to describe the behavior of matter in the most diverse regimes of density and temperature.

According to QCD, hadrons (baryons and mesons) are considered to be composed of quarks and antiquarks, which interact by exchanging gluons. Since the nucleus is composed of protons and neutrons (which are baryons especially called *nucleons*), it would be natural to attempt a description of nuclear matter from QCD. However, this theory is quite complex. When one tries to describe the nucleus, a many-body system, from the degrees of freedom of the elementary quarks “embedded” in composite particles (nucleons), one obtains a set of highly coupled equations which is practically intractable from a mathematical point of view. QCD calculations, in most cases, involve the use of high-performance computers, mainly for the study of lattice QCD [3]. Furthermore, current lattice QCD calculations have difficulty reaching the high-density regime due to the highly os-

cillatory behavior in the functional integral; in fact, the path integrals for the fermionic fields written from the Lagrangian density of QCD will have real values only for zero or purely imaginary chemical potentials, making it impossible to perform direct simulations of lattice QCD in the finite density regime – this is the well-known *sign problem of lattice QCD* [4, 5]. Hence, it is not possible to describe the equation of state (EoS) of dense and strongly interacting matter at a fundamental level. An exception are the limits in which it is possible to study QCD using perturbation theory, a methodology known as *PQCD* (from *perturbative QCD*) [6]. The PQCD approach can be adopted to investigate different regions of the phase diagram, such as very high temperature and low chemical potential [7] or very high chemical potential and low temperature [8].

However, it is not necessary to use a theory as fundamental as QCD to coherently describe the properties of nuclear matter, since, in this case, the system to be studied is located in a restricted region of the QCD phase diagram, corresponding to lower densities and temperatures (when compared to the regime where quarks are expected to be deconfined). Just as, for example, in the study of atoms and molecules there is no relevance in including the internal structure of the nucleus or even of electrons that are outside the valence shell, it is not relevant, for studies of nuclear matter, to take into account more fundamental degrees of freedom, since they do not necessarily interfere in the results. As a matter of fact, at the nuclear energy scale (MeV), the important degrees of freedom are those of the hadrons.

Therefore, alternatives to QCD were sought for the study of nuclear matter. In this context, models called *effective theories* emerged. In 1974, John Dirk Walecka, following the work of Johnson and Teller [9] and Duerr [10], proposed an effective theory of nuclear fields, capable of describing nuclear matter in a region of the energy spectrum in which the degrees of freedom of the quarks do not present a significant contribution. This is a *relativistic mean-field theory* (RMF), based on a formulation

by Yukawa [11], in which nucleons are considered to interact through the exchange of scalar mesons (called  $\sigma$ ) and vector mesons (called  $\omega$ ), without explicitly considering the presence of quarks. Scalar mesons are responsible for long-range attraction (attractive component of the strong nuclear force), and vector mesons are responsible for short-range repulsion (repulsive component of the strong nuclear force). This model is known as the *Walecka Model* or  $\sigma$ - $\omega$  model or *QHD Model* (from *quantum hadrodynamics*) [12].

In the effective theories considered in this work, the term *effective* is used to convey that the baryon and meson fields are treated as fundamental fields, without taking into account, as already mentioned, the presence of quarks in their interior. These fields are then called *effective*. Furthermore, in such theories, the interaction is mediated by the meson fields, which are also effective, without taking into account the presence of gluons, and is therefore an effective interaction characterized by effective coupling constants. These constants must be such that the theory can reproduce basic nuclear properties, such as the binding energy of the nucleus and its saturation density. As an effective theory, Walecka Model presents many results consistent with phenomenology [13]; however, some nuclear properties are overestimated, such as the compressibility of nuclear matter, and others are underestimated, such as the effective mass of the nucleon in the medium.

In order to correct these deficiencies, other effective models have emerged in the literature, such as the *Non-linear Boguta-Bodmer Model* [14], which introduces self-coupling terms of the scalar meson, and the *Zimanyi and Moszkowski Model*, the *ZM Model* [15], which replaces the minimal Yukawa coupling between the scalar meson and the nucleon (where coupling appears in the Lagrangian density as a simple product of fields) by a derivative-type coupling, in which the scalar meson couples to the nucleon field through its derivative terms. From a physical standpoint, the key distinction is that the minimal Yukawa coupling introduces a linear response of the baryon effective mass to the scalar field, while the derivative coupling yields a nonlinear, saturating behavior [16]. The latter tends to soften the scalar attraction at high densities and is often used to mimic many-body correlations that would otherwise need to be introduced explicitly.

Another model that follows the same philosophy is the *Many-Body Forces Model* (MBF Model) [17, 18]. From a formal point of view, the special feature of this model consists in a generalization of the effective models previously developed, considering a parameterizable derivative coupling that simulates many-body forces. The MBF Model is the one to be adopted in this work and its complete formalism will be presented in Section II.

Nonetheless, the exact behavior of the EoS of nuclear matter at high densities is still largely unknown, since PQCD provides the EoS only for densities above approximately forty times the saturation density at low tem-

perature [8]. However, nature itself provides us with observatories to test our understanding of nuclear matter under extreme conditions. The interior of a neutron star (NS) offers a unique meeting point between astrophysics and nuclear physics, since the macroscopic properties of NSs, such as mass, radius and thermal evolution, depend on the microscopic nature of matter at high densities.

## B. Neutron stars as astrophysical labs

NSs are formed during the collapse of the cores of massive stars ( $8 \text{ M}_{\text{Sun}} \lesssim M \lesssim 25 \text{ M}_{\text{Sun}}$ ), when there is not enough thermonuclear energy to sustain the mass of the star beyond the core. This core, consisting mainly of  $Fe^{56}$  nuclei, undergoes gravitational collapse, causing its interior to reach high densities. When the baryon degeneracy pressure of the collapsing core becomes equivalent to the gravitational pressure, the outer layers of the star are ejected in a supernova explosion. Due to the conservation of magnetic flux and angular momentum during the collapse, the remnant has extremely strong magnetic fields and rapid rotation [19–21]. The compact object thus formed, called a *proto-neutron star* (PNS), is hot, reaching temperatures of tens of MeV ( $\sim 10^{11}$ K), but is quickly cooled through the emission of photons from its surface and neutrinos from its interior [22]. Finally, as the star loses energy over the years, its rotation rate slows down until these objects become fully evolved NSs, with temperatures on the order of 1 MeV ( $\sim 10^{10}$ K). Such objects typically have masses within the range  $1 - 2 \text{ M}_{\text{Sun}}$ , but some estimates indicate that their maximum mass can reach  $M_{\text{max}} = 2.3 \text{ M}_{\text{Sun}}$ , with radii of the order of  $10 - 13$  km [23], resulting in average densities of  $7 \times 10^{14} \text{ g/cm}^3$ , which corresponds, approximately, to the saturation density of nuclear matter  $n_0 = 0.15 \text{ fm}^{-3}$ . For comparison, this is the value of the density of nuclear matter inside a massive nucleus such as  $Pb^{208}$ . In the innermost layers of these compact objects, evidently, the density can reach significantly higher values.

NSs and PNSs are, in this sense, cosmic laboratories for the physics of supranuclear densities: the nuclear matter contained in them is excellently suited to the study proposed by effective theories, since these objects are found at relatively low temperatures ( $T \lesssim 30$  MeV) and high chemical potentials ( $\mu \gtrsim 900$  MeV). More precisely, three main reasons for the applicability of effective models to the study of NSs should be highlighted. First: as already mentioned, NSs are extremely compact objects, with densities of the order of magnitude of  $\sim 10^{15} \text{ g/cm}^3$ , composed of an estimated total of  $10^{57}$  neutrons ( $\sim 80\%$  of their composition); Therefore, the nuclear matter contained in these stars adapts admirably to the study proposed by effective theories, in which the definition of nuclear matter presupposes an infinite number of nucleons. Second: in QHD models, the formalism is covariant and, therefore, causality is intrinsically respected (as long as the vector interactions are not extremely strong). Third:

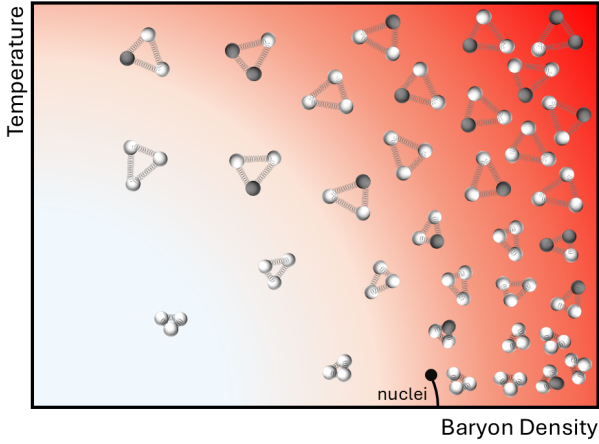


FIG. 1. Schematic representation of the low/high-baryon-density and low/medium-temperature sector of the QCD phase diagram, where strongly interacting matter is dominated by baryonic degrees of freedom. Light quarks ( $u$  and  $d$ ) are shown in white, such that ordinary nucleons are depicted as bound triplets of three white circles. The onset of strangeness is illustrated through the appearance of strange quarks ( $s$ ), represented in gray; hyperons are therefore indicated as composite states containing one or two gray circles in combination with the light-quark constituents. The background red gradient points toward increasing energy scale.

the mean-field approximation used in the Walecka Model and similar models is more valid the higher the particle density (and, in the case of NSs and PNSs, this condition is fully satisfied).

Despite the current use of the indistinct nomenclature *neutron stars* for such objects, it should be emphasized that their structure is not composed exclusively of neutrons – and, in fact, NSs can have different compositions, depending on the model adopted. These are the possible compositions mostly explored in the literature, as well as some of the pioneering works on such descriptions: (i) exclusively nucleons (protons and neutrons), electrons and muons [24]; (ii) nucleons, electrons and muons and a core containing a pion condensate [25]; (iii) nucleons, electrons and muons, and a core containing a kaon condensate [26]; (iv) nucleons, hyperons (baryons of non-zero strangeness), electrons and muons [27, 28]; (v) nucleons, hyperons, electrons and muons and a core containing quark matter (deconfined  $u$ ,  $d$  and  $s$  quarks) [29]; (vi) exclusively deconfined quark matter [30].

The different possibilities for the internal composition of NSs suggest that different phases of QCD are eligible as constituents of these objects. In the present work, we will investigate the scenarios described in (i) and (iv), which are illustrated in Fig. 1.

Fig. 1 shows the region of the QCD phase diagram corresponding to low/high baryon density and low/medium temperature. At low baryon densities and low temperatures, the QCD phase diagram is governed by hadronic degrees of freedom, with matter composed primarily of

nucleons (composed only of  $u$  and  $d$  quarks, represented in white). In this regime, thermal agitation is insufficient to create a significant amount of thermal mesons and free quarks, and the baryon chemical potential is assumed to not reach the threshold for deconfinement, still unknown [31]. Nonetheless, even in this relatively cold and dilute sector, heavier baryons such as hyperons (baryons which contain one or more  $s$  quarks, represented in grey) can begin to appear if density or temperature increases enough to make their formation energetically favorable. As the baryon chemical potential rises, the threshold for producing strange baryons is crossed, allowing the system to populate states containing strange quarks in order to minimize its free energy. Similarly, modest thermal effects can contribute to populating heavier baryonic states, enabling the occasional emergence of hyperons even before the system reaches the high-density core-collapse or neutron-star-interior regime. Thus, the low/high-density, low/medium-temperature corner of the QCD diagram still hints at the rich structure of baryonic matter and the onset of strangeness under appropriate thermodynamic conditions.

In spite of the exact internal composition of NSs and PNSs, there are some conditions that such objects must obey. Among them, for the discussion that will be developed in this work, three stand out: conservation of baryon density, neutrality of electric charge, and chemical equilibrium. Regarding the first aspect, it is simply a matter of saying that, by adding the baryon (number) densities  $n_{B_j}$  of the different types of baryons  $b$  present in the system, the total baryon (number) density  $n_B$  is obtained:

$$\sum_{j=b} n_{B_j} - n_B = 0, \quad (1)$$

where  $n_{B_j} = \mathcal{B}_j n_j$ , with  $\mathcal{B}_j$  being the baryon number (1 for baryons, 0 for leptons) and  $n_j$  the number density of each particle.

Regarding the second aspect, NSs must be electrically neutral, due to the disproportionate relation between the strength of gravitational and electromagnetic forces. In order to demonstrate this fact, consider an electrically charged particle located on the surface of the also charged star. This particle will therefore suffer gravitational attraction and the action of the electromagnetic force. Assuming that the sign of the net charge of the star is the same as that of the particle, it follows that the gravitational component must overcome the electrical repulsion so that the particle is not expelled from the star. Following a simple calculation [32], this results in  $Z_{\text{net}}/A \sim 10^{-36}$ , where  $Z_{\text{net}}$  is the net charge of the star (in units of the elementary charge), and  $A$  is the total number of baryons in the star. A fraction between  $Z_{\text{net}}$  and  $A$  greater than this value expels the test particle from the star. Thus, it is verified that the net charge per nucleon is practically zero. In short, this condition can

be expressed as:

$$\sum_{j=l} \mathcal{Q}_j n_{l_j} + \sum_{j=b} \mathcal{Q}_j n_{B_j} = 0 \quad (2)$$

where  $\mathcal{Q}_j$  denotes the electric charge of each lepton species  $l$  and each baryon species  $b$  present in the system (in units of the elementary charge),  $n_{l_j} = \mathcal{L}_j n_j$  is the lepton (number) density, being  $\mathcal{L}_j$  the lepton number (0 for baryons and 1 for leptons).

Regarding the third aspect, it is important to remember that systems in which reactions occur (whether chemical or nuclear) are governed by equilibrium laws given by thermodynamics. Chemical equilibrium is established when the fractions of the constituents  $j$  of the reaction stabilize, which is described by their chemical potentials  $\mu_j$ . The chemical potential is related to the increase in energy of the system when a new particle is added to it, and chemical equilibrium is a way of ensuring that, starting from the reactions pertinent to the problem analyzed, the system will reach a state of thermodynamic stability in which the energy levels will be filled in such a way as to minimize the energy. In a situation of chemical equilibrium, the number of each type of particle is not conserved, since they are created and annihilated according to the reactions considered. In fact, in the evolution of a star from the condition of a PNS to becoming a NS and beyond, several reactions can occur. It can be mentioned, initially, that, moments after the supernova explosion or even during it, the nucleons have such a high momentum that their Fermi energy exceeds the mass value of some hyperons, allowing these particles to be formed.

In addition to the hyperon formation and decay reactions, it is also possible to cite as an example beta decay and inverse beta decay, which establish how protons and neutrons transmute into each other (beta-equilibrium), consisting of reactions of great importance for understanding the properties of nuclear matter and NSs. Although there are many possible reactions that occur in nuclear matter at high densities, it is not necessary to discuss all of them individually to establish the conditions of beta-equilibrium; in fact, the chemical equilibrium equations can be written in terms of a small number of chemical potentials, related to the number of quantities conserved in the system:

$$\mu_j = \mathcal{B}_j \mu_B + \mathcal{Q}_j (\mu_q + \mu_l) + \mathcal{L}_j \mu_l, \quad (3)$$

where  $\mu_j$  is the chemical potential of a given particle species  $j$  present in the system, and  $\mu_B$ ,  $\mu_q$  and  $\mu_l$  are, respectively, the baryon chemical potential, the charged chemical potential and the lepton chemical potential. Equation (3) properly expresses the conditions for beta-equilibrium if one considers that both baryons and leptons follow its prescription. Note that equation (3) is valid for both NSs and PNSs, with the caveat that the lepton chemical potential is non-zero only when the lepton fraction is fixed (since neutrinos cannot escape). If strangeness were conserved, like in the case of the ini-

tial stages of a heavy ion collision, a strange chemical potential  $\mu_S$  would have to be introduced.

Focusing on the recent advances in the observation of NSs, data obtained by NASA's NICER mission have allowed, for the first time, a reliable measurement of the radius of these stars [33, 34], while the LIGO and Virgo interferometers have provided a measure of the tidal deformability of NSs [35] and a consequent estimate of their maximum mass [36]. Consequently, existing models for the interior of NSs that were not compatible with the new results have been severely restricted, modified or even abandoned. On the other hand, advances in the understanding of supernova explosions and NS mergers (recently measured by LIGO and Virgo) have started to call for descriptions of dense matter that include temperature effects. Old prescriptions that included *ad hoc* temperature effects became problematic because they do not allow the composition of matter to vary with temperature (see again Fig. 1), which can generate large discrepancies. In this context, the present work aims to provide a comprehensive description of nuclear matter inside compact stars that beyond zero-temperature approximation.

## II. THE MANY-BODY FORCES (MBF) MODEL

### A. General formalism

Inspired by previous efforts to expand the ZM Model [16, 37], the effective model for nuclear matter proposed by Taurines and collaborators [17, 18] is a parametric derivative coupling model in which the coupling constants of this model are dependent on the meson fields – and indirectly on the density of nuclear matter –, thus contemplating contributions from many-body interactions, as will be clear below. For this reason, this model became known in the literature as *MBF Model* (from the expression *many-body forces*).

In the MBF Model, the coupling between mesons and baryons is directly dependent on the scalar fields, and parameterized in such a way as to reproduce the case of minimal coupling (as in the Walecka Model [12]), derivative coupling (as in the ZM Model [15]), and infinite new forms of couplings that depend on the chosen parameterization. The model has been applied to a wide range of problems, in particular in studies of the density-dependence of the compressibility of nuclear matter [38], hyperonic matter at high densities [39], phase transition to deconfined quark matter [40], and many-body forces in magnetic neutron stars [41].

The most complete version of the MBF Model [39] includes eight baryon fields ( $\psi_b$ ) coupled to six meson fields ( $\sigma$ ,  $\omega$ ,  $\rho$ ,  $\delta$ ,  $\phi$  and  $\sigma^*$ ) plus free lepton fields ( $\psi_l$ ). The  $\delta$  meson is introduced in order to better describe the properties of asymmetric matter, while the strange mesons ( $\sigma^*$ ,  $\phi$ ) have important impact on hyperon interactions.

In the natural system of units, where  $\hbar = c = k_B =$

TABLE I. Properties of baryons and leptons included in the MBF Model. The lines present the different particles and  $I^3$ ,  $\mathcal{B}$ ,  $\mathcal{L}$ ,  $\mathcal{Q}$  and  $\mathcal{S}$  and stand for the isospin projection in the  $z$  direction, baryon number, lepton number, electric charge (in units of the elementary charge) and strangeness, respectively. The masses follow the values provided by the *Particle Data Group (PDG)* [42], rounded to four significant digits.

particle	mass (MeV)	$I^3$	$\mathcal{B}$	$\mathcal{L}$	$\mathcal{Q}$	$\mathcal{S}$
$p$	939.6	$1/2$	1	0	+1	0
$n$	938.3	$-1/2$	1	0	0	0
$\Lambda^0$	1116	0	1	0	0	-1
$\Sigma^+$	1189	$+1$	1	0	+1	-1
$\Sigma^0$	1193	0	1	0	0	-1
$\Sigma^-$	1197	$-1$	1	0	-1	-1
$\Xi^0$	1315	$+1/2$	1	0	0	-2
$\Xi^-$	1322	$-1/2$	1	0	-1	-2
$e^-$	0.5110	0	0	1	-1	0
$\mu^-$	105.7	0	0	1	-1	0

1, the Lagrangian density for the MBF Model can be written as follows:

$$\begin{aligned} \mathcal{L} = & \sum_b \bar{\psi}_b \left[ \gamma_\mu \left( i\partial^\mu - g_{\omega b \xi}^* \omega^\mu - g_{\phi b \kappa}^* \phi^\mu - \frac{1}{2} g_{\varrho b \eta}^* \boldsymbol{\tau} \cdot \boldsymbol{\varrho}^\mu \right) \right. \\ & - \left( m_b - g_{\sigma b \zeta}^* \sigma - g_{\sigma^* b \zeta}^* \sigma^* - \frac{1}{2} g_{\delta b \zeta}^* \boldsymbol{\tau} \cdot \boldsymbol{\delta} \right) \left. \psi_b \right] \\ & + \left( \frac{1}{2} \partial_\mu \sigma \partial^\mu \sigma - m_\sigma^2 \sigma^2 \right) + \left( \frac{1}{2} \partial_\mu \sigma^* \partial^\mu \sigma^* - m_{\sigma^*}^2 \sigma^{*2} \right) \\ & + \left( -\frac{1}{16\pi} \omega_{\mu\nu} \omega^{\mu\nu} + \frac{1}{8\pi} m_\omega^2 \omega_\mu \omega^\mu \right) \\ & + \left( -\frac{1}{16\pi} \phi_{\mu\nu} \phi^{\mu\nu} + \frac{1}{8\pi} m_\phi^2 \phi_\mu \phi^\mu \right) \\ & + \left( -\frac{1}{16\pi} \varrho_{\mu\nu} \cdot \varrho^{\mu\nu} + \frac{1}{8\pi} m_\varrho^2 \varrho_\mu \cdot \varrho^\mu \right) \\ & + \left( \frac{1}{2} \partial_\mu \boldsymbol{\delta} \cdot \partial^\mu \boldsymbol{\delta} - m_\delta^2 \boldsymbol{\delta}^2 \right) + \sum_l \bar{\psi}_l \gamma_\mu (i\partial^\mu - m_l) \psi_l, \end{aligned} \quad (4)$$

where  $\omega_{\mu\nu} = \partial_\mu \omega_\nu - \partial_\nu \omega_\mu$ ,  $\varrho_{\mu\nu} = \partial_\mu \varrho_\nu - \partial_\nu \varrho_\mu$  and  $\phi_{\mu\nu} = \partial_\mu \phi_\nu - \partial_\nu \phi_\mu$ , and the operators  $\boldsymbol{\tau} = (\tau_1, \tau_2, \tau_3)$  denote the Pauli isospin matrices. Moreover, the subscripts  $b$  and  $l$  label, respectively, the baryon octet ( $n, p, \Lambda^0, \Sigma^-, \Sigma^0, \Sigma^+, \Xi^-, \Xi^0$ ) and lepton ( $e^-, \mu^-$ ) degrees of freedom.

In equation (4), the first and last terms represent the Dirac Lagrangian density for baryons and leptons, respectively. The other terms represent the Lagrangian densities of mesons, adopting a Klein-Gordon Lagrangian density for the scalar fields  $\sigma, \delta$  and  $\sigma^*$  and a Proca Lagrangian density for the vector fields  $\omega, \varrho$  and  $\phi$ . The meson-baryon coupling is introduced by the coupling constants  $g^*$  present in the first term of the equation (4).

More precisely, the (scalar) fields  $\sigma$  and  $\sigma^*$  couple to the scalar density  $\bar{\psi}_b \gamma_\mu \psi_b$ , and the (isovector) fields

TABLE II. Meson fields in the MBF Model. Particle nomenclatures follow the *PDG* [42]. The masses of the five heavier mesons shown in this table follow the *PDG* average or estimate values, truncated in the units place. Since *PDG* does not provide an average or estimate value for the mass of  $\sigma$ , we adopt the upper value in the range provided by this same reference, which is in accordance with [43].

meson	particle	classification	coupling constant	mass (MeV)
$\sigma$	$f_0(500)$	scalar-isoscalar	$g_{\sigma b}$	550
$\boldsymbol{\delta}$	$a_0(980)$	scalar-isovector	$g_{\delta b}$	980
$\omega_\mu$	$\omega(782)$	vector-isoscalar	$g_{\omega b}$	783
$\varrho_\mu$	$\varrho(770)$	vector-isovector	$g_{\varrho b}$	775
$\sigma^*$	$f_0(980)$	scalar-isoscalar	$g_{\sigma^* b}$	990
$\phi_\mu$	$\phi(1020)$	vector-isoscalar	$g_{\phi b}$	1019

$\boldsymbol{\varrho}^\mu$  and  $\boldsymbol{\delta}$  introduce isospin asymmetry, coupling, respectively, to the isospin current  $\frac{1}{2} \bar{\psi}_b \boldsymbol{\tau} \gamma_\mu \psi_b$  and to the scalar-isovector density  $\bar{\psi}_b \boldsymbol{\tau} \psi_b$ . The properties of all the particles included in the formalism are shown in Table I, and the meson fields are listed in Table II.

The general definition of the meson-baryon couplings is:

$$\begin{aligned} g_{\sigma b \zeta}^* &\equiv \Pi_{\zeta b} g_{\sigma b}, & g_{\sigma^* b \zeta}^* &\equiv \Pi_{\zeta b} g_{\sigma^* b}, & g_{\delta b \zeta}^* &\equiv \Pi_{\zeta b} g_{\delta b}, \\ g_{\omega b \xi}^* &\equiv \Pi_{\xi b} g_{\omega b}, & g_{\varrho b \kappa}^* &\equiv \Pi_{\kappa b} g_{\varrho b}, & g_{\phi b \eta}^* &\equiv \Pi_{\eta b} g_{\phi b}, \end{aligned} \quad (5)$$

where the parametric term  $\Pi_{\lambda b}$  introduces the nonlinear contributions that define the MBF Model:

$$\Pi_{\lambda b} \equiv \left( 1 + \frac{g_{\sigma b} \sigma + g_{\sigma^* b} \sigma^* + \frac{1}{2} g_{\delta b} \boldsymbol{\tau} \cdot \boldsymbol{\delta}}{\lambda m_b} \right)^{-\lambda}, \quad (6)$$

for  $\lambda = \xi, \kappa, \eta, \zeta$ .

In agreement with the Lagrangian density (4), the effective mass of baryons  $m_b^*$  is defined as:

$$m_b^* = m_b - \Pi_{\zeta b} \left( g_{\sigma b} \sigma + g_{\sigma^* b} \sigma^* + \frac{1}{2} g_{\delta b} \boldsymbol{\tau} \cdot \boldsymbol{\delta} \right). \quad (7)$$

In expression (6),  $\lambda$  is an adjustable parameter that can assume different values  $\xi, \kappa, \eta$  or  $\zeta$  to regulate the intensity of such coupling for  $\omega, \varrho, \phi$  or the scalar mesons, respectively. From expressions (5) and (6) it can be seen that the coupling constants of the model depend on the scalar fields and, since these fields vary as a function of density according to their equations of motion, the couplings have an indirect density dependence. In short, the MBF Model presents *adjustable meson-nucleon couplings*. This type of adjustable coupling provides a great freedom of choice, since we can vary the indices  $\xi, \kappa, \eta$  or  $\zeta$  continuously to obtain different values for the relevant physical quantities.

The range of relevant values for these parameters is not as large as one might initially guess. Due to the

TABLE III. Nomenclature for the standard parameterizations of the MBF Model. S: scalar version; V: vector version; SVIS: scalar-vector-isoscalar version; SVIV: scalar-vector-isovector version.

model	$\zeta$	$\xi$	$\kappa$	$\eta$
S	$\neq 0$	$= 0$	$= 0$	$= 0$
V	$\neq 0$	$\neq 0$	$= 0$	$= 0$
SVIS	$\neq 0$	$\neq 0$	$\neq 0$	$= 0$
SVIV	$\neq 0$	$\neq 0$	$\neq 0$	$\neq 0$

general form of the couplings, presented in (6), there is a rapid convergence to an exponential form of coupling. In order to verify this fact, it suffices to let the adjustable parameters tend to infinity ( $\lambda \rightarrow \infty$ ):

$$\begin{aligned} \lim_{\lambda \rightarrow \infty} \Pi_{\lambda b} &= \lim_{\lambda \rightarrow \infty} \left( 1 + \frac{g_{\sigma b} \sigma + g_{\sigma^* b} \sigma^* + \frac{1}{2} g_{\delta b} \boldsymbol{\tau} \cdot \boldsymbol{\delta}}{\lambda m_b} \right)^{-\lambda} \\ &= \lim_{\lambda \rightarrow \infty} \left( 1 + \frac{x}{\lambda} \right)^{-\lambda} = e^{-x}, \end{aligned} \quad (8)$$

where we have defined

$$x \equiv (g_{\sigma b} \sigma + g_{\sigma^* b} \sigma^* + \frac{1}{2} g_{\delta b} \boldsymbol{\tau} \cdot \boldsymbol{\delta}) / m_b. \quad (9)$$

Given that sufficiently small values for  $\lambda$  can be chosen, it is possible to carry out the explicit binomial expansion of the parametric term  $\Pi_{\lambda b}$  in the following way:

$$\begin{aligned} \Pi_{\lambda b} &= 1 - \left( \frac{g_{\sigma b} \sigma + g_{\sigma^* b} \sigma^* + \frac{1}{2} g_{\delta b} \boldsymbol{\tau} \cdot \boldsymbol{\delta}}{m_b} \right) \\ &+ \frac{(\lambda + 1)}{2! \lambda} \left( \frac{g_{\sigma b} \sigma + g_{\sigma^* b} \sigma^* + \frac{1}{2} g_{\delta b} \boldsymbol{\tau} \cdot \boldsymbol{\delta}}{m_b} \right)^2 \\ &- \frac{(\lambda^2 + 3\lambda + 2)}{3! \lambda^2} \left( \frac{g_{\sigma b} \sigma + g_{\sigma^* b} \sigma^* + \frac{1}{2} g_{\delta b} \boldsymbol{\tau} \cdot \boldsymbol{\delta}}{m_b} \right)^3 + \dots \end{aligned} \quad (10)$$

The crossed terms, of order higher than one, are be interpreted as many-body contributions. Important to emphasize, however, that  $\lambda$  does not need to be small, and different  $\lambda$  values can be seen as producing *different models*, although we conservatively refer to these as *different parameterizations* or *different versions*. See Appendix for a detailed discussion of how the MBF Model reduces to the Walecka and ZM models.

The dependence of the many-body interactions is introduced in the meson-baryon couplings through the parameters  $\xi$ ,  $\kappa$ ,  $\eta$  or  $\zeta$ , which will define the character of the many-body contribution to each meson field. Thus, in the MBF formalism, the parameter space to be investigated is expanded. To reduce the number of parameters to be studied, we restrict ourselves to the standard parameterizations of the MBF Model, as summarized in Table III.

Most of the literature on the MBF Model has focused on the scalar (S) and scalar-vector-isoscalar (SVE) parameterizations, and in the latter case, the constraint  $\zeta = \xi = \kappa$  has commonly been adopted [17, 18]. However, the majority of works have focused on the scalar version (S) of the MBF Model [39], since it has presented more consistent results for both the properties of nuclear matter and the masses and radii of NSs. For this reason, in order to allow a comparison of the effects of including temperature in the MBF Model (something unprecedented until now) with most of the results already obtained for this model, the present work will henceforth explore only the S version of the MBF Model.

Therefore, from this point on, adopting the scalar version (S) of the MBF Model, the equations are controlled by a single adjustable parameter ( $\zeta$ ). In this scenario, the general definition of the meson-baryon couplings is:

$$\begin{aligned} g_{\sigma b \zeta}^* &\equiv \Pi_{\zeta b} g_{\sigma b}, & g_{\sigma^* b \zeta}^* &\equiv \Pi_{\zeta b} g_{\sigma^* b}, & g_{\delta b \zeta}^* &\equiv \Pi_{\zeta b} g_{\delta b}, \\ g_{\omega b \xi}^* &\equiv g_{\omega b}, & g_{\varrho b \kappa}^* &\equiv g_{\varrho b}, & g_{\phi b \eta}^* &\equiv g_{\phi b}. \end{aligned} \quad (11)$$

Since the meson-baryon couplings depend on the scalar meson fields, and since these fields, in turn, depend on density, it is possible to say that the MBF Model is implicitly density-dependent. For this reason, the MBF Model exhibits all the advantages inherent in density-dependent relativistic models for nuclear matter (the density dependence mimics medium effects seen in microscopic many-body calculations, reproduces empirical saturation without *ad hoc* nonlinear meson terms, and provides more flexibility to fit neutron-rich matter properties and astrophysical constraints), with the added benefit of not requiring the usual rearrangement terms that must be included for thermodynamic consistency when the coupling constants are explicit functions of the baryon density (see, e.g., [44–48]).

## B. Equations of motion and mean-field approximation

The equations of motion for the meson and baryon fields can be obtained by the Euler-Lagrange equations from the Lagrangian density of the model (4). For the field  $\sigma$ , it follows that

$$\begin{aligned} (\partial_\mu \partial^\mu + m_\sigma^2) \sigma &= \sum_b \bar{\psi}_b \left[ g_{\sigma b} (\Pi_{\zeta b}) - \frac{g_{\sigma b}}{m_b} (\Pi_{\zeta b})^{\frac{\zeta+1}{\zeta}} \times \right. \\ &\quad \left. \times \left( g_{\sigma b} + \frac{1}{2} g_{\delta b} \boldsymbol{\tau} \cdot \boldsymbol{\delta} + g_{\sigma^* b} \sigma^* \right) \right] \psi_b, \end{aligned} \quad (12)$$

which is a Klein-Gordon equation with a scalar source related to the derivative coupling. For the field  $\omega$ , we obtain

$$-\partial^\mu \omega_{\mu\nu} + m_\omega^2 \omega_\mu = \sum_b g_{\omega b} \bar{\psi}_b \gamma_\mu \psi_b, \quad (13)$$

which is a Proca equation, whose source is given by the baryon four-current  $j_\mu = \bar{\psi}_b \gamma_\mu \psi_b$ . For the field  $\boldsymbol{\varrho}$ , it follows that

$$-\partial^\nu \boldsymbol{\varrho}_{\mu\nu} + m_\varrho^2 \boldsymbol{\varrho}_\mu = \frac{1}{2} \sum_b g_{\varrho b} \bar{\psi}_b \gamma_\mu \boldsymbol{\tau} \psi_b, \quad (14)$$

where we have, again, a Proca equation, whose source is given by the baryon isospin four-current  $j_\mu = \bar{\psi}_b \gamma_\mu \boldsymbol{\tau} \psi_b$ . For the field  $\boldsymbol{\delta}$ , we obtain

$$(\partial_\mu \partial^\mu + m_\sigma^2) \boldsymbol{\delta} = \sum_b \bar{\psi}_b \left[ g_{\sigma b} (\Pi_{\zeta b}) - \frac{g_{\sigma b}}{m_b} (\Pi_{\zeta b})^{\frac{\zeta+1}{\zeta}} \times \right. \\ \left. \times \left( g_{\sigma b} + \frac{1}{2} g_{\delta b} \boldsymbol{\tau} \cdot \boldsymbol{\delta} + g_{\sigma^* b} \sigma^* \right) \right] \frac{\boldsymbol{\tau}}{2} \psi_b, \quad (15)$$

which is an equation analogous to that of the field  $\sigma$  and, therefore, it is again a Klein-Gordon equation with a scalar source related to the derivative coupling. For the field  $\sigma^*$ , it turns out that

$$(\partial_\mu \partial^\mu + m_{\sigma^*}^2) \sigma^* = \sum_b \bar{\psi}_b \left[ g_{\sigma^* b} (\Pi_{\zeta b}) - \frac{g_{\sigma^* b}}{m_b} (\Pi_{\zeta b})^{\frac{\zeta+1}{\zeta}} \times \right. \\ \left. \times \left( g_{\sigma b} + \frac{1}{2} g_{\delta b} \boldsymbol{\tau} \cdot \boldsymbol{\delta} + g_{\sigma^* b} \sigma^* \right) \right] \psi_b, \quad (16)$$

which is analogous to the equations for  $\sigma$  and  $\delta$ . For the field  $\phi$ , we obtain

$$-\partial^\nu \phi_{\mu\nu} + m_\omega^2 \phi_\mu = \sum_b g_{\phi b} \bar{\psi}_b \gamma_\mu \psi_b, \quad (17)$$

which is an equation analogous to that for  $\omega$ .

For the baryon fields  $\psi_b$ , it follows that

$$\sum_b \left[ \gamma_\mu \left( i \partial^\mu - g_{\omega b} \omega^\mu - \frac{1}{2} g_{\varrho b} \boldsymbol{\tau} \cdot \boldsymbol{\varrho}^\mu - g_{\phi b} \phi^\mu \right) \right. \\ \left. - \left( m_b - g_{\sigma b}^* \sigma - g_{\sigma^* b}^* \sigma^* - \frac{1}{2} g_{\delta b}^* \boldsymbol{\tau} \cdot \boldsymbol{\delta} \right) \right] \psi_b = 0, \quad (18)$$

which represents the Dirac equation modified by the meson fields. Here, once again, in the second term in parentheses, we notice the emergence of the effective baryon mass  $m_b^*$ , according to (7); furthermore, the kinetic term is displaced by the vector mesons. This feature introduces a modification in the chemical potential of the baryons, giving rise to the effective chemical potential

$$\mu_b^* = \mu_b - g_{\omega b} \gamma_\mu \omega^\mu - \frac{1}{2} g_{\varrho b} \gamma_\mu \boldsymbol{\tau} \cdot \boldsymbol{\varrho}^\mu - g_{\phi b} \gamma_\mu \phi^\mu, \quad (19)$$

where  $\mu_b$  is the chemical potential of each baryon, defined according to (3).

Finally, for the lepton fields, we obtain

$$\sum_l (i \gamma_\mu \partial^\mu - m_l) \psi_l = 0, \quad (20)$$

which represents the free Dirac equation, for leptons of mass  $m_l$ , since their contributions do not couple to the mesons. Therefore, the electron and muon appear in the form of a free gas, since they do not interact via the strong nuclear force. It is worth to note that, in this regime of energy, Coulomb interactions are not taken into account explicitly, in spite of the presence of charged species. This is called in literature a “Coulomb-less” model description [49]. In such a Coulomb-less approach, electromagnetic interactions are only accounted for through the imposition of charge neutrality, according to equation (2).

The equations of motion (12)-(17) obtained for the meson fields present nonlinear behavior due to the kinetic terms, making it difficult to obtain an exact solution. Therefore, it is convenient to use an approximate method to solve the problem. The mean-field approximation is a tool commonly used in many-body theory [50], since it maintains the original characteristics of the model, preserving the degrees of freedom and covariance. This approximation can be used because, in the high-density regime, the system is strongly coupled, making it reasonable to disregard the variations of the meson fields. This means that the variations of the meson fields will be small disturbances, negligible compared to the coupling amplitude at high densities and that, therefore, it is feasible to take into account only their average values.

Then, in the mean-field approximation, the meson fields are rewritten as:

$$\sigma \rightarrow \langle \sigma \rangle = \sigma_0, \\ \sigma^* \rightarrow \langle \sigma^* \rangle = \sigma_0^*, \\ \omega^\mu \rightarrow \langle \omega^\mu \rangle = \delta_0^\mu \omega_0, \\ \phi^\mu \rightarrow \langle \phi^\mu \rangle = \delta_0^\mu \phi_0, \\ \boldsymbol{\varrho}^\mu \rightarrow \langle \boldsymbol{\varrho}^\mu \rangle = \delta_0^\mu \varrho_{03}, \\ \boldsymbol{\delta} \rightarrow \langle \boldsymbol{\delta} \rangle = \delta_0^3, \quad (21)$$

where  $\delta_0^\mu$  is the Kroenecker delta function and  $\sigma_0$ ,  $\sigma_0^*$ ,  $\omega_0$ ,  $\phi_0$ ,  $\varrho_{03}$ , and  $\delta_0^3$  denote the classical expectation values of the meson fields. It is important to highlight that, in these equivalences, the  $z$  axis was chosen as the quantization axis in isospin space, so that:

$$\frac{1}{2} \boldsymbol{\tau} \cdot \boldsymbol{\varrho}^\mu \rightarrow \frac{1}{2} \langle \boldsymbol{\tau} \cdot \boldsymbol{\varrho}^\mu \rangle = \frac{1}{2} \tau^i \delta_i^\mu \varrho_{03} = I^3 \delta_0^\mu \varrho_{03} = I^3 \varrho_0^3, \\ \frac{1}{2} \boldsymbol{\tau} \cdot \boldsymbol{\delta} \rightarrow \frac{1}{2} \langle \boldsymbol{\tau} \cdot \boldsymbol{\delta} \rangle = \frac{1}{2} \tau^i \delta_{i3} \delta_0^3 = I^3 \delta_0^3, \quad (22)$$

where  $I^3$  corresponds to the isospin projection of each baryon in the  $z$  direction, whose values are found in Table I.

Applying the mean-field approximation to the meson equations of motion, (12), (13), (14), (15), (16) and (17),

we obtain:

$$\begin{aligned}
\sigma_0 &= \frac{1}{m_\sigma^2} \sum_b \left[ g_{\sigma b} (\Pi_{\zeta b}) \right. \\
&\quad \left. - \frac{g_{\sigma b}}{m_b} (\Pi_{\zeta b})^{\frac{\zeta+1}{\zeta}} (g_{\sigma b} \sigma_0 + g_{\delta b} \delta_0^3 I^{3b} + g_{\sigma^* b} \sigma_0^*) \right] n_{s_b}, \\
\omega_0 &= \frac{1}{m_\omega^2} \sum_b g_{\omega b} n_{B_b}, \\
\varrho_0^3 &= \frac{1}{m_\varrho^2} \sum_b g_{\varrho b} I^{3b} n_{B_b}, \\
\delta_0^3 &= \frac{1}{m_\delta^2} \sum_b \left[ g_{\delta b} (\Pi_{\zeta b}) \right. \\
&\quad \left. - \frac{g_{\delta b}}{m_b} (\Pi_{\zeta b})^{\frac{\zeta+1}{\zeta}} (g_{\sigma b} \sigma_0 + g_{\delta b} \delta_0^3 I^{3b} + g_{\sigma^* b} \sigma_0^*) \right] I^{3b} n_{s_b}, \\
\sigma_0^* &= \frac{1}{m_{\sigma^*}^2} \sum_b \left[ g_{\sigma^* b} (\Pi_{\zeta b}) \right. \\
&\quad \left. - \frac{g_{\sigma^* b}}{m_b} (\Pi_{\zeta b})^{\frac{\zeta+1}{\zeta}} (g_{\sigma b} \sigma_0 + g_{\delta b} \delta_0^3 I^{3b} + g_{\sigma^* b} \sigma_0^*) \right] n_{s_b}, \\
\phi_0 &= \frac{1}{m_\phi^2} \sum_b g_{\phi b} n_{B_b}. \tag{23}
\end{aligned}$$

In the above equations, the scalar density and baryon density are calculated, respectively, as  $n_{s_b} = \langle \bar{\psi}_b \psi_b \rangle$  and  $n_{B_b} = \langle \psi_b^\dagger \psi_b \rangle$  and, in accordance with (6),

$$\Pi_{\zeta b} = \left( 1 + \frac{g_{\sigma b} \sigma_0 + g_{\sigma^* b} \sigma_0^* + g_{\delta b} I^{3b} \delta_0^3}{\zeta m_b} \right)^{-\zeta}. \tag{24}$$

To calculate  $n_{s_b}$  and  $n_{B_b}$ , the equation of motion for the baryon fields  $\psi_b$  is also considered in the mean field approximation (for mesons only), from (18):

$$\begin{aligned}
\sum_b (i\gamma_\mu \partial^\mu - g_{\omega b} \gamma_0 \omega_0 - g_{\varrho b} \gamma_0 I^{3b} \varrho_0^3 \\
- g_{\phi b} \gamma_0 \phi_0 - m_b^*) \psi_b = 0. \tag{25}
\end{aligned}$$

In the mean-field approximation, according to (7) and (19), the effective mass and effective chemical potential of each baryon species can be rewritten respectively as:

$$m_b^* = m_b - \Pi_{\zeta b} (g_{\sigma b} \sigma_0 + g_{\sigma^* b} \sigma_0^* + g_{\delta b} I^{3b} \delta_0^3), \tag{26}$$

$$\mu_b^* = \mu_b - g_{\omega b} \omega_0 - g_{\varrho b} I^{3b} \varrho_0^3 - g_{\phi b} \phi_0. \tag{27}$$

Clearly, the lepton equation of motion, given by (20), does not undergo any modification due to the application of the mean field approximation, since it does not depend on the meson fields.

### C. EoS, densities and entropy at finite temperature

To determine the baryon density  $n_{B_b} = \langle \psi_b^\dagger \psi_b \rangle$  and the scalar density  $n_{s_b} = \langle \bar{\psi}_b \psi_b \rangle$ , it is necessary to consider the solutions to the modified Dirac equation (25) that describes the fields  $\psi_b$ . Since the mean-field approximation maintains the form of the equation and since, in this approximation, the scalar and vector mesons are represented by classical fields (i.e., constant functions in spacetime), the solutions will have the same form obtained for the free particle case. In short, they will be typical stationary plane wave solutions, with a displacement in the mass term, due to the scalar fields, according to (26), and also a displacement in the energy eigenvalues, due to the vector fields, according to (27). Then, from the expressions for  $\psi_b$  and  $\psi_b^\dagger$  and the anti-commutation relations between the creation and destruction operators of baryons and antibaryons,  $n_{B_b}$  and  $n_{s_b}$  can easily be obtained.

Regarding the calculations of energy density and pressure to construct the equation of state (EoS), both quantities can be obtained from the components of the energy-momentum tensor. In quantum field theory, the energy-momentum tensor is defined as

$$T_{\mu\nu} = -\mathcal{L}g_{\mu\nu} + \frac{\partial \mathcal{L}}{\partial(\partial^\mu \psi)} \partial_\nu \psi, \tag{28}$$

where  $g_{\mu\nu}$  is the Minkowsky metric tensor. If the field  $\psi$  satisfies a Dirac-like equation, such as equations (18) and (20), the first term in (28) vanishes, leaving:

$$T_{\mu\nu} = i\bar{\psi} \gamma^\mu \partial_\nu \psi. \tag{29}$$

Assuming an ideal fluid, one can identify

$$< T_{\mu\nu} > = (\varepsilon + p) u_\mu u_\nu - p g_{\mu\nu}, \tag{30}$$

as being the structure of the energy-momentum tensor and where the four-velocity, for a fluid at rest, is described by  $u^\mu = (1, \mathbf{0})$ , and satisfies  $u_\mu^2 = 1$ . The energy density  $\varepsilon$  and the pressure  $p$  of the system are thus determined by the expected value of the energy-momentum tensor.

$$\varepsilon = \langle T_{00} \rangle, \tag{31}$$

$$p = \frac{1}{3} (\langle T_{xx} \rangle + \langle T_{yy} \rangle + \langle T_{zz} \rangle), \tag{32}$$

where the energy-momentum tensor assumes the symmetric and isotropic form.

$$T_{\mu\nu} = \begin{pmatrix} \varepsilon & 0 & 0 & 0 \\ 0 & p & 0 & 0 \\ 0 & 0 & p & 0 \\ 0 & 0 & 0 & p \end{pmatrix}. \tag{33}$$

Using (29) and considering the standard form of Dirac matrices, equations (31) and (32) become

$$\varepsilon = i\bar{\psi} \gamma^0 \partial_0 \psi, \tag{34}$$

$$p = -\frac{i}{3}\bar{\psi}\vec{\gamma} \cdot \vec{\nabla}\psi. \quad (35)$$

In the finite temperature case ( $T \neq 0$ ), the integrals over the Fermi momenta (involved in the calculations of  $n_B$ ,  $n_s$ ,  $\varepsilon$  and  $p$ ) must extend to infinity, and both particles and antiparticles must be included in the statistical description. Therefore, the results for all these physical quantities can be summarized as follows:

$$n_B = \sum_{j=b} n_{B_j} = \frac{1}{\pi^2} \sum_{j=b} \int_0^\infty dk_j k_j^2 (f_{j+} + f_{j-}), \quad (36)$$

$$n_s = \sum_{j=b} n_{s_j} = \sum_{j=b} \frac{m_j^*}{\pi^2} \int_0^\infty dk_j \frac{k_j^2}{E_j} (f_{j+} + f_{j-}), \quad (37)$$

$$\begin{aligned} \varepsilon = & \frac{m_\sigma^2 \sigma_0^2}{2} + \frac{m_\delta^2 \delta_0^3}{2} + \frac{m_{\sigma^*}^2 \sigma_0^{*2}}{2} + \frac{m_\omega^2 \omega_0^2}{2} \\ & + \frac{m_\varrho^2 \varrho_0^3}{2} + \frac{m_\phi^2 \phi_0^2}{2} + \sum_{j=b} \varepsilon_j + \sum_{j=l} \varepsilon_j, \end{aligned} \quad (38)$$

$$\begin{aligned} p = & -\frac{m_\sigma^2 \sigma_0^2}{2} - \frac{m_\delta^2 \delta_0^3}{2} - \frac{m_{\sigma^*}^2 \sigma_0^{*2}}{2} + \frac{m_\omega^2 \omega_0^2}{2} \\ & + \frac{m_\varrho^2 \varrho_0^3}{2} + \frac{m_\phi^2 \phi_0^2}{2} + \sum_{j=b} p_j + \sum_{j=l} p_j, \end{aligned} \quad (39)$$

where

$$\varepsilon_j = \frac{1}{\pi^2} \int_0^\infty dk_j k_j^2 E_j (f_{j+} + f_{j-}), \quad (40)$$

$$p_j = \frac{1}{\pi^2} \int_0^\infty dk_j \frac{k_j^4}{E_j} (f_{j+} + f_{j-}), \quad (41)$$

being  $k_j$  the momentum for each species  $j$  of fermion (baryon  $b$  or lepton  $l$ ),  $E_b = \sqrt{k_b^2 + (m_b^*)^2}$  the energy for each species of baryon  $b$ ;  $E_l = \sqrt{k_l^2 + m_l^2}$  the energy for each species of lepton  $l$ ; additionally,  $f_{b+}$  e  $f_{b-}$  are the Fermi-Dirac distributions for baryons and antibaryons, respectively, and  $f_{l+}$  e  $f_{l-}$  are the Fermi-Dirac distributions for leptons and antileptons, respectively:

$$f_{b\pm} = \left[ \frac{1}{e^{(E_b \mp \mu_b^*)/T} + 1} \right], \quad f_{l\pm} = \left[ \frac{1}{e^{(E_l \mp \mu_l)/T} + 1} \right]. \quad (42)$$

In the above expressions,  $m_b^*$  and  $\mu_b^*$  are given by equations (26) and (27), respectively.

It is important to highlight that, technically, equation (36) gives the *net baryon density*, i.e., the number of particles minus the number of antiparticles, although the word “net” is often omitted. Using the net baryon

density allows the value to be conserved by particle-antiparticle creation and annihilation events.

The total entropy density reads:

$$s = \sum_{j=b} s_j + \sum_{j=l} s_j, \quad (43)$$

being

$$\begin{aligned} s_j = & \frac{1}{\pi^2} \int_0^\infty dk_j k_j^2 \left[ f_{j+} \ln \left( \frac{1}{f_{j+}} \right) + f_{j-} \ln \left( \frac{1}{f_{j-}} \right) \right. \\ & \left. + (1 - f_{j+}) \ln \left( \frac{1}{1 - f_{j+}} \right) + (1 - f_{j-}) \ln \left( \frac{1}{1 - f_{j-}} \right) \right], \end{aligned} \quad (44)$$

where the Fermi-Dirac distributions  $f_{j+}$  and  $f_{j-}$  follow the prescription of (42). The above expression for  $s_j$  is basically the formula for the entropy density of a free Fermi gas; however, it is important to emphasize that the interactions are implicit in the Fermi-Dirac distributions for baryons, as long as they contain both the effective chemical potential  $\mu_b^*$  (which depends on the scalar meson fields) and the effective mass  $m_b^*$  (which is present in the definition of the energy for baryons  $E_b$  and depends on the vector meson fields). In this context, the entropy per baryon  $S/A$  can be defined as:

$$S/A = s/n_B, \quad (45)$$

where  $s$  and  $n_B$  are defined by expressions (43) and (36), respectively.

Here, in expressions (36), (37), (38), (39) and (43), the summations correspond to the kinetic contributions (matter contributions) to baryons (summation in  $b$ ) and leptons (summation in  $l$ ); moreover, in expressions (38) and (39), the first six terms represent the contributions of the meson fields to the EoS.

## D. Meson-nucleon couplings

In the scalar (S) version of the MBF Model, each choice of  $\zeta$  corresponds to a different parameterization of the model. Then, given a specific value for  $\zeta$ , the meson-nucleon coupling constants can be determined in two steps, for isospin symmetric and asymmetric matter, following the procedure described in detail in the Appendix.

Observing the data in Table IV, it is evident that the adjustable parameter  $\zeta$  functions as a control that allows fine-tuning the intensity of the many-body contributions in the MBF Model, establishing a middle ground between the predictions of Walecka and Zimanyi–Moszkowski models. Note that, as the parameter  $\zeta$  increases, the effective mass of the nucleon at saturation  $(m_N^*)_0$  also increases and the compressibility at saturation  $K_0$  decreases, disclosing a spectrum between the limiting values of Walecka [13] and Zimanyi–Moszkowski [15] models, which are, respectively, in their original configurations,  $(m_N^*)_0 = 0.54 m_N$  with  $K_0 = 560$  MeV and

TABLE IV. Effective mass of the nucleon, compressibility, and symmetry energy, symmetry energy slope (all at saturation), and meson-nucleon coupling constants for different parameterizations of the scalar (S) version of the MBF Model. These results consider a saturation density  $n_0 = 0.15 \text{ fm}^{-3}$  and a binding energy per baryon  $B/A = -15.75 \text{ MeV}$ . The lines in bold describe the two parameterizations that will be focused on in the present work.

$\zeta$	$\frac{(m_N^*)_0}{m_N}$	$K_0$	$a_{sym}^0$	$L_0$	$(\frac{g_\sigma}{m_\sigma})^2$	$(\frac{g_\omega}{m_\omega})^2$	$(\frac{g_\varrho}{m_\varrho})^2$	$(\frac{g_\delta}{m_\delta})^2$
		(MeV)	(MeV)	(MeV)	(fm $^2$ )	(fm $^2$ )	(fm $^2$ )	(fm $^2$ )
0.040	0.66	297	25	76	14.51	8.74	2.56	0.38
0.040	0.66	297	25	90	14.51	8.74	6.53	6.50
<b>0.040</b>	<b>0.66</b>	<b>297</b>	<b>33</b>	<b>100</b>	<b>14.51</b>	<b>8.74</b>	<b>4.74</b>	<b>0.38</b>
0.040	0.66	297	33	115	14.51	8.74	6.93	0.66
0.049	0.68	272	25	74	13.99	8.14	2.53	0.16
0.049	0.68	272	25	90	13.99	8.14	7.20	7.56
0.049	0.68	272	33	100	13.99	8.14	5.31	1, 11
0.049	0.68	272	33	115	13.99	8.14	9.65	8.02
0.059	0.70	253	25	73	13.44	7.55	2.75	0.34
0.059	0.70	253	25	90	13.44	7.55	7.78	8.54
0.059	0.70	253	33	100	13.44	7.55	5.84	1.82
0.059	0.70	253	33	115	13.44	7.55	10.24	9.00
0.071	0.72	237	25	72	12.74	6.90	2.97	0.61
0.071	0.72	237	25	90	12.74	6.90	8.12	9.25
0.071	0.72	237	33	100	12.74	6.90	7.00	3.70
0.071	0.72	237	33	115	12.74	6.90	10.50	9.62
0.085	0.74	225	25	72	12.13	6.32	2.88	0.21
0.085	0.74	225	25	90	12.13	6.32	8.60	9.84
0.085	0.74	225	33	100	12.13	6.32	7.34	4.00
0.085	0.74	225	33	115	12.13	6.32	10.70	10.10
0.104	0.76	216	25	73	11.46	5.71	3.30	1.21
0.104	0.76	216	25	90	11.46	5.71	8.80	10.31
0.104	0.76	216	33	100	11.46	5.71	7.50	4.28
0.104	0.76	216	33	115	11.46	5.71	10.93	10.30
0.129	0.78	211	25	73	10.78	5.13	4.10	3.00
0.129	0.78	211	25	90	10.78	5.13	9.10	10.60
<b>0.129</b>	<b>0.78</b>	<b>211</b>	<b>33</b>	<b>100</b>	<b>10.78</b>	<b>5.13</b>	<b>7.60</b>	<b>4.60</b>
0.129	0.78	211	33	115	10.78	5.13	11.10	10.50

$(m_N^*)_0 = 0.85 m_N$  with  $K_0 = 225 \text{ MeV}$ . Furthermore, it should be highlighted that, due to the specific form of the parametric term  $\Pi_{\zeta b}$  that characterizes the MBF Model, which is explicitly dependent on the scalar meson fields (see equation (24)), an increase in the parameter  $\zeta$  implies a reinforcement of the attractive components of the nuclear interaction, which is the reason for the decrease in the compressibility when  $\zeta$  is increased. Without the intention to be exhaustive, Table IV presents seven possible values for the pair  $(m_N^*)_0/K_0$ , and, for each one of those, two values for  $a_{sym}^0$  and four values for  $L_0$ . Hence, the values presented in Table IV serve as benchmarks in the continuous parameter map that can be constructed for the MBF Model.

From these considerations, it becomes clear that the general form of the parametric term  $\Pi_{\zeta b}$  (24) can be regarded as a generalized *ansatz*, based on reproducing other RMF results.

## E. Meson-hyperon couplings

Hyperons are heavy baryons that have at least one strange quark in their composition (see Table I). Because of their high mass, they are not energetically favored in nuclear matter close to the saturation density; therefore, it is not possible to fit the coupling constants between mesons and hyperons based on some property of nuclear matter as was done previously with  $g_\sigma$ ,  $g_\omega$ ,  $g_\varrho$  and  $g_\delta$ , when only nucleons were present.

Different proposals for the meson-hyperon coupling constants have been considered in literature, and three of them will be adopted in the present work:

**U - Universal Coupling:** In this very simple proposal, the coupling constants for hyperons ( $Y = \Lambda, \Sigma, \Xi$ ) and nucleons are considered to be identical:

$$g_{\sigma Y} = g_\sigma, \quad g_{\omega Y} = g_\omega, \quad g_{\varrho Y} = g_\varrho, \quad (46)$$

$$g_{\delta Y} = g_\delta, \quad g_{\phi Y} = g_\phi.$$

Moreover, considering that the strange mesons do not couple to the nucleons,  $g_{\sigma^*} = 0$  and  $g_\phi = 0$ .

**M - Moszkowski Coupling:** Based on the quark content of nucleons and hyperons, Moszkowski proposed [51] that meson-hyperon coupling constants should be corrected according to:

$$g_{\sigma Y} = \sqrt{\frac{2}{3}} g_\sigma, \quad g_{\omega Y} = \sqrt{\frac{2}{3}} g_\omega, \quad g_{\varrho Y} = \sqrt{\frac{2}{3}} g_\varrho, \quad (47)$$

$$g_{\delta Y} = \sqrt{\frac{2}{3}} g_\delta, \quad g_{\phi Y} = \sqrt{\frac{2}{3}} g_\phi.$$

In this scheme, for the reasons previously stated, we also consider  $g_{\sigma^*} = 0$  and  $g_\phi = 0$ .

**SU(6) - Spin-Flavor Symmetry Coupling:** This coupling scheme takes into account the strangeness of the particles and the isospin proportion between nucleons and hyperons [52, 53]:

$$\frac{1}{3} g_\omega = \frac{1}{2} g_{\omega \Lambda} = \frac{1}{2} g_{\omega \Sigma} = g_{\omega \Xi}, \quad (48)$$

$$g_\varrho = \frac{1}{2} g_{\varrho \Sigma} = g_{\varrho \Xi}, \quad g_{\varrho \Lambda} = 0,$$

$$-\frac{2\sqrt{2}}{3} g_\omega = 2g_{\phi \Lambda} = 2g_{\phi \Sigma} = g_{\phi \Xi}, \quad g_\phi = 0,$$

$$g_\delta = \frac{1}{2} g_{\delta \Sigma} = g_{\delta \Xi}, \quad g_{\delta \Lambda} = 0.$$

Furthermore, we obtain the hyperon-sigma coupling associated to the attractive interaction between hyperons and nucleons by fitting the potential depths of the hyperons in nuclear matter  $U_Y$ , according to the prescription [54, 55]:

$$g_{\sigma Y} = \frac{g_{\omega Y} \omega_0(n_0) - U_Y}{\sigma_0(n_0)}. \quad (49)$$

Using the values presented in reference [56], we consider  $U_\Lambda = -28 \text{ MeV}$ ,  $U_\Sigma = +30 \text{ MeV}$  and  $U_\Xi = -18 \text{ MeV}$ .

Finally, we still need to define the coupling of hyperons with the meson  $\sigma^*$  for all coupling schemes. Considering the lack of experimental information on hyperon-hyperon interaction and, therefore, on  $U_{YY}$  potentials, we choose to follow the approach already established in the literature for the MBF Model and define that the couplings of hyperons with this meson are all identical ( $g_{\sigma^*\Lambda} = g_{\sigma^*\Sigma} = g_{\sigma^*\Xi}$ ) and we varied their values freely. Adopting the range of values from [39], we have  $g_{\sigma^*Y} = 0 - 5$ . Two remarks should be made regarding these limiting values. The first is that, since  $\sigma^*$  is a scalar meson, it introduces a new attractive contribution to the EoS, resulting in a decrease in the maximum mass of the stars; indeed, it has already been shown that, for the most rigid parameterization of the model ( $\zeta = 0.040$ ), the range of values  $g_{\sigma^*Y} = 0 - 5$  produces a decrease in the value of the maximum mass from  $2.15 M_{\text{Sun}}$  to  $2.12 M_{\text{Sun}}$  [39], and this effect is even more pronounced for parameterizations that produce softer EoSs and which, consequently, provide stars with even lower maximum mass. The second remark is that the value of the  $g_{\sigma^*Y}$  couplings cannot be increased indiscriminately because, in addition to its value being limited by observational predictions, it also has an impact on the effective mass of the hyperons, decreasing it; therefore, the limit of validity of the MBF formalism corresponds to the density for which the effective masses of the hyperons become zero, and, from that point, a formalism that goes beyond the mean-field approximation is necessary [18, 57, 58].

### III. RESULTS FOR NUCLEAR MATTER PROPERTIES AT FINITE TEMPERATURE

From the discussion presented in Section IID, it is evident that the MBF Model exhibits enough flexibility to fit experimental constraints, which translates into a variety of possibilities for the coupling constants, some of which are shown in Table IV. In other words, our formalism provides numerous distinct EoSs. Therefore, in order to obtain and discuss numerical results, we consider only two extreme values of the adjustable parameter  $\zeta$  which give the same results for  $a_{\text{sym}}^0$  (symmetry energy at saturation) and  $L_0$  (slope of the symmetry energy at saturation), which allows us to focus on many-bodies effects. These two parameterizations are shown in bold letters in Table IV. For this reason, throughout Sections III, and IV, the reader should bear in mind that, as a matter of fact, the MBF Model is capable of reproducing any intermediate result between those presented in the plots for  $\zeta = 0.040$  and  $\zeta = 0.129$ .

Regarding the values for  $g_{\sigma^*Y}$ , the procedure is analogous: in the following sections, numerical results will be presented for two antipode values,  $g_{\sigma^*Y} = 0$  and  $g_{\sigma^*Y} = 5$ , corresponding, respectively, to no additional attraction between hyperons (in comparison to nucleons) and to an enhanced attraction between hyperons.

Furthermore, it would be possible to adopt many dif-

ferent configurations to study the case of finite temperature. Hence, without the intention of being exhaustive, we will present results for three paradigmatic scenarios, where entropy per baryon is fixed, following pioneering studies [59–63] and also more recent works (see, e.g., [64], [65] and [66]):

- $S/A = s/n_B = 1, Y_l = 0.4$
- $S/A = s/n_B = 2, \mu_\nu = 0$
- $S/A = s/n_B = 0, \mu_\nu = 0$

These correspond to three snapshots of the time evolution of a compact star in its first minutes of life. Initially, the star is relatively warm (represented by fixed entropy per particle  $S/A = 1$ ) and has a large number of trapped neutrinos, since their mean free path is much shorter than the star's radius, which can be represented by a fixed lepton fraction  $Y_l$ , defined as

$$Y_l = \sum_{j=l} Y_{lj} = \sum_{j=l} \frac{n_{lj}}{n_B} = \sum_{j=l} \frac{\mathfrak{L}_j n_j}{n_B}. \quad (50)$$

Next, in the deleptonization stage of the PNS evolution, neutrinos gradually diffuse outward and escape; as they diffuse, they deposit energy via scattering and absorption in certain layers of the star, in a process that can locally increase the temperature (the so-called “Joule heating”), here represented by the fixed entropy per particle  $S/A = 2$  [59, 67]. Finally, the star becomes transparent to neutrinos, cools down gradually by neutrino emission and settles into a cold NS ( $\sim S/A = 0$  or  $T = 0$ ). The value  $Y_l \simeq 0.4$  is taken from numerical simulations of proto-neutron-star evolution [60, 67–70].

The choice to study the properties of nuclear matter for a fixed entropy per baryon  $S/A$  also has a compelling physical meaning, because: (i) when the iron core of a massive star collapses and rebounds to form a PNS, the collapse is nearly adiabatic, meaning that each fluid element conserves its entropy per baryon (as long as heat cannot flow fast enough to homogenize temperature); (ii) if entropy per baryon is fixed instead of temperature, the temperature will automatically adjust with density (because compressing matter adiabatically increases  $T$ ), and that provides a self-consistent temperature profile, which is what actually happens in a star that evolves quasi-adiabatically.

It is important to emphasize that, during the initial stages of evolution of a PNS, which here correspond to the cases of finite temperature, the system is potentially out of equilibrium; however, even in these cases, we apply the beta-equilibrium condition as a first approach, following other studies established in the literature [65, 71, 72].

In the following subsections, our results are consistently presented in two sets of plots:

- **SET 1:** Each panel shows the numerical results for fixed values of  $\zeta$  ( $\zeta = 0.040$  or  $\zeta = 0.129$ ) and  $g_{\sigma^*}$  ( $g_{\sigma^*} = 0$  or  $g_{\sigma^*} = 5$ ), displaying all three scenarios

of entropy per baryon –  $S/A = 1$  (dotted lines),  $S/A = 2$  (dashed lines) and  $S/A = 0$  (solid lines) – and covering four different possibilities for the inclusion of hyperons:  $N$  - pure nucleonic matter, containing only neutrons, protons, electrons and muons (black lines);  $U$  - universal coupling (green lines);  $M$  - Moszkowski coupling (red lines);  $SU(6)$  - spin-flavor symmetry coupling (blue lines). Each row (line) of plots in this set aims to enable a direct, side-by-side comparison of the changes caused in the physical quantity as a result of the change in the value of the adjustable parameter  $\zeta$  characteristic of the MBF Model.

- **SET 2:** Each panel shows the numerical results for fixed values of entropy per baryon ( $S/A = 1$ ,  $S/A = 2$  or  $S/A = 0$ ) and  $g_{\sigma^*}$  ( $g_{\sigma^*} = 0$  or  $g_{\sigma^*} = 5$ ), displaying together two options for  $\zeta - \zeta = 0.040$  (solid lines) and  $\zeta = 0.129$  (dashed lines) – and covering four different possibilities for the inclusion of hyperons:  $N$  - pure nucleonic matter, containing only neutrons, protons, electrons and muons (black lines);  $U$  - universal coupling (green lines);  $M$  - Moszkowski coupling (red lines);  $SU(6)$  - spin-flavor symmetry coupling (blue lines). Each row (line) of plots in this set aims to provide a glimpse of the time evolution of the star, from a hot PNS into a cold NS.

### A. Equations of state

As already discussed in Section IA, the EoS is the key quantity to describe how nuclear matter behaves. The EoS of nuclear matter is the fundamental relation that connects pressure and energy density within strongly interacting systems. It encapsulates the collective behavior that emerges from the complex interplay of nuclear forces at both microscopic and macroscopic scales. In essence, the EoS dictates how compressible or stiff nuclear matter is, governing the internal structure, stability, and observable properties of NSs.

In the framework of the MBF Model, each choice of the adjustable parameter  $\zeta$  provides a different EoS. Fig. 2 shows, side by side, the EoSs for  $\zeta = 0.040$  and  $\zeta = 0.129$  at different temperatures, considering  $g_{\sigma^*}^* = 0$  in the upper panels and  $g_{\sigma^*}^* = 5$  in the lower ones. Comparing these two extreme values for  $\zeta$ , it is clear that pressure increases more rapidly with  $\varepsilon$  for  $\zeta = 0.040$ , meaning that this parameterization predicts a stiffer behavior for nuclear matter. Additionally, it is also evident that the inclusion of the scalar strange meson does not have a significant impact on the overall appearance of the EoS (compare the upper and lower panels of both Figs. 2 and 3).

In Fig. 3, the sequence of the three upper panels ( $g_{\sigma^*}^* = 0$ ) and, in parallel, the sequence of the three lower panels ( $g_{\sigma^*}^* = 5$ ) allow us to glimpse the temporal evo-

lution of the EoS as the system evolves from the early stages of a PNS (left panels) to a cold NS (right panels). When analyzing these graphs, the reader should keep in mind that, by varying the adjustable parameter  $\zeta$  or the coupling scheme of the hyperons, the MBF Model is capable of reproducing virtually any EoS between the softest EoS (the blue dashed line, for  $\zeta = 0.129$  and  $SU(6)$ ) and the stiffest EoS (the black solid line, for pure nucleonic matter with  $\zeta = 0.040$ ) shown there. Focusing on the black lines (nucleonic matter) no difference can be spotted between panels, except for a slightly higher pressure in the high density regime for  $T = 0$ .

Regarding hyperonic matter, there is a patent ranking in the stiffness of the EoS, according to the different coupling schemes, all below the black curves for nucleonic matter:  $U$ ,  $M$  and  $SU(6)$  (from the stiffest to the softest). A deeper inspection into this feature reveals that, since the  $SU(6)$  coupling scheme results in a much softer behavior than the other cases, the corresponding EoS is much more sensible to the appearance of hyperons. The onset of these strange baryons opens new degrees of freedom; therefore, instead of all the pressure being supported by nucleons, some of the baryon number is carried by hyperons, which reduces the Fermi pressure of nucleons. This “softens” the EoS, meaning that pressure rises more slowly with increasing density. That is the explanation for the pronounced inflection around  $\varepsilon \simeq 350$  MeV (for  $\zeta = 0.040$ ) or  $\varepsilon \simeq 400$  MeV (for  $\zeta = 0.129$ ) in the blue curves, mostly for  $T = 0$  (see the solid blue curves in Fig. 2). Our results are in good agreement with those obtained for other density dependent RMF models at  $T = 0$  (compare, for example, the upper-right and lower-right panels of Fig. 3 with Fig. 1 in reference [73]).

When hyperons are included, the different evolution snapshots (columns in Fig. 3) show a more diverse behavior, with curves crossing differently at different energy densities. Moreover, the universal coupling ( $U$ ) for hyperons provides an EoS which is close to the EoS for pure nucleonic matter: indeed, comparing the black lines and the corresponding green lines in Figs. 2 and 3, it can be seen that they almost overlap. This result points out that one can obtain stiff EoSs even if hyperons are included in the formalism, simply by choosing the suitable coupling scheme.

Here, all sets of EoSs are numerically checked for thermodynamic consistency using Gibbs-Duhem relation:

$$\varepsilon + p = T \left( \sum_{j=b} s_j + \sum_{j=l} s_j \right) + \sum_{j=b} n_{B_j} \mu_j + \sum_{j=l} n_{l_j} \mu_j, \quad (51)$$

where  $\mu_j$  is given by equation (3) and  $n_{l_j}$  is the number density of each lepton species  $j = l$ , calculated through the usual integration over momentum space:

$$n_{l_j} = \frac{1}{\pi^2} \int_0^\infty dk_j k_j^2 (f_{j+} + f_{j-}). \quad (52)$$

However, it is clear that the mere inspection of the EoSs is not sufficient to reveal the behavior of nuclear

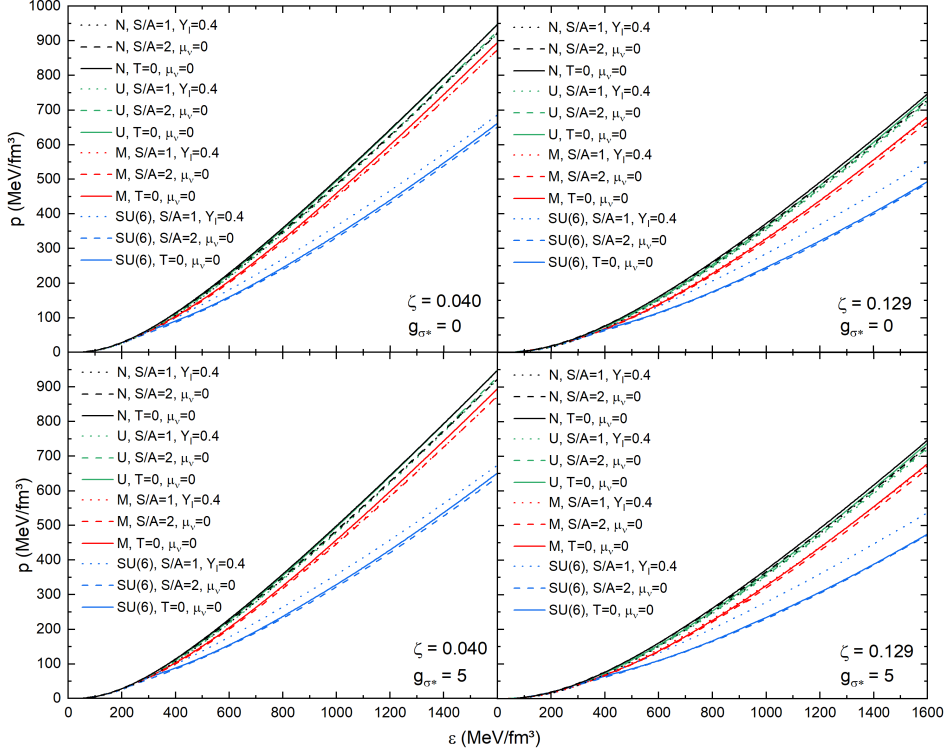


FIG. 2. **SET 1 (Equations of state):** Pressure ( $p$ ) as a function of energy density ( $\varepsilon$ ) for different proto-neutron star evolution snapshots, particle composition, and hyperon couplings. The different panels show different MBF (left vs. right) and strange scalar meson parameterizations (top vs. bottom).

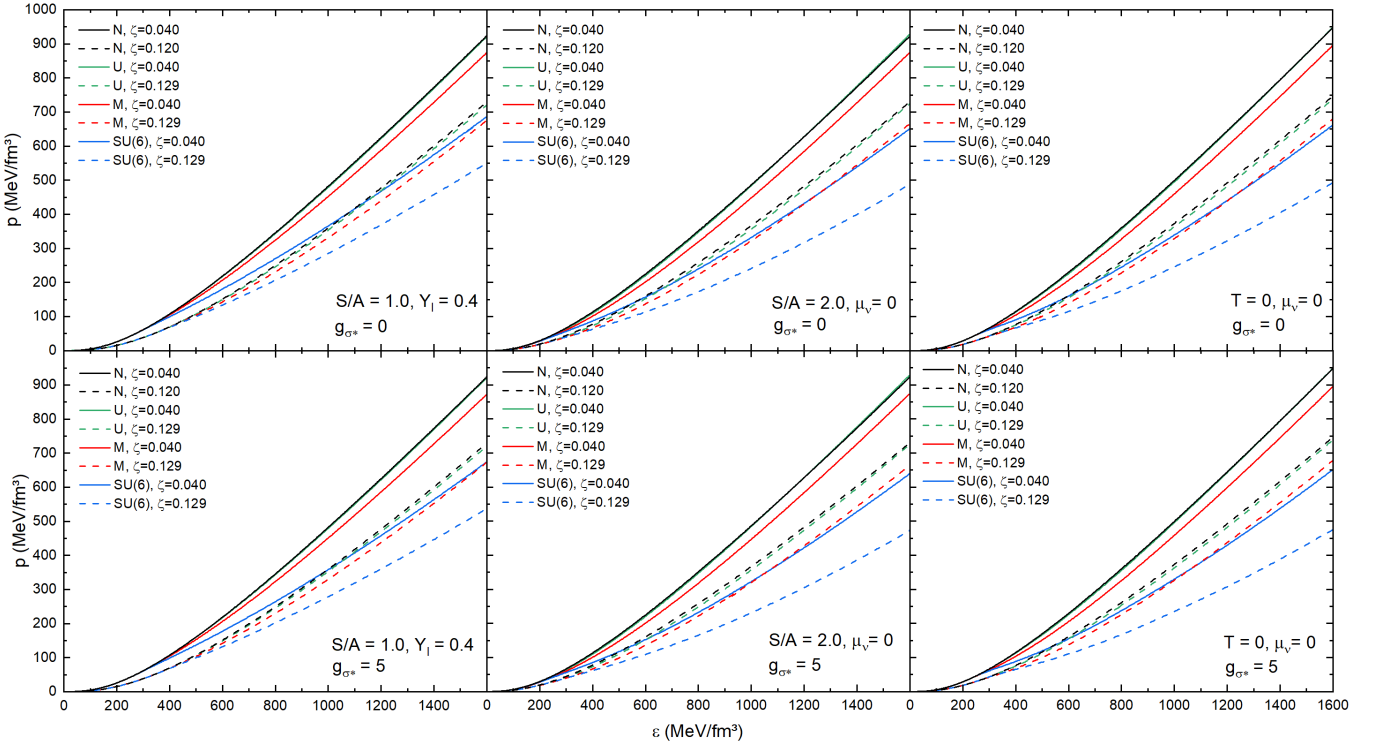


FIG. 3. **SET 2 (Equations of state):** Same as Fig. 2 but now the different panels show different evolution snapshots (left/center/right) and strange scalar meson parameterizations (top vs. bottom).

matter in all its details. For this reason, in the following sections, we discuss the most relevant properties of dense matter, seeking to reveal further differences between the various configurations of the MBF Model here examined.

### B. Populations of particles and antiparticles

As we consider increasingly higher densities, according to QCD predictions, the baryon effective mass decreases and new baryon degrees of freedom should be included in the description of the system. This is because, as the energy density of the system increases, chemical processes allow the generation of stable heavier particles. Since the timescale of the weak interaction is small even when compared to the timescale for the collapse of a supernova [32], it is possible that the net strangeness resulting from the neutron star matter is non-zero.

Therefore, from a theoretical point of view, hyperons should be expected to be present in hadronic matter at high densities [74]. Thus, when the Fermi energy of the nucleons exceeds the mass of these heavier baryons, the existence of these particles is favored in order to minimize the energy of the system. The formation of hyperons is associated with the chemical potentials of these particles, given by equation (3), which determine the model's particle creation threshold. By knowing the threshold condition, we can analyze how particle properties influence their emergence and also determine their relative population for different baryon densities.

A concise and comprehensive way to assess the proportions of particles present in the system is to analyze the fraction of strangeness, which represents the number of hyperons relative to the total number of baryons. The fraction of strangeness  $Y_S$  can be defined as

$$Y_S = \sum_j \frac{n_{B_j} |\mathcal{S}_j|}{n_B} = \frac{n_{B_\Lambda} + n_{B_\Sigma} + 2n_{B_\Xi}}{n_B}, \quad (53)$$

where  $\mathcal{S}_j$  is the strangeness of these particles, according to the values given in Table I.

Nonetheless, a more detailed analysis can be carried out by calculating the populations of particles (or antiparticles), i.e., the ratio  $Y_j$  between the number density of a given species  $j$  present in the system ( $n_j$ ) and the total baryon density  $n_B$ :

$$Y_j = \frac{n_j}{n_B}. \quad (54)$$

For baryons,  $n_j \equiv n_{Bj}$ , which can be determined from equation (36); for leptons,  $n_j \equiv n_{lj}$ , which can be determined from equation (52). These two equations remind us that these densities are *net densities*, i.e., the result that emerges from subtracting the number of particles and the number of antiparticles of a given species  $j$ . In order to calculate the number density of a certain antiparticle separately, one must consider

$$n_j = \frac{1}{\pi^2} \int_0^\infty dk_j k_j^2 f_{j-}, \quad (55)$$

where the Fermi-distribution function for antiparticles  $f_{j-}$  is defined in (42).

Figs. 4 and 5 display the strangeness fraction  $Y_S$  as a function of the baryon density  $n_B$  for several thermodynamic conditions and hyperon-meson coupling schemes. Additionally, the panels shown in Figs. 6, 7, 8 and 9 represent the populations of particles defined by the fractions  $Y_j$ , according to equation (54). Broadly speaking, all panels in Figs. 4 and 5 show the same qualitative trend:  $Y_S$  remains vanishingly small at low densities, rises sharply once the first hyperons become energetically favored (especially for  $T = 0$ ), and then increases monotonically as additional strange baryons populate the system. The precise onset density and growth rate, however, depend sensitively on (i) the thermodynamic state of matter (characterized by the values of  $S/A$  in the different snapshots of evolution), (ii) the stiffness of the equation of state (encoded in the parameter  $\zeta$ ), and (iii) the adopted hyperonic couplings.

The four panels in Fig. 4 allow us to isolate the effects of both the parameter  $\zeta$  and the inclusion of the strange scalar meson  $\sigma^*$ . For each panel, the three thermal scenarios (dashed for  $S/A = 1$  with trapped neutrinos, and dotted for  $S/A = 2$  without neutrinos and solid curves for  $T = 0$ ) clearly separate. At finite temperature and/or fixed entropy, the thermal population of the Fermi sea lowers the threshold for hyperon formation. As a result, hyperons appear earlier, and  $Y_S$  rises more gradually than in the cold, neutrino-free case.

Comparing the left and right panels of each row of Fig. 4 highlights the role of the adjustable parameter  $\zeta$ . A closer inspection of the panels reveals that the sensitivity of the strangeness fraction to the parameter  $\zeta$  is more nuanced than a simple “stiffer vs. softer” dichotomy. In fact, the effect of  $\zeta$  strongly depends on the chosen hyperon-meson coupling scheme. For  $SU(6)$ -type couplings, the stiffer model ( $\zeta = 0.040$ ) consistently leads to larger strangeness fractions at a given density, indicating that the additional stiffness actually facilitates hyperon formation once the threshold is crossed. For the universal coupling prescription ( $U$ ), however, the opposite trend emerges: the softer model ( $\zeta = 0.129$ ) generally produces higher values of  $Y_S$  at fixed density. In turn, the Moszkowski prescription ( $M$ ) shows only tiny sensitivity to  $\zeta$ , with both parameterizations yielding nearly identical  $Y_S$  curves across the entire density range.

This mixed pattern is present not only in the cold-matter limit but remains visible in the finite-temperature and finite-entropy scenarios as well. In other words, thermal effects do not obscure the influence of  $\zeta$ , and the model exhibits a coupling-dependent interplay between stiffness and strangeness production rather than a universal behavior across all prescriptions.

The influence of the hyperonic couplings is encoded in the color scheme. At finite temperature (or fixed entropy), the onset density for hyperons is essentially the same for all coupling schemes, since thermal smearing washes out the details of the threshold condition. In

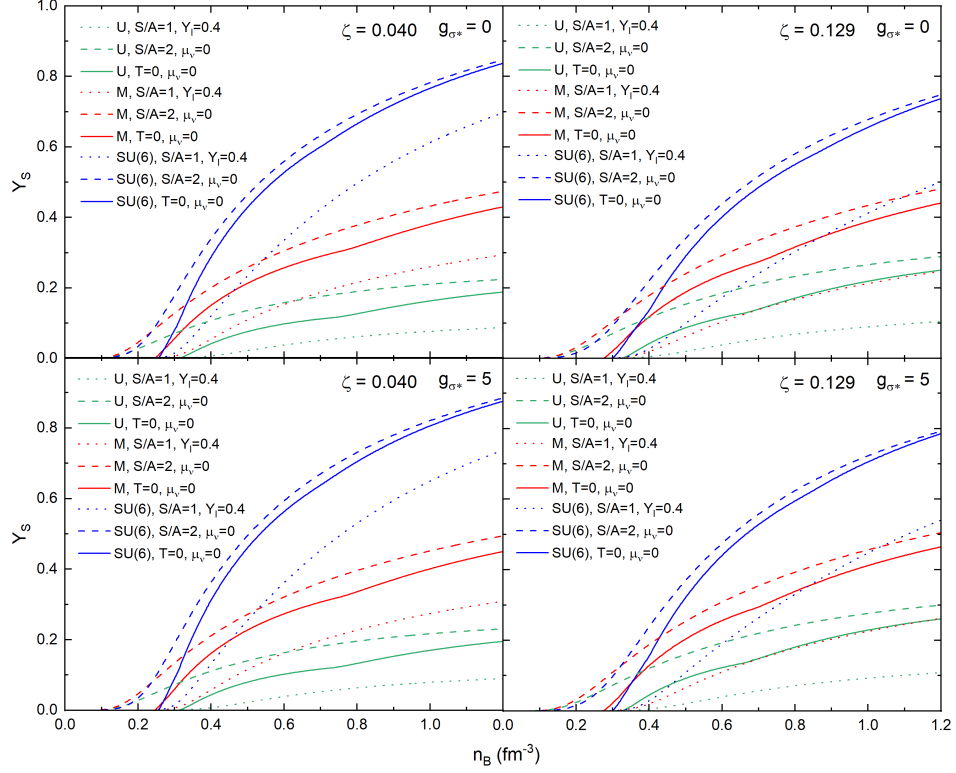


FIG. 4. **SET 1 (Fraction of strangeness):** Fraction of strangeness ( $Y_S$ ) as a function of baryon density ( $n_B$ ) for different proto-neutron star evolution snapshots, particle composition, and hyperon couplings. The different panels show different MBF (left vs. right) and strange scalar meson parameterizations (top vs. bottom).

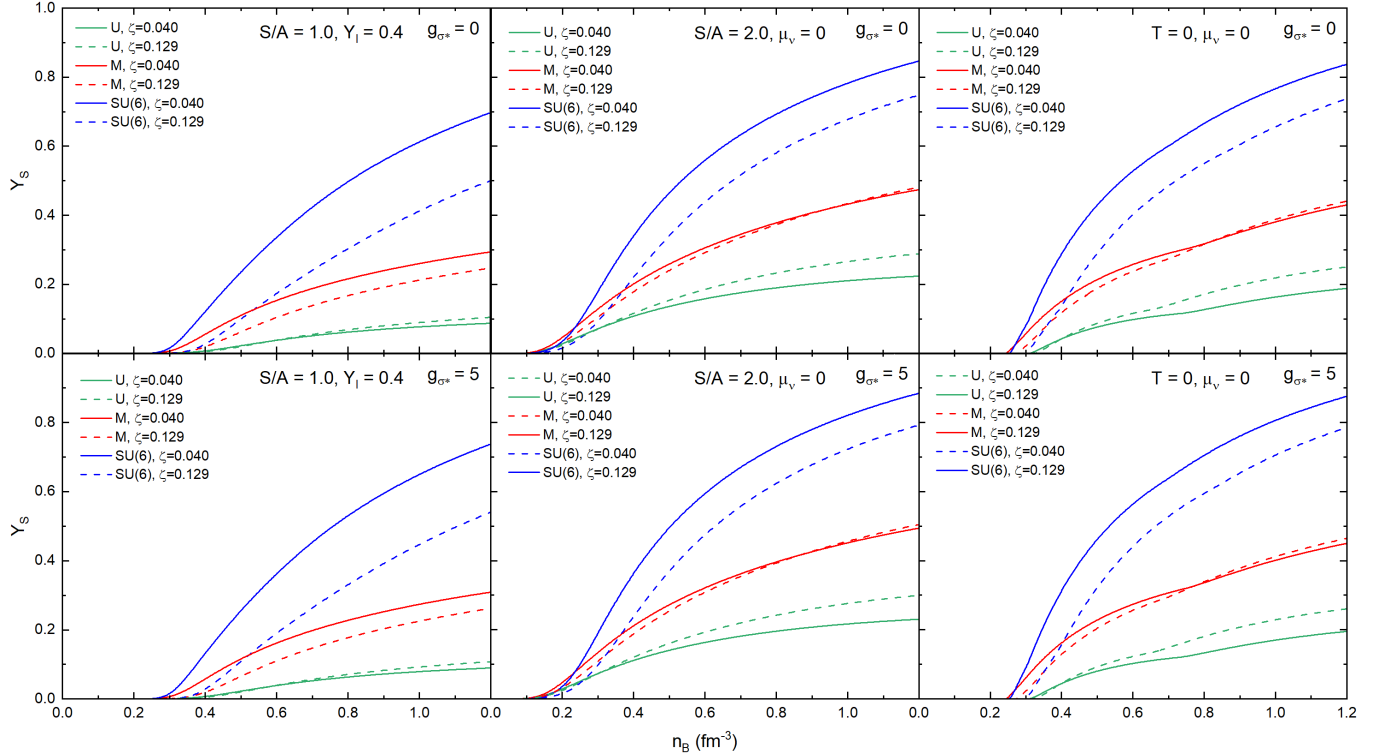


FIG. 5. **SET 2 (Fraction of strangeness):** Same as Fig. 4 but now the different panels show different evolution snapshots (left/center/right) and strange scalar meson parameterizations (top vs. bottom).

the cold-matter case, however, clear differences arise: both the  $SU(6)$  and Moszkowski ( $M$ ) prescriptions allow hyperons to appear at slightly lower densities (around  $n_B \simeq 0.25 - 0.30 \text{ fm}^{-3}$ ), whereas the universal-coupling scenario only develops strangeness at somewhat higher densities (above  $n_B \simeq 0.30 \text{ fm}^{-3}$ ). These trends hold for both  $\zeta = 0.040$  and  $\zeta = 0.129$ .

By contrasting the top and bottom rows of Fig. 4, we see that introducing the strange scalar meson  $\sigma^*$  slightly increases the overall level of attraction in the hyperonic sector. This effect mildly enhances the strangeness content, lowering hyperon thresholds by a small margin and allowing  $Y_S$  to reach slightly higher values at a given density. This feature is most visible in the  $SU(6)$  coupling scheme, as long as this is the choice that most favors the creation of the  $\Lambda$  hyperons, due to the attractive potential that is explicitly taken into account, according to equation (49).

Importantly, however, the global behavior of  $Y_S(n_B)$  remains essentially unchanged: the presence of the strange scalar meson  $\sigma^*$  shifts the curves but does not qualitatively alter their ordering or slope. The same conclusion applies to both  $\zeta$  values and all coupling prescriptions.

The six panels in Fig. 5 reorganize the same information by fixing the thermodynamic state (from left to right:  $S/A = 1$  with neutrino trapping,  $S/A = 2$  without neutrinos, and  $T = 0$ ) and showing the dependence on both coupling scheme and  $\zeta$  simultaneously. In the  $S/A = 1$  neutrino-trapped case, the presence of a large leptonic fraction increases the electron chemical potential, which suppresses negatively charged hyperons. Accordingly, despite the available thermal energy, the threshold density of hyperon creation does not decrease as much as one might expect, compared to the case of  $T = 0$ ; for the same reason, the strangeness fraction  $Y_S$  does not present a pronounced increase and remains below its value in the other two cases ( $S/A = 2$  and  $T = 0$ ).

In the  $S/A = 2$  case (center panels 5), thermal effects become more important. The earlier appearance of hyperons is evident, and the differences among the coupling schemes manifest primarily in the slope of  $Y_S(n_B)$ :  $SU(6)$  maintains the most rapid growth, universal coupling ( $U$ ) the slowest, and Moszkowski coupling scheme ( $M$ ) remains intermediate. The dependence on  $\zeta$  follows the same non-universal pattern seen earlier –  $SU(6)$  shows larger strangeness for the stiffer EoS ( $\zeta = 0.040$ ), whereas universal coupling ( $U$ ) yields larger  $Y_S$  for the softer parametrization ( $\zeta = 0.129$ ), indicating that the interplay between stiffness and hyperon dynamics persists even at higher temperatures.

In the cold, neutrino-free case (right panels of Fig. 5), threshold behavior is sharpest, and, unlike the finite-temperature cases, the onset density is distinct for each coupling scheme:  $SU(6)$  and Moszkowski ( $M$ ) couplings allow hyperons to appear at somewhat lower densities, while universal coupling ( $U$ ) delays their emergence. The adjustable parameter  $\zeta$  influences the growth rate of

the strangeness fraction: for  $SU(6)$ , the stiffer model ( $\zeta = 0.040$ ) produces a noticeably faster rise in  $Y_S$ , whereas for the universal prescription ( $U$ ), increasing  $\zeta$  has the opposite effect, leading to larger  $Y_S$  in the softer model. As before, Moszkowski couplings ( $M$ ) are only mildly sensitive to  $\zeta$ . These patterns emphasize that, in the cold regime, the influence of the hyperon-meson couplings dominates the early behavior of  $Y_S$ , while the parameter  $\zeta$  modulates the high-density behavior.

Finally, the top and bottom rows again show that the inclusion of the strange scalar meson  $\sigma^*$  has an effect that is concentrated at higher densities: once hyperons are present, the additional attractive channel slightly enhances the efficiency of strangeness growth but does not modify the ordering or density dependence of the curves. Its influence remains subdominant compared to the thermal state, the presence or absence of neutrino trapping, and the chosen hyperon-meson coupling scheme.

To conclude our analysis, we now provide a set of general remarks regarding the particle populations – defined as the number density of each species normalized by the total net baryon density – without attempting an exhaustive case-by case examination. Except for antiparticles, the populations here shown are given by the *net* particle fraction.

First, in purely nucleonic matter (Fig. 6), where hyperons are absent and the composition is limited to neutrons, protons, electrons, and muons, the particle fractions vary much more mildly than in strange matter. Because fewer degrees of freedom participate in the competition for chemical equilibrium, the relative abundances of  $n$ ,  $p$ ,  $e^-$ , and  $\mu^-$  tend to stabilize at comparatively low densities, typically around  $0.2 \text{ fm}^{-3}$ , an effect that is even more pronounced at finite temperature. In such cases, beta-equilibrium is maintained with relatively small rearrangements in the isospin and leptonic sectors.

Including hyperons, we show results for the different coupling schemes in Figs. 7-9. In these cases, for any fixed entropy per baryon, neither the variation of the parameter  $\zeta$  nor the inclusion of the strange scalar meson  $\sigma^*$  qualitatively alters the overall structure of the particle-population curves or the ordering in which different species appear. Instead, the dominant source of variation is the meson-hyperon coupling scheme. The universal ( $U$ ) and Moszkowski ( $M$ ) prescriptions behave rather similarly: in particular, they predict exactly the same order of hyperon appearance in all finite temperature scenarios. This is expected, since both schemes assign identical values of meson-hyperon coupling constants to all strange baryons, according to equations (46) and (47). The  $SU(6)$  scheme, by contrast, employs symmetry-motivated but particle-dependent coupling constants, as prescribed in equation (48); consequently, it leads to a far more distinctive pattern in the emergence and growth of hyperonic species. One peculiar characteristic of this coupling scheme is the suppression of the  $\Sigma$  baryons and the favoring of the  $\Xi$  baryons, which can be explained by the assumption of a repulsive optical

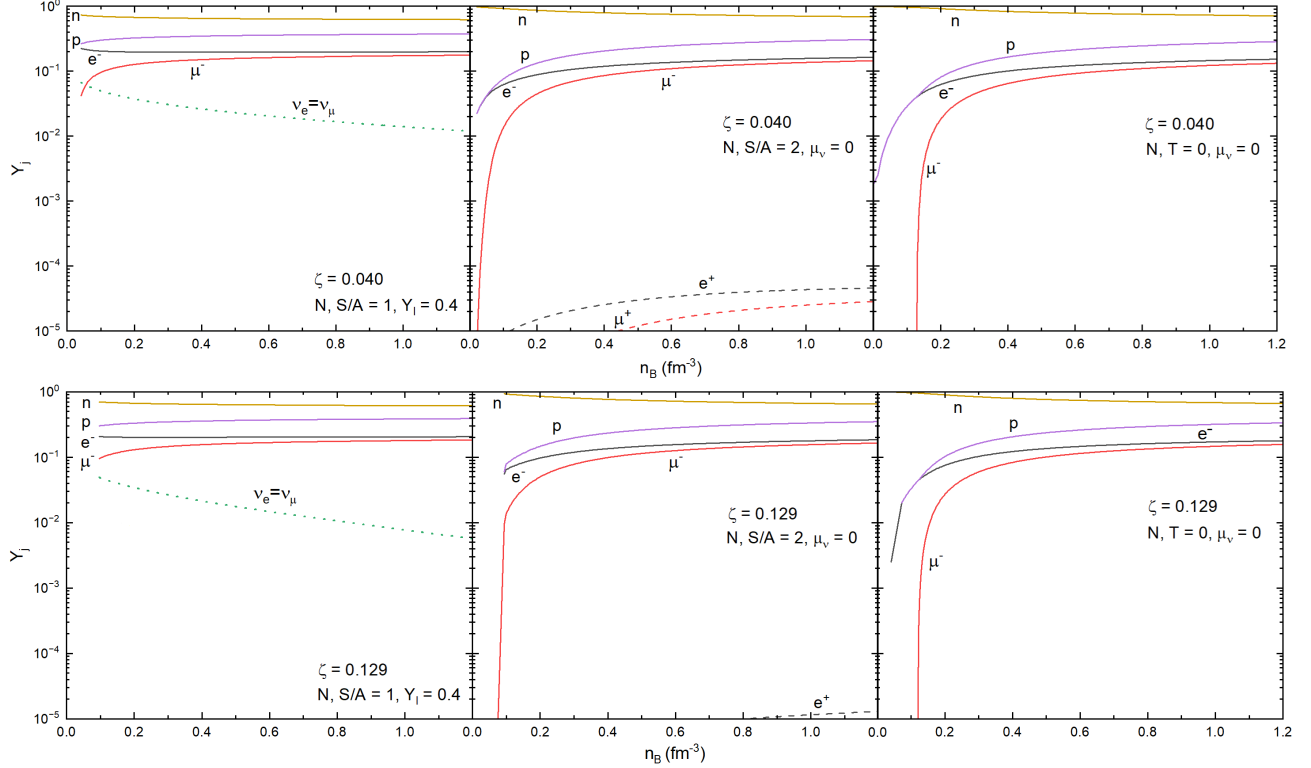


FIG. 6. **Populations of particles – Pure nucleonic matter (N):** Particle fraction ( $Y_j$ ) as a function of baryon density ( $n_B$ ). The different panels show different proto-neutron star evolution snapshots (left/center/right) and different MBF parameterizations (top vs. bottom). Antiparticles appear in dashed lines (center panels only).

potential for the first and an attractive optical potential for the latter when computing the coupling constants  $g_{\sigma\Sigma}$  and  $g_{\sigma\Xi}$ , according to equation (49).

In line with the previously established ordering of total strangeness fractions ( $U > M > SU(6)$ ), one observes that in the universal scheme ( $U$ ) the population of each hyperon species typically saturates below  $\sim 0.1 \text{ fm}^{-3}$ . Under Moszkowski couplings ( $M$ ), this range increases to roughly  $0.1\text{--}0.2 \text{ fm}^{-3}$ , while the  $SU(6)$  prescription yields the highest hyperon fractions, typically above  $0.2 \text{ fm}^{-3}$ . This trend reflects the increasing amount of attractive interaction experienced by the strange baryons as one moves from  $U$  to  $M$  to  $SU(6)$ , modifying both the chemical potentials and the competition among species.

As noted earlier, the influence of the strange scalar meson  $\sigma^*$  remains modest in most situations, except in the case of antiparticles (shown as dashed lines in Figs. 6-9). Antiparticles (namely, antileptons) acquire non-negligible abundances only in the  $S/A = 2$  case, where high temperatures generate strong thermal pair production. In this regime, the additional attraction mediated by  $\sigma^*$  noticeably enhances antiparticle populations at high densities. A second visible effect occurs in the universal coupling scheme at  $T = 0$ : here, the inclusion of  $\sigma^*$  actually reverses the order in which the  $\Lambda^0$  and  $\Sigma^-$  hyperons appear, highlighting the sensitivity of threshold competition to even relatively weak strange-sector inter-

actions.

However, examining each row of panels – corresponding to the thermal evolution from a hot, lepton-rich PNS to a cold, deleptonized NS – reveals that the particle-population dynamics in the three regimes differ substantially from one another. For  $S/A = 1$  with fixed lepton fraction  $Y_l = 0.4$ , neutrinos (dotted lines) are trapped. Here, thermal energy lowers the thresholds for all six hyperonic species, causing them to appear earlier than in the cold-matter case, typically between  $0.2$  and  $0.7 \text{ fm}^{-3}$ . Their growth, however, is comparatively moderate, and they do not reach large fractions. Because the lepton fraction is fixed, the populations of  $n$ ,  $p$ ,  $e^-$ , and  $\mu^-$  resemble those of purely nucleonic matter: they vary smoothly and exhibit far less restructuring than in neutrino-free scenarios. This reflects the strong constraint imposed by lepton trapping, which prevents drastic changes in proton and lepton fractions even as hyperons emerge.

In the  $S/A = 2$  case, now without neutrinos and at higher temperatures, thermal effects become so significant that all six hyperonic species are already present at densities around  $0.2 \text{ fm}^{-3}$ , only slightly above saturation. This behavior is robust across all values of the adjustable parameter  $\zeta$  and all meson-hyperon coupling schemes. Strong thermal pair production, reduced degeneracy pressure, and the enhanced role of temperature in

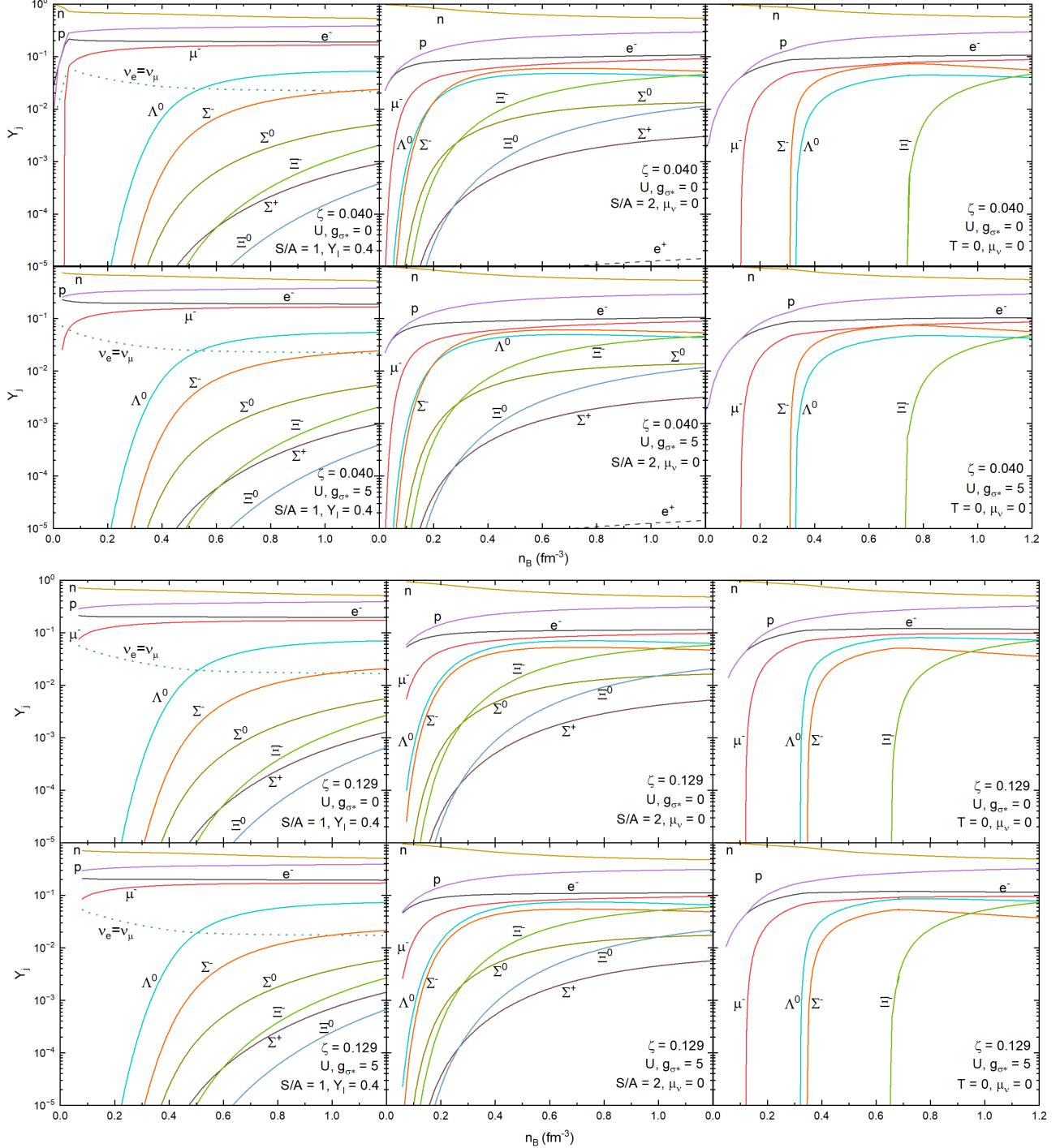


FIG. 7. **Populations of particles – Universal coupling ( $U$ ):** Same as Fig. 6 but for the universal coupling scheme for hyperons. Second and forth rows show different strange scalar meson parameterizations.

equilibrium conditions combine to lower hyperon thresholds dramatically. As a result, the composition of matter in this regime is already deeply strange even at relatively modest baryon densities, illustrating the profound impact of finite-temperature physics on the onset and evolution of strangeness.

Finally, in the cold, neutrino-free case ( $T = 0$ ), the composition is governed purely by the balance of chemical potentials and the competition between baryonic rest masses and interaction energies. As a consequence, hyperons emerge later than in both finite-temperature scenarios, typically above  $\sim 0.25 \text{ fm}^{-3}$ , and their appear-

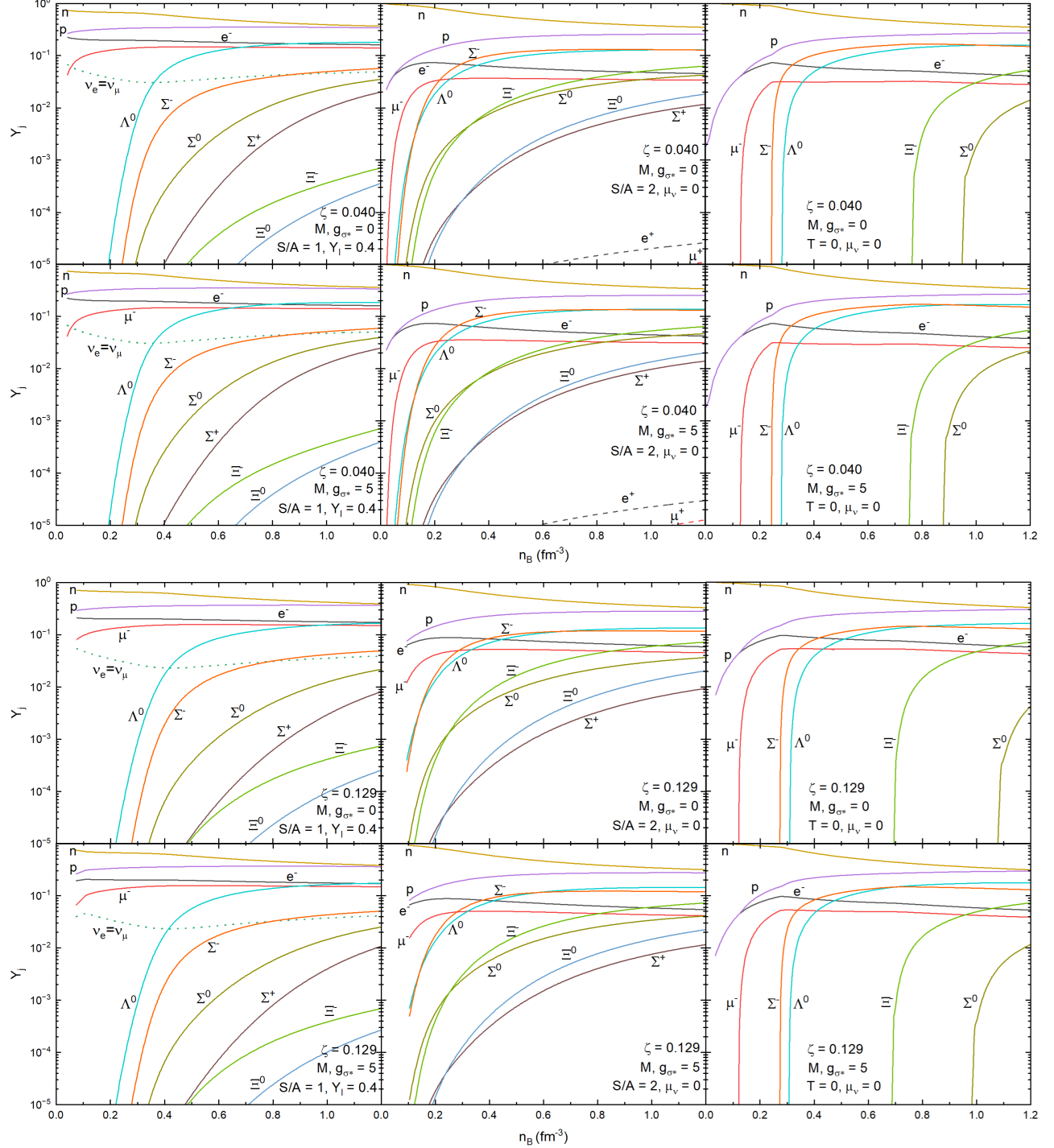


FIG. 8. **Populations of particles – Moszkowski coupling ( $M$ ):** Same as Fig. 7 but for the Moszkowski coupling scheme for hyperons.

ance occurs in a wider and more sharply defined sequence. Once they do appear, however, their populations grow substantially faster—particularly under the  $SU(6)$  coupling scheme—because cold matter maintains large degeneracy pressures, making additional degrees of freedom highly energetically favorable once their thresholds

are crossed. In this regime, the ordering of hyperon onset is most clearly expressed: the  $SU(6)$  and Moszkowski prescriptions predict early emergence of the  $\Lambda$  and  $\Sigma^-$ , whereas the universal scheme delays their appearance to higher densities, consistent with its weaker effective attraction in the strange sector.

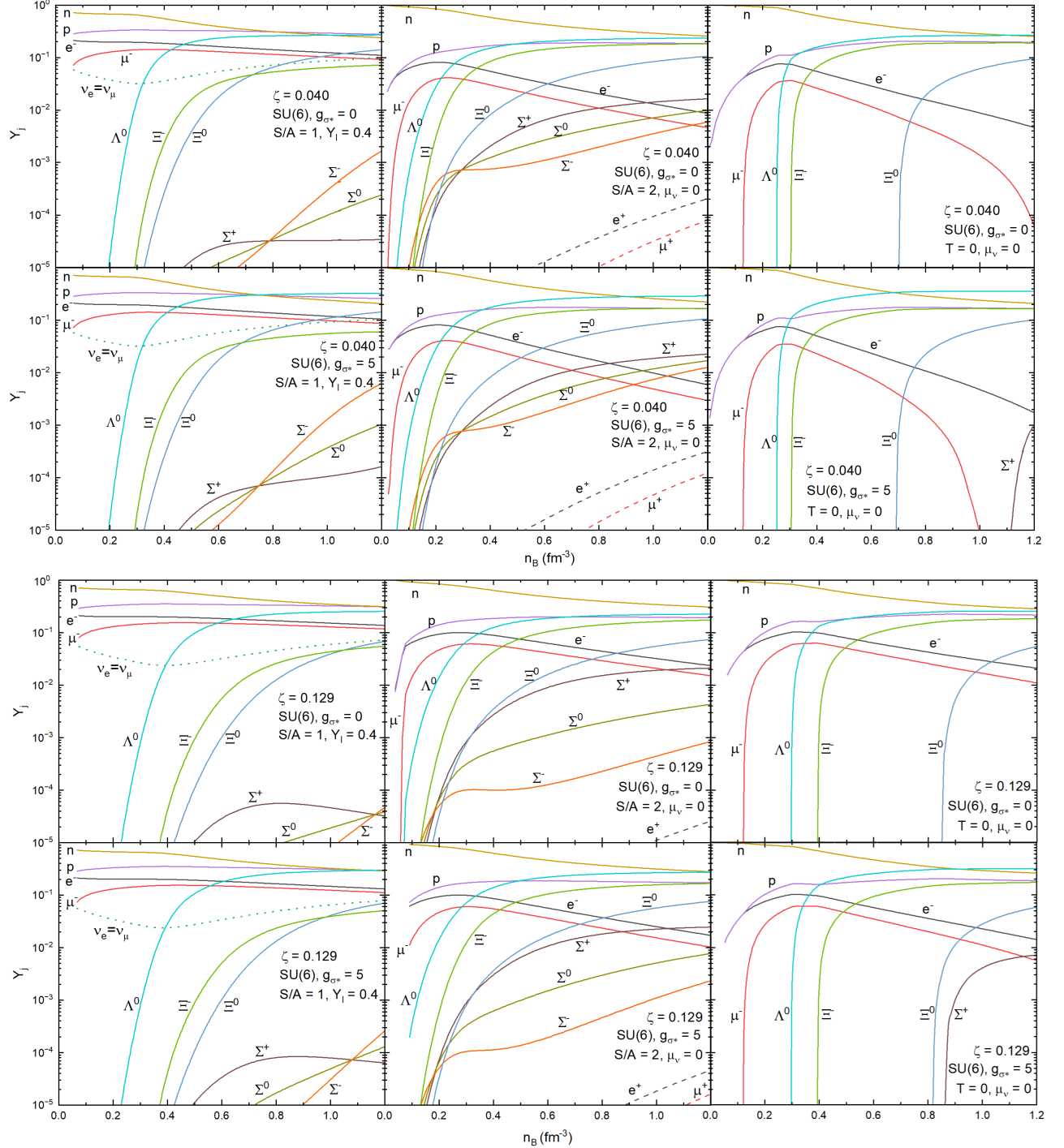


FIG. 9. **Populations of particles – SU(6):** Same as Fig. 7 but for the SU(6) coupling scheme for hyperons.

At zero temperature, lepton populations also behave differently. Without neutrino trapping and without thermal smearing of the Fermi-distributions, the electron and muon fractions decrease more rapidly once negatively charged hyperons ( $\Sigma^-$  and  $\Xi^-$ ) become energetically accessible. This reflects a mechanism of charge replacement, wherein hyperons partially assume the role of leptons in maintaining charge neutrality. Accordingly, the

proton fraction decreases at a slower rate, and the neutron fraction grows more steadily compared to the hotter, neutrino-rich cases. The absence of thermal pair creation also suppresses antiparticle populations entirely, leaving the strange sector dominated exclusively by hyperons.

Taken together, these results for the fraction of strangeness  $Y_S$  and for the populations of particles  $Y_j$  illustrate the multifaceted competition that governs

strangeness production in dense matter, i.e., the strong and nonlinear interplay among temperature, neutrino content, and the meson–hyperon interaction scheme in determining the microscopic composition of matter inside PNs and fully evolved NSs.

### C. Temperature profiles

The temperature profiles displayed in Figs. 10 and 11 illustrate how different choices the adjustable parameter ( $\zeta = 0.040$  and  $\zeta = 0.129$ ), together with distinct meson–hyperon coupling schemes, influence the thermal response of dense hadronic matter at finite entropy. The curves show the temperature  $T(n_B)$  for two thermodynamic conditions: (i) fixed entropy per baryon  $S/A = 1$  with trapped neutrinos, corresponding to a fixed lepton fraction  $Y_l = 0.4$ ; and (ii) fixed entropy per baryon  $S/A = 2$  with  $\mu_\nu = 0$ , representing a later stage of proto-neutron star evolution after neutrino diffusion [59, 60]. This comparison highlights the role of hyperons at finite temperature and different lepton contents.

For both  $\zeta$  values (top and bottom panels), the black curves correspond to purely nucleonic matter, and they systematically display the highest temperatures for a given density. Introducing hyperons softens the EoS [57, 75], because these additional degrees of freedom share the baryon number and reduce the nucleon Fermi pressure. At fixed entropy, a softer EoS tends to produce lower temperatures, since the available thermal energy is distributed among more baryonic species. This explains the ordering observed across all coupling sets: nucleonic matter ( $N$ )  $>$  universal coupling ( $U$ )  $>$  Moszkowski coupling ( $M$ )  $>$  spin-flavor symmetry coupling ( $SU(6)$ ). The  $SU(6)$  scheme, which incorporates quark-model symmetry arguments [51, 57], yields the weakest vector-meson–hyperon repulsion and thus the earliest onset of hyperons, leading to the lowest temperature profiles.

Comparison between Figs. 2 and 10 makes it clear how misleading the mere observation of the behavior of the equation of state can be: even though the  $p \times \varepsilon$  curves for pure nucleonic matter ( $N$ , black curves) and the universal coupling scheme ( $U$ , green curves) are quite close, almost coincident, these two cases exhibit completely distinct temperature profiles (note that, in Fig. 2, the black and green curves almost overlap; though, in Fig. 10, they are far apart, especially at higher densities).

Still in Fig. 10, the difference between the dotted ( $S/A = 1$ , neutrino-rich) and dashed ( $S/A = 2$ , neutrino-free) curves further illustrates the role of lepton trapping. At fixed density,  $S/A = 2$  corresponds to a hotter configuration. Neutrino trapping ( $S/A = 1$ ,  $Y_l = 0.4$ ) enhances the electron fraction and thus the proton fraction via charge neutrality, producing a more symmetric composition and delaying the appearance of negatively charged hyperons such as  $\Sigma^-$  [59, 60]. This delay is visible as gentler slopes in the hyperonic temperature curves of the neutrino-rich case. A better understanding of this

TABLE V. Temperature (in MeV) reached for baryon density  $n_B = 1.2 \text{ fm}^{-3} \simeq 8 n_0$  in different configurations of the MBF Model and two scenarios of finite entropy per baryon ( $S/A$ ). Here,  $n$  stands for pure nucleonic matter. These results consider  $g_{\sigma^*} = 0$ .

$S/A$	$\zeta$	$SU(6)$	$M$	$U$	$N$
1	0.040	16	19	23	29
1	0.129	16	18	21	26
2	0.040	43	46	52	65
2	0.129	40	40	44	58

relation between the slope in the temperatures profiles and the populations of particles can be reached by comparing Figs. 10 and 11 with the figures showing particle fractions in Section III B.

A comparison between the left panel ( $\zeta = 0.040$ ) and the right panel ( $\zeta = 0.129$ ) in Fig. 10 highlights the influence of the many-body forces in our model. Smaller values of  $\zeta$  correspond to stiffer EoSs because the influence of the scalar mesons is weaker, allowing the vector field to grow faster with density [76]. This is reflected in the temperature curves: for  $\zeta = 0.040$ , all profiles – especially the nucleonic ones ( $N$ ) – increase more steeply with  $n_B$ . In contrast, the softer EoSs ( $\zeta = 0.129$ ) lead to flatter temperature curves at high densities. Additionally, a larger  $\zeta$  lowers the density threshold for hyperon onset, since the reduced vector repulsion makes it energetically favorable to populate hyperons earlier, smoothly redistributing the baryon population.

At low densities, all curves in Fig. 10 converge regardless of the coupling prescription or  $\zeta$  value. Here, the thermal behavior is dominated by nucleons and leptons, because of the typical suppression of hyperons at sub-saturation densities [59]. Differences among EoS parameterizations become significant only above  $\sim 0.25 - 0.30 \text{ fm}^{-3}$ .

For the maximum baryon density depicted in Fig. 10 ( $n_B = 1.2 \text{ fm}^{-3} \simeq 8 n_0$ ), temperature lies in the range 16–23 MeV for hyperonic matter and reaches  $\simeq 29$  MeV for pure nucleonic matter when  $S/A = 1$ ; considering  $S/A = 2$ , this temperature lies in the range 40–52 MeV for hyperonic matter and reaches  $\simeq 65$  MeV for pure nucleonic matter. These results are detailed in Table V.

In Fig. 11, the two upper or lower panels show the temperature profiles for fixed thermodynamic conditions ( $S/A = 1$ ,  $Y_l = 0.4$  on the left;  $S/A = 2$ ,  $\mu_\nu = 0$  on the right) and provide a complementary view to Fig. 10. Here, both values of the adjustable parameter  $\zeta$  are displayed together, allowing an evaluation of how EoS stiffness affects the temperature at a given evolutionary stage. Solid curves correspond to  $\zeta = 0.040$  (stiffer EoS) and dashed ones to  $\zeta = 0.129$  (softer EoS), while the color scheme distinguishes the different hyperon–meson coupling prescriptions as before.

Several robust patterns emerge. First, for any coupling scheme, the temperatures for  $\zeta = 0.040$  (solid lines) lie

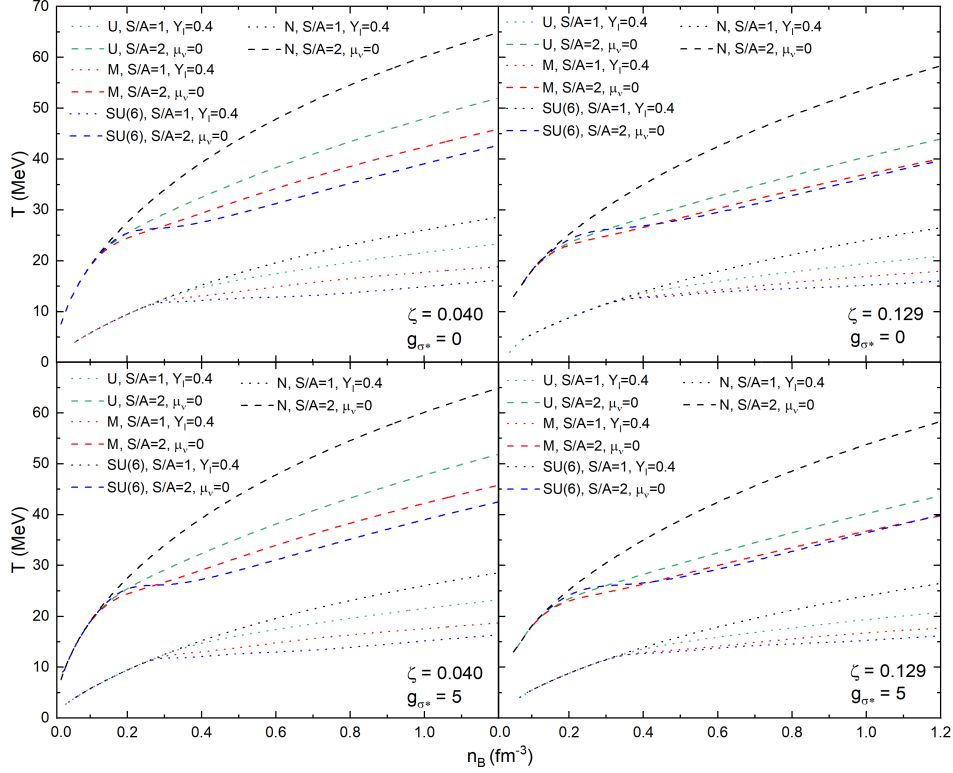


FIG. 10. **SET 1 (Temperature profiles):** Temperature ( $T$ ) as a function of baryon density ( $n_B$ ) for different proto-neutron star evolution snapshots, particle composition, and hyperon couplings. The different panels show different MBF (left vs. right) and strange scalar meson parameterizations (top vs. bottom).

above those for  $\zeta = 0.129$  (dashed lines), reflecting the fact that a stiffer EoS requires higher thermal excitation to achieve the same entropy per baryon. Second, the ordering of the curves is consistent across both panels: nucleonic matter yields the highest temperatures, followed by the universal ( $U$ ) and Moszkowski ( $M$ ) couplings, with the  $SU(6)$  prescription producing the lowest values. This trend mirrors the progressive softening of the EoS caused by hyperons.

Neutrino trapping also plays a clear role. In the  $S/A = 1$ ,  $Y_l = 0.4$  case, the presence of neutrinos delays hyperon formation, causing the hyperonic curves to cluster more closely and resemble the nucleonic one at low and intermediate densities. In contrast, in the neutrino-free  $S/A = 2$  scenario, hyperons appear earlier, enhancing both the model dependence and the separation between the solid and dashed curves.

Thus, Fig. 11 effectively illustrates how variations in EoS stiffness and hyperon interactions shape the thermal structure of proto-neutron-star matter at distinct moments of its evolution. Furthermore, by examining our results more closely and contrasting the top and bottom panels of Figs. 10 and 11, one can clearly see that introducing the strange scalar meson  $\sigma^*$  into the model has no noticeable impact on the general pattern of the temperature profiles.

Overall, these temperature profiles encapsulate three

fundamental physical effects: (i) the softening induced by hyperons, which decreases  $T$  at fixed entropy; (ii) the stiffening controlled by the adjustable parameter  $\zeta$ , with smaller  $\zeta$  producing higher temperatures and stronger density dependence; (iii) the influence of neutrino trapping, which delays hyperon formation and alters the symmetry energy, modifying the temperature evolution.

These results are consistent with the thermodynamic behavior predicted by other finite-temperature RMF models with hyperonic degrees of freedom [57, 59, 77] and are relevant for the early evolution of PNS and hot, dense hadronic matter in general. In particular, also note the consistency of the data shown in Figs. 10 and 11 with the following results from effective-field models: Fig. 8 in reference [78], Fig. 4 in [66] and Fig. 3 in [65].

An additional point worth emphasizing is that the temperature profiles  $T(n_B)$  shown in Figs. 10 and 11 directly reflect the typical thermal stratification the interior of compact stars. As the baryon density increases – that is, as one moves from the outer core toward the inner stellar core –, the temperature is expected to rise significantly. The low-density outer regions are more efficient at radiating energy and therefore remain comparatively cool, whereas the dense inner layers are thermally opaque and retain heat more effectively, resulting in substantially higher temperatures. In this sense, the functional behavior of  $T$  as a function of  $n_B$  encapsulates the thermody-

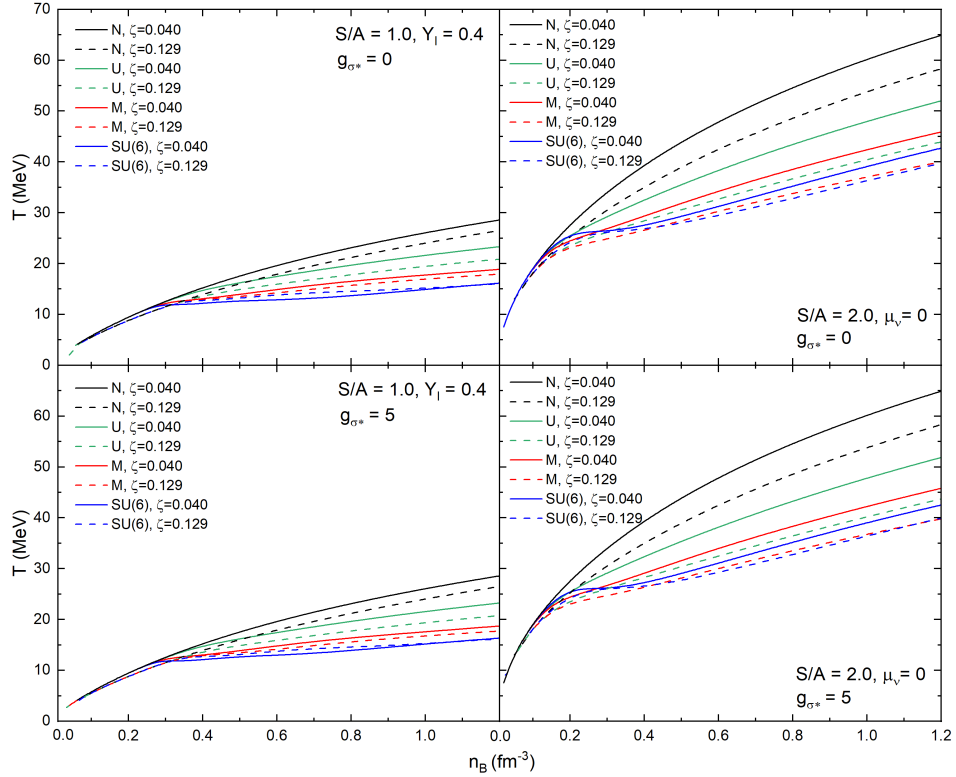


FIG. 11. **SET 2 (Temperature profiles):** Same as Fig. 10 but now the different panels show different evolution snapshots (left/right) and strange scalar meson parameterizations (top vs. bottom).

namic architecture of the star itself: a positive temperature gradient driven by increasing density and by the medium's varying ability to trap or release thermal energy.

#### D. Speed of sound

In nuclear matter, the speed of sound reflects how efficiently pressure builds up in response to changes in energy density, and thus reflects key information about the stiffness of the EoS. At low baryon densities, the system is relatively soft: the pressure increases only slowly with density, so the speed of sound is small. Around saturation density, the growth of pressure becomes steeper, and the speed of sound increases accordingly. At supranuclear densities, relevant for the cores of NSs, the behavior depends strongly on the underlying interactions: in many models the speed of sound continues to rise, reaching values significantly above those at saturation, but causality requires it to remain below the speed of light [79]. A particularly interesting feature is that some realistic EoSs (such as the MBF Model EoS) predict non-monotonic behavior, where the speed of sound stiffens rapidly above a few times saturation density and then levels off, or even softens again if different particles are created, e.g., strange matter (such as hyperons), exotic matter (such as exotic hadrons or hadron resonances), or

even deconfined quark matter. Because of that, the speed of sound may present structures such as kinks, bumps, jumps, spikes, wells, or plateaus [66, 80–94], and it has been shown that these structures can easily lead to ultra-heavy neutron stars, i.e., those with masses larger than  $2.5 M_{\odot}$  [95].

The speed of sound  $c_s$  for a fixed parameter  $\alpha$ , in units of the speed of light, can be obtained from the expression:

$$c_s^2|_\alpha = \frac{dp}{d\varepsilon}|_\alpha. \quad (56)$$

A variety of choices for  $\alpha$  may be found in literature, such as  $\alpha = s/n_B$ ,  $s$ ,  $n_B$ ,  $T$ ,  $\mu_B$ , etc. In neutron star matter, the quantity  $c_s^2|_T$  has been studied extensively with considerable experimental importance [96]; however, in the present work, for the reasons presented in the introduction of Section III, we study the speed of sound with the fixed parameter  $\alpha = S/A = s/n_B$ , i.e., along the isentropic curve.

The results of the MBF Model for the speed of sound for pure nucleonic matter, as well as for hyperonic matter, considering different values of  $\zeta$ ,  $g_\sigma^*$  and different temperatures are presented in Figs. 12 and 13. Firstly, in all cases: (i)  $c_s^2 \rightarrow 0$  for  $n_B = 0$  (what should be expected, since, as can be seen in Figs. 2 and 3,  $p$  is initially many orders of magnitude smaller than  $\varepsilon$ ); (ii)  $c_s^2$  increases more pronouncedly in the density region around saturation density. In this same region, for a given model

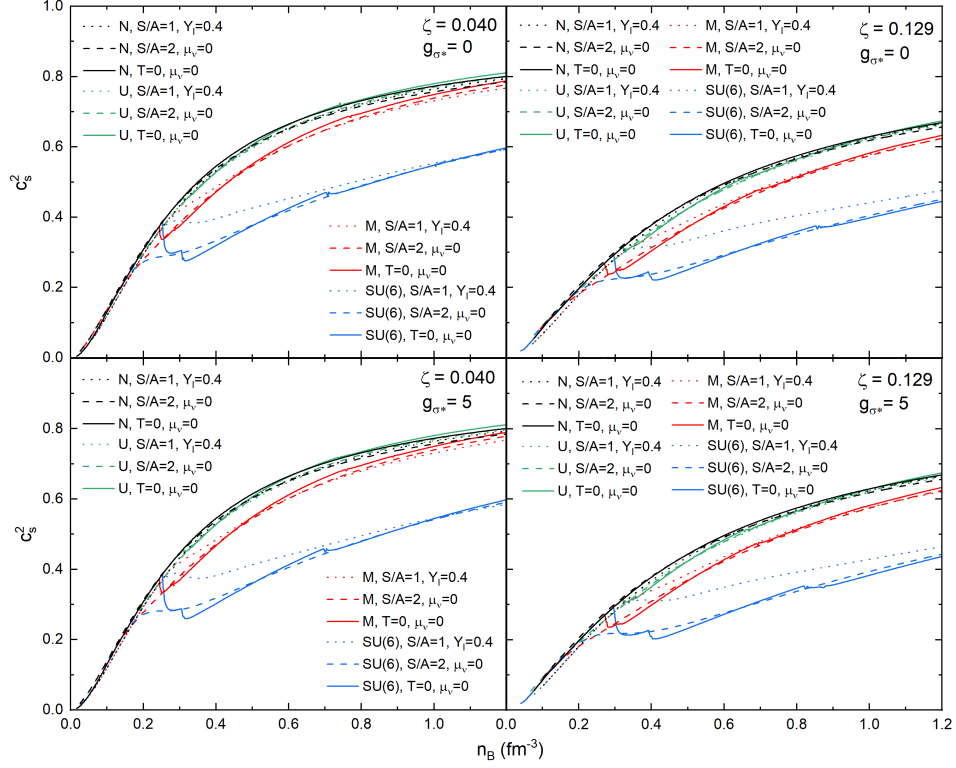


FIG. 12. **SET 1 (Speed of sound):** Speed of sound squared ( $c_s^2$ ) as a function of baryon density ( $n_B$ ) for different proton-neutron star evolution snapshots, particle composition, and hyperon couplings. The different panels show different MBF (left vs. right) and strange scalar meson parameterizations (top vs. bottom).

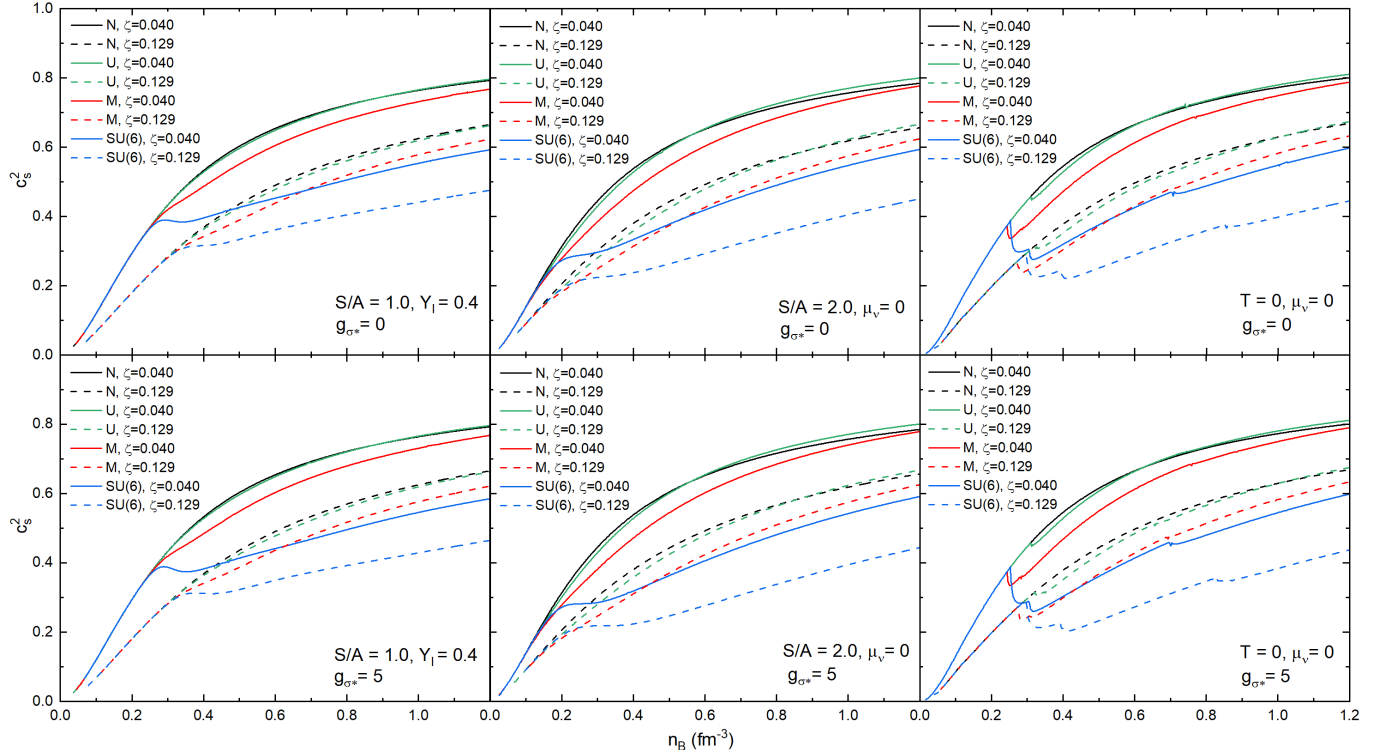


FIG. 13. **SET 2 (Speed of sound):** Same as Fig. 12 but now the different panels show different evolution snapshots (left/center/right) and strange scalar meson parameterizations (top vs. bottom).

parameterization ( $\zeta = 0.040$  or  $\zeta = 0.129$ , for example) and temperature choice (see Fig. 13), the curves for pure nuclear matter and for all the hyperon coupling schemes overlap, as expected, since the behavior of the corresponding EoSs will be the same until baryon density is high enough to enable the creation of hyperons: up to that point, in all cases, only nucleons and leptons are present, so the coupling constants chosen for the hyperons are irrelevant.

Next, as density increases, the slope of the  $c_s^2$  curve becomes smaller, tending to a constant value at high densities. Actually, given a specific configuration of the model, this value is approximately the same for  $T = 0$  and finite temperature, showing that, in this regime, thermal effects are less relevant than the influence of the high density itself (see Fig. 12, dotted/dashed vs. solid lines). At high densities, for  $\zeta = 0.040$  with the SU(6) coupling scheme,  $c_s^2$  approaches 0.6, while the other coupling schemes and pure nuclear matter give  $c_s^2 \simeq 0.8$ ; for  $\zeta = 0.129$  with the SU(6) coupling scheme,  $c_s^2$  approaches 0.45, while the other coupling schemes and pure nuclear matter give  $c_s^2 \simeq 0.65$ . These results show that the MBF Model strictly respects causality in all cases (both at zero and finite temperature), even in the presence of significant vector interactions ( $0 \leq c_s^2 \leq 1$ ).

On the other hand, due to the conformal symmetry of QCD, PQCD predicts that the speed of sound should approach the value realized in ultrarelativistic fluids  $c_s^2 = 1/3$  from below, at very high densities. Even though approaching the conformal limit depends on the values of the chemical potentials considered [97], it is known that PQCD calculations become reliable at sufficiently high densities,  $\sim 40 n_0$  [8, 98], far beyond those found in the interior of NSs. Clearly, the  $c_s^2 < 1/3$  limit is always violated in the MBF Model. Nevertheless, we must point out that between the low density ( $n_B \lesssim n_0$ ) and the very high density ( $n_B \gg n_0$ ) limits, the EoS is not accessible by first-principle methods and, therefore, the speed of sound is fundamentally unknown. As stated in reference [99], this uncertainty allows us to consider at least three possible behaviors for  $c_s$  as a function of density: (i) monotonic and sub-conformal:  $c_s^2 < 1/3$ ; (ii) non-monotonic and sub-conformal:  $c_s^2 < 1/3$ ; (iii) non-monotonic and sub-luminal:  $c_s^2 \leq 1$ .

Since the speed of sound is small at low densities and should approach the conformal limit at asymptotically large densities from below, behaviors (i) and (ii) would be preferred, and the condition  $c_s^2 < 1/3$  could then be regarded as a universal bound; notwithstanding, this bound conflicts with many clues from QCD and also from astrophysical constraints. Counterexamples to this bound emerge from QCD at large isospin density [100–103], two-color QCD [104–106], quarkyonic matter, models for high-density QCD [81, 107, 108], and models based on the gauge/gravity duality [109–111]. In addition, measurements of high-mass NSs [112–114] and theoretical calculations for the maximum gravitational mass of these objects [36, 115–118] suggest stiff EoSs with

$c_s^2 \gtrsim 1/3$  at  $n_B \gtrsim n_0$  [82]. Taking these data into account, scenario (iii) would be the most likely. As a matter of fact, a recent study [99] analyzed more than  $10^7$  EoSs that provide stellar models consistent not only with nuclear theory and PQCD, but also with astronomical observations, and concluded that EoSs with sub-conformal sound speeds are possible in principle but very unlikely in practice, being only 0.03% of the sample.

Taking a deeper look at our results and comparing the upper and lower panels of both Figs 12 and 13, it becomes evident that the inclusion of the strange scalar meson  $\sigma^*$  in the formalism does not affect the overall behavior of the speed of sound. Additionally, for pure nucleonic matter (represented by the black curves in Figs. 12 and 13), the speed of sound grows continuously; however, in hyperonic matter (represented by the colored curves in Figs. 12 and 13), when hyperons appear, typically at a few times nuclear saturation density, the speed of sound drops, because of the sudden “softening” the EoS, creating “bumps”. This means that the stiffness controls the speed of sound, as expected [119]. This effect is more pronounced in the curves for  $T = 0$  (both for  $\zeta = 0.040$  and  $\zeta = 0.129$ ): here, each peak corresponds to the creation of a different hyperon species (compare with the plots for the populations of particles in Section III B).

Our results are in good agreement with those obtained for other density dependent RMF models at  $T = 0$  (compare, for example, the upper-right and lower-right panels of Fig. 13 with Fig. 3 in reference [73]) and other effective models in general (see, for example, the right panel of Fig. 2 in [66]). When temperature increases, such as in the plots for  $S/A = 1$  and  $S/A = 2$ , the curves become smoother because of the creation of hyperons at lower densities, leading to the disappearance of the typical peaks found at  $T = 0$ . The predicted behavior of  $c_s^2$  as a function of density in the finite temperature case is compatible with the results obtained from different effective models (see, for example, the right panel Fig. 5 in [66], Fig. 16 in [120] and Fig. 6 in [121]).

## E. Compressibility

The study of compressibility in NSs is crucial because it determines how matter responds to changes in density at nuclear scales, directly influencing the stiffness of the EoS and, consequently, the star’s global properties. The compressibility controls the pressure at saturation density [122], as well as densities below and above, affecting the maximum mass and radius that NSs can achieve before collapsing into black holes [123], as well as the dynamics of phenomena such as supernovae and NS mergers [124]. The compressibility  $K$  of nuclear matter is calculated from its general definition in nuclear physics (valid for both zero and finite temperature):

$$K = 9 \frac{\partial p}{\partial n_B} . \quad (57)$$

Our results for this physical quantity are presented in Figs. 14 and 15, both for pure nucleonic and hyperonic matter, considering different values of  $\zeta$ ,  $g_\sigma^*$  and different temperatures.

One can easily notice that there is a clear parallel between the behavior of  $K$  and  $c_s^2$  in many aspects. In the first place, in all cases,  $K \rightarrow 0$  for  $n_B = 0$  and increases with density – although, differently from  $c_s^2$ ,  $K$  always increases and does not tend to a constant value at high densities. This growth can be regarded as monotonic for pure nuclear matter (black lines in Figs. 14 and 15); for hyperonic matter, on the contrary, the creation of the strange baryons tends to suddenly decrease the value of the compressibility in such a way that small bumps or peaks appear (see the colored lines in the plots), mainly for  $T = 0$ . This behavior is even more clear here, in the results for  $K$ , than in the corresponding results for  $c_s^2$ . Actually, the results for the compressibility are more sensitive to the peculiarities of each configuration of the model: note, for example, that, even though the behavior of pure nucleonic matter (black lines) and hyperonic matter with universal coupling ( $U$ , green lines) are still very similar, the corresponding curves for  $K$  are not as close as the ones for  $c_s^2$ , being the green lines (hyperonic matter with universal coupling  $U$ ) evidently below the black lines (pure nucleonic matter), making it clear that the presence of the hyperons leads to a less incompressible EoS; additionally, since the peaks are more pronounced here, it is easier to compare the densities where these peaks and bumps occur with de densities where new hyperon species are created, as shown in the plots in Section III B.

Moreover, once again, comparing the upper and lower panels of both Figs 12 and 13, it becomes evident that the inclusion of the strange scalar meson  $\sigma^*$  in the formalism does not affect the overall behavior of the compressibility. Furthermore, the results for  $K$  corroborate the stiffness ranking already established from the analysis of the EoSs in Section III A and the behavior of the speed of sound in Section III D: namely,  $\zeta = 0.040$  implies a more incompressible EoS than  $\zeta = 0.129$  (compare the left and right panels in Fig. 14), and, for a fixed  $\zeta$ , the increasing order of incompressibility is  $SU(6)$  coupling, Moszkowski ( $M$ ) coupling, and universal ( $U$ ) coupling. In Fig. 14, note, for example, that for  $\zeta = 0.040$  and  $n_B = 1.2 \text{ fm}^{-3}$  ( $\simeq 8n_0$ ),  $K$  reaches a value  $K \simeq 2300 \text{ MeV}$  for the  $SU(6)$  coupling (blue lines),  $K \simeq 3900 \text{ MeV}$  for the  $M$  coupling (red lines), and  $K \simeq 4600 \text{ MeV}$  for the  $U$  coupling (green lines). The compressibility for pure nucleonic matter is always slightly greater than its value for the  $U$  coupling.

Also, the results for  $K$  allow us a deeper insight into the effect of temperature on the stiffness of the EoS. In Fig. 14, it is possible to see that, for each configuration of the model (represented by the different colors), the dotted ( $S/A = 1$ ) and dashed ( $S/A = 2$ ) lines always lie above the solid line ( $T = 0$ ) of same color. That means that, in general, thermal effects make the EoS more incompressible. For a fixed value of  $\zeta$ , one can notice that

this increment in incompressibility due to temperature is more pronounced in those EoSs which tend to be less incompressible *a priori* due to their particular hyperon coupling scheme (namely,  $M$  and  $SU(6)$ ); on the other hand, this stiffening due to temperature is more subtle in those EoSs which tend to be softer *a priori* (namely,  $U$  and pure nucleonic matter). This influence of temperature on  $K$  also emerges from the comparison between two different choices for the adjustable parameter  $\zeta$ , shown side-by-side in Fig. 14: the wider separation between the solid lines and the dashed and dotted lines of same color is unmistakably wider in the right panels (representing  $\zeta = 0.129$ , the least incompressible EoSs) in comparison with the left panels (representing  $\zeta = 0.040$ , the most incompressible EoSs).

The more incompressible configurations have this property because they either contain no hyperons (pure nucleonic matter,  $n$ ) or have a tendency toward hyperon suppression ( $U$  scheme). In these cases, the EoS is already quite stiff by its very nature, so that a small increase in temperature (as in the case  $S/A = 1$ ) does not significantly modify the EoS's behavior with respect to its compressibility: note that, for nucleonic matter and the universal coupling scheme ( $U$ ), the dashed ( $S/A = 1$ ) and solid ( $T = 0$ ) lines overlap; however, with increasing temperature ( $S/A = 2$ ), the thermal effect is already sufficient to increase the incompressibility of the EoS, leading to higher values of  $K$  (which can be seen by the fact that the dashed lines are above the solid lines in these two cases).

However, for those coupling schemes that enhance the creation of hyperons, namely  $M$  and  $SU(6)$ , the EoS is naturally more compressible, so that even at relatively low temperatures ( $S/A = 1$ ), there is no significant increase in the hyperon fraction, but thermal effects already cause a more pronounced increase in  $K$  – hence, for the red ( $M$ ) and blue ( $SU(6)$ ) curves, the dotted lines lie markedly above the corresponding solid lines. For even higher temperature regimes ( $S/A = 2$ ), however, the reinforcement in the incompressible behavior of the EoS due to temperature increase is overcome by a significant increase in the hyperon fraction, facilitated by the substantial increment in the energy available to the system already at low densities, which reduces the EoS stiffness from the outset. For this reason, in Fig. 14, the dashed lines for the  $M$  (red) and  $SU(6)$  (blue) coupling schemes lie below the higher temperature lines (dotted lines).

In summary, there are two competing mechanisms that determine the compressibility  $K$ : the tendency for pressure to increase with increasing temperature, and the tendency for this quantity to decrease when the meson-hyperon coupling scheme facilitates the creation of these particles. In some cases, the first mechanism prevails; in others, the second is more relevant.

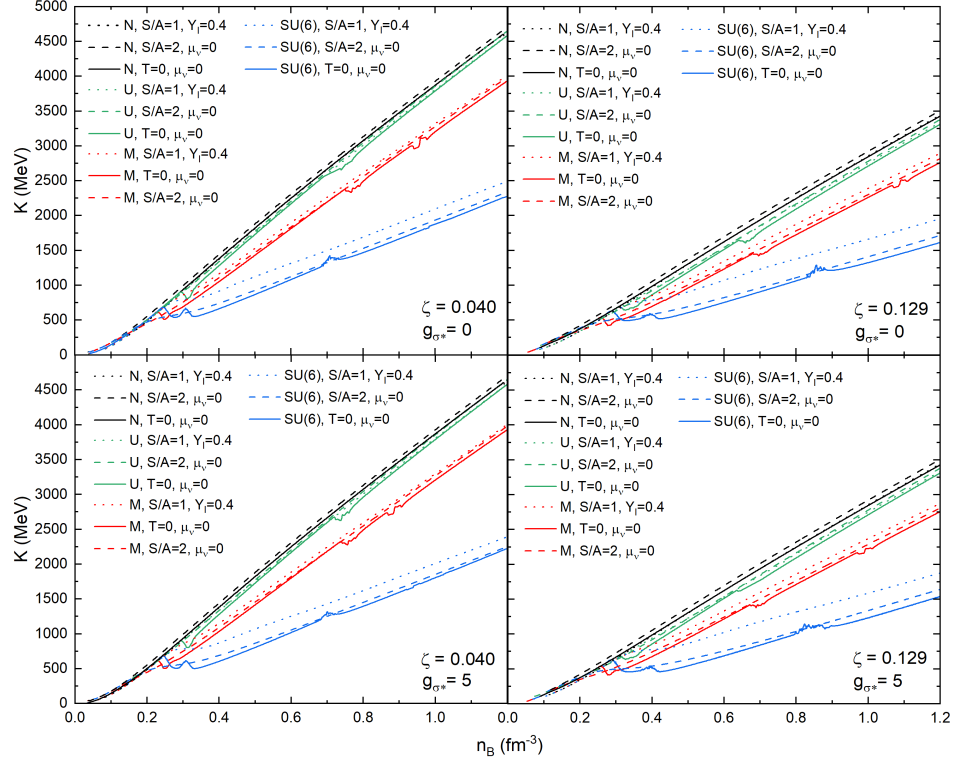


FIG. 14. **SET 1 (Compressibility):** Compressibility ( $K$ ) as a function of baryon density ( $n_B$ ) for different proto-neutron star evolution snapshots, particle composition, and hyperon couplings. The different panels show different MBF (left vs. right) and strange scalar meson parameterizations (top vs. bottom).

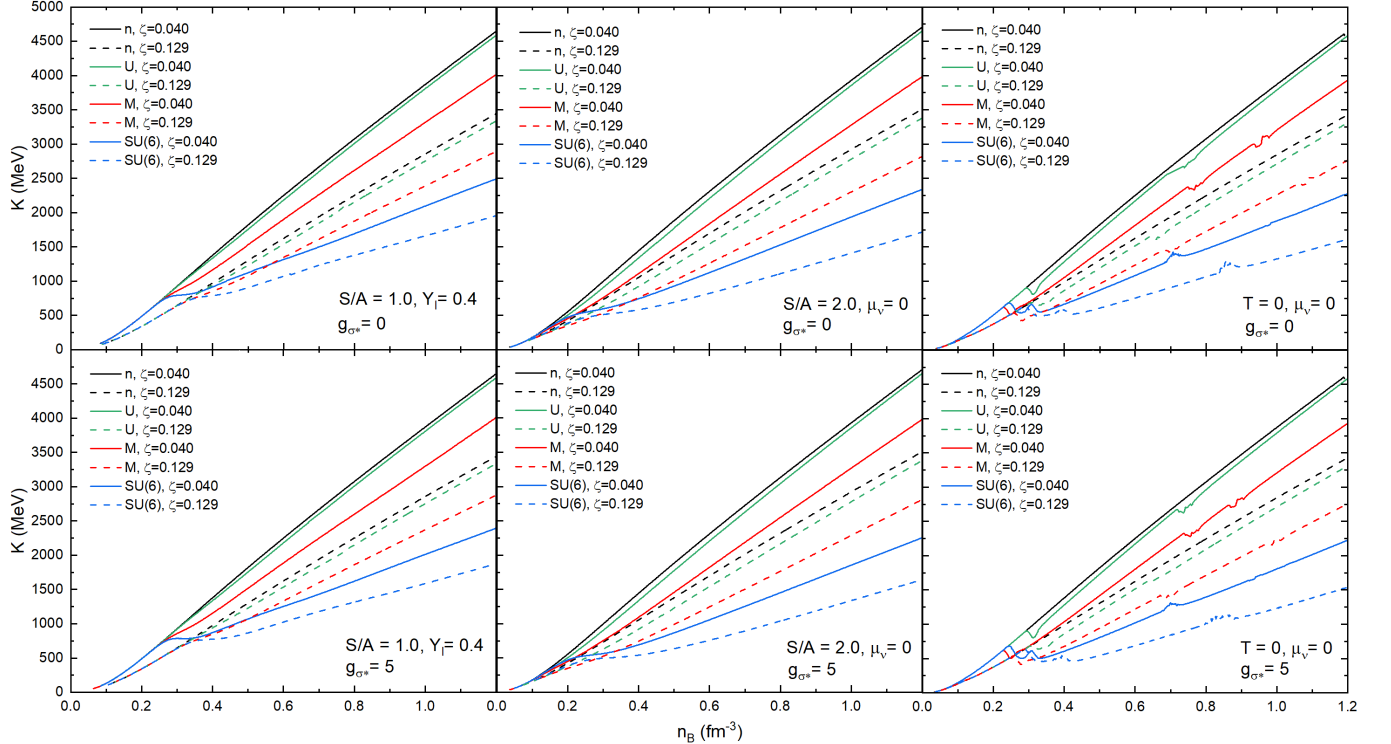


FIG. 15. **SET 2 (Compressibility):** Same as Fig. 14 but now the different panels show different evolution snapshots (left/center/right) and strange scalar meson parameterizations (top vs. bottom).

## F. Adiabatic index

The adiabatic index is a dimensionless parameter that characterizes how pressure responds to changes in density or energy density in a given thermodynamic process. In simple terms, it is another quantity that measures the stiffness or compressibility of matter. The adiabatic index  $\Gamma$  is related to the speed of sound  $c_s$  and can be directly obtained from the EoS:

$$\Gamma = \frac{\partial \ln p}{\partial \ln n_B} = \frac{n_B}{p} \frac{\partial p}{\partial n_B} = \frac{(p + \varepsilon)}{p} \frac{dp}{d\varepsilon} = \frac{(p + \varepsilon)}{p} c_s^2. \quad (58)$$

In the context of neutron star matter,  $\Gamma$  plays a central role in determining the internal structure and stability of the star, as long as it behaves as a sensitive indicator of phase changes and stability with respect to vibrations of a star [125–128]. Near the stellar surface, where the density is low and matter is only weakly degenerate,  $\Gamma$  tends to values close to those of nonrelativistic gases (around 5/3). As density increases, interactions between nucleons soften the equation of state, and  $\Gamma$  decreases, typically to values near 1–2. In the inner core, where matter may become ultrarelativistic or contain exotic components such as hyperons, quarks, or meson condensates,  $\Gamma$  can vary sharply, reflecting transitions in the microscopic composition and the stiffness of the EoS. Therefore, the behavior of  $\Gamma$  with density conceals important data about the microphysics of dense matter and strongly influences macroscopic observables. For example, the stability of a neutron star against radial oscillations depends on the average value of  $\Gamma$ : when  $\Gamma$  falls below about 4/3, the star becomes unstable to gravitational collapse [129, 130].

The adiabatic index is a weak function of density only for some special EoSs, namely those which present a very specific smooth dependence of the pressure on neutron and proton number densities (the EoSs which are based on the Skyrme-type energy density functionals, for example [130]). The remaining EoSs, constructed in the framework of many-body theories based on realistic nuclear Lagrangians, have a complicated density dependence, which reflects different contributions from various components of nuclear interaction. Moreover, it has been shown that the adiabatic index depends non-negligibly on the temperature and density, especially when hyperons are present; therefore, true thermal effects cannot be reproduced with the use of a constant  $\Gamma$  law [131]. The MBF Model consistently incorporates both dependencies, on density and temperature, as can be seen in Figs. 16 and 17.

The first noticeable feature, both for  $T = 0$  and finite  $T$ , is that, starting from  $\simeq 5/3$ , there is a sudden increase of  $\Gamma$  in the the low density regime ( $n_B < n_0$ ). This behavior can be easily understood if we consider the definition of  $\Gamma$  in the following form:  $\Gamma = (1 + \varepsilon/p) c_s^2$ . Here, one must first notice that, for  $n_B = 0$ , the factor  $c_s^2$  vanishes (see Figs. 12 and 13), and this would lead to  $\Gamma \rightarrow 0$  for  $n_B \simeq 0$ ; however, since  $p \ll \varepsilon$  in the low

density regime (see Figs. 2 and 3), the term  $\varepsilon/p$  assumes high numerical values and competes with the term  $c_s^2$ , quickly becoming dominant in that region. On the other hand, in the high density region, the slope of the EoS curves approaches a nearly constant value and  $c_s^2$  tends to stabilize; therefore, the adiabatic index also reaches a plateau, such that  $\Gamma \simeq 2$  for  $n_B \gtrsim 1.2 \text{ fm}^{-3}$  ( $\simeq 8 n_0$ ).

In the region of intermediate densities, the softening of the EoS is reflected in the density dependence of the adiabatic index. The index  $\Gamma$  drops at each hyperon threshold. At densities slightly higher than each hyperon threshold, the number density of hyperon species is small, i.e., these hyperons mainly interact with nucleons. Thus, the softening and associated drop of  $\Gamma$  strongly depend on the nucleon-hyperon interaction. This behavior is evident for the  $T = 0$  plots, both for  $\zeta = 0.040$  and  $\zeta = 0.129$  (see right panels of Fig. 17). Noticeably, the two configurations which hinder ( $U$ ) or suppress (pure nucleonic matter  $n$ ) hyperon creation exhibit a smoother behavior, even for  $T = 0$ . Differently, the  $M$  and  $SU(6)$  coupling schemes for hyperons cause striking drops in the adiabatic index.

These drops are clearly more pronounced for the  $SU(6)$  coupling, since this scheme is the one that plainly incorporates nucleon-hyperon interactions by taking into account, for example, the isospin proportion between nucleons and hyperons and also the potential depths of the hyperons in nuclear matter, according to equations from (48) to (49). Once again, the comparison with the plots for the populations of particles in Section III B can be enlightening to check the correspondence between the values of  $n_B$  where the drops in  $\Gamma$  occur and the threshold values of  $n_B$  for creation of each hyperon species. The results for  $\Gamma$  at  $T = 0$  obtained in this work exhibit the same general features derived from other effective models (see, for example, the left panel in Fig. 2 of reference [66]).

As usual, in the finite temperature cases ( $S/A = 1$  and  $S/A = 2$ ), the curves are much smoother, even for configurations that are rich in hyperons, since the thermal energy available favors the creation of these particles even when baryon density is low (see left and center panels of Fig. 17). The behavior of the adiabatic index  $\Gamma$  in the MBF Model at finite temperature is coherent with the predictions of different effective models (see Fig. 15 in reference [120] and the left panel of Fig. 5 in [66]).

It is important to notice that, in all configurations and cases here studied, the adiabatic index values provided by the MBF Model stay above the canonical limit for stability ( $\Gamma > 4/3$ ). Furthermore, comparison between the upper and lower panels of Figs. 16 and 17 corroborate that the presence of the strange scalar meson  $\sigma^*$  does not imply considerable modification in the key physical quantities calculated in the present work.

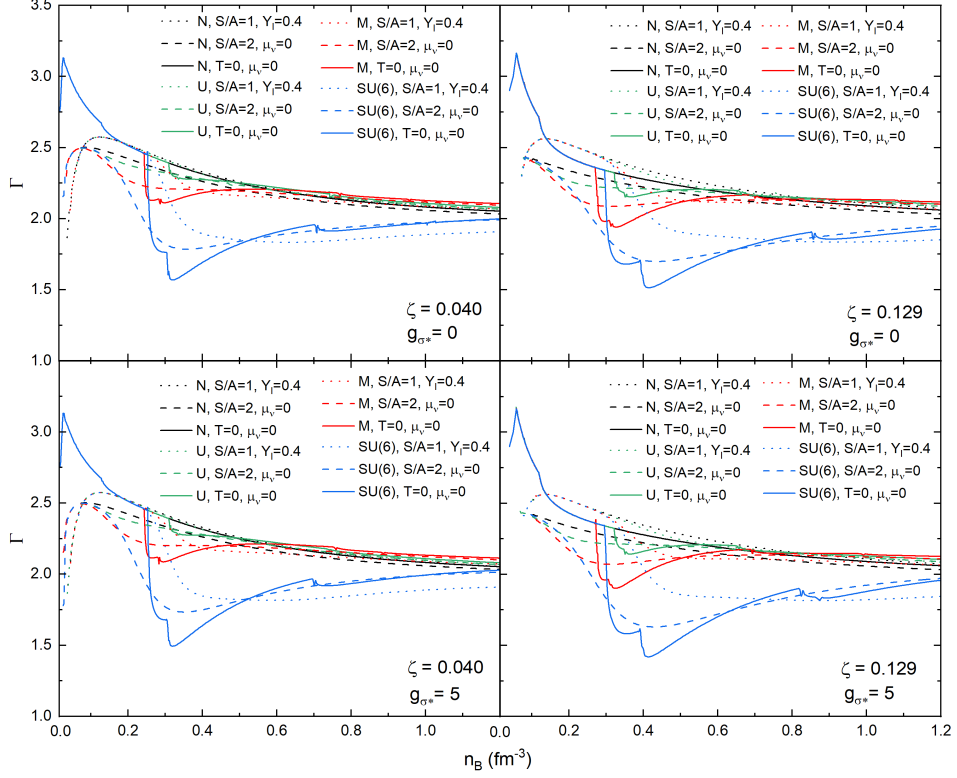


FIG. 16. **SET 1 (Adiabatic index):** Adiabatic index ( $\Gamma$ ) as a function of baryon density ( $n_B$ ) for different proto-neutron star evolution snapshots, particle composition, and hyperon couplings. The different panels show different MBF (left vs. right) and strange scalar meson parameterizations (top vs. bottom).

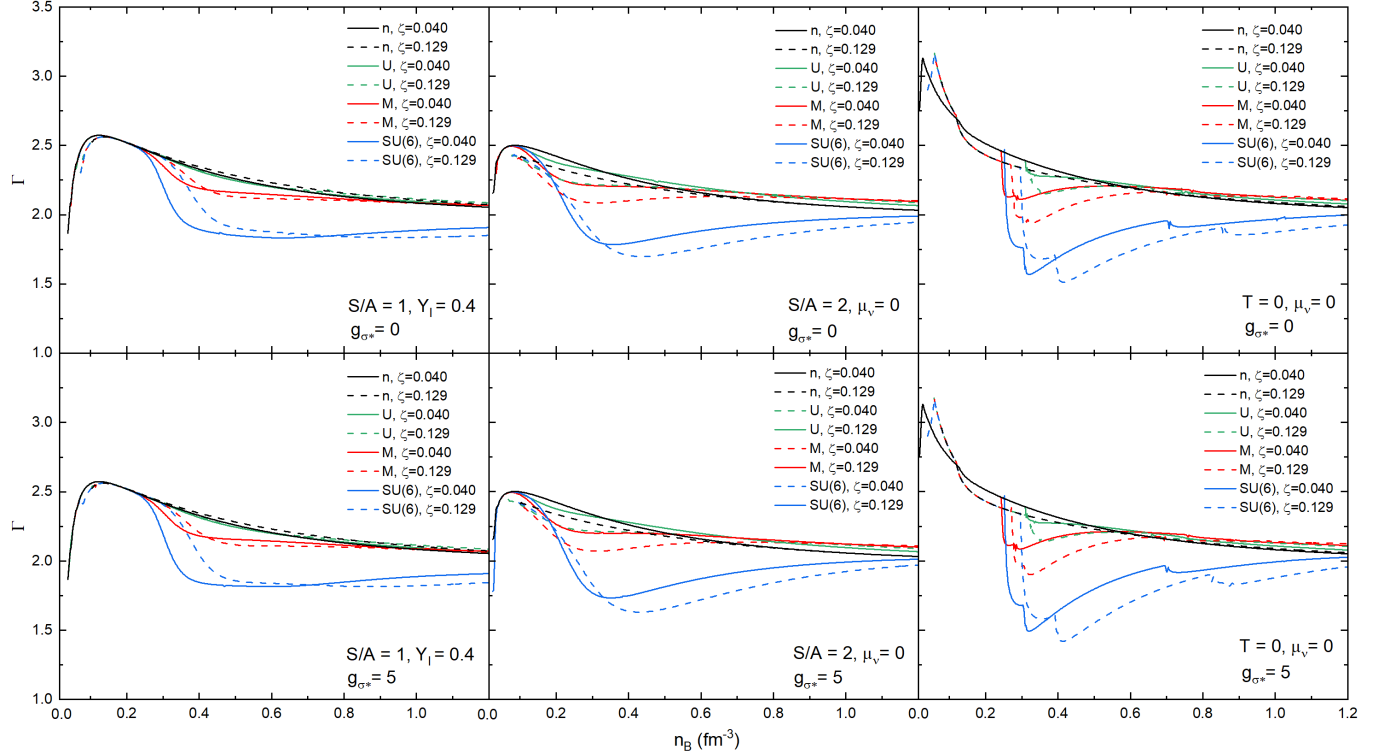


FIG. 17. **SET 2 (Adiabatic index):** Same as Fig. 14 but now the different panels show different evolution snapshots (left/center/right) and strange scalar meson parameterizations (top vs. bottom).

#### IV. MASS-RADIUS RELATION OF HOT AND COLD NEUTRON STARS

The global structure of neutron stars is determined by the interplay between gravity and the pressure generated by dense matter. In the framework of general relativity, this balance is encoded in the Tolman-Oppenheimer-Volkoff (TOV) equations, which describe the hydrostatic equilibrium of a spherically symmetric, nonrotating star composed of an isotropic fluid [132, 133]. These equations are the relativistic generalization of the classical Newtonian stellar structure equations and provide a direct connection between the microscopic physics contained in the equation of state (EoS) and macroscopic, observable stellar properties such as mass and radius. Considering  $G = c = 1$ , the TOV system can be expressed as

$$\frac{dp(r)}{dr} = -\frac{\varepsilon(r)M(r)}{r^2} \frac{[1 + p(r)/\varepsilon(r)][1 + 4\pi r^3 p(r)/M(r)]}{[1 - 2M(r)/r]}, \quad (59)$$

$$M(r) = \int_0^r 4\pi r'^2 \varepsilon(r') dr', \quad (60)$$

where  $p(r)$  is the pressure,  $\varepsilon(r)$  the energy density, and  $M(r)$  the enclosed gravitational mass at radius  $r$ . To solve these equations one specifies a central energy density  $\varepsilon_c$  and integrates outward until the pressure drops to zero, which defines the stellar radius  $R$ . The resulting gravitational mass  $M(R)$  yields a single point on the mass-radius curve. Repeating this procedure for a range of central densities produces the full sequence of equilibrium stellar configurations predicted by a given EoS.

The role of the EoS is therefore central: it supplies the functional relation  $p(\varepsilon)$  that closes the TOV system and encodes all relevant microphysical information, including the composition, interactions, and thermodynamic state of dense matter. Different model choices for the EoS – such as whether hyperons are included, what coupling schemes govern the interactions, or whether the matter is cold or thermally excited – lead to different predictions for the pressure at a given density. These differences, when fed into the TOV equations, manifest as distinct mass-radius relations and maximum mass limits. Because of this sensitivity, neutron-star observations serve as powerful constraints on the high-density EoS, while theoretical modeling provides the bridge between microscopic physics and astrophysical data for macroscopic stellar properties.

Thermal and compositional effects can significantly alter stellar structure, especially in the early life of a PNS. Finite entropy per baryon, the presence or absence of trapped neutrinos, and the possible appearance of new degrees of freedom such as hyperons all modify the energy density, pressure, and chemical potentials. Consequently, each thermodynamic scenario corresponds to a different EoS, and thus to a different family of TOV solutions. Tracking how the mass-radius relation evolves as the star cools and deleptonizes offers insight into the dynamical

transformation from a hot PNS to a cold, catalyzed neutron star. Figs. 18 and 19 illustrate this connection, showing how variations in the EoS driven by thermodynamics, composition, and the adjustable parameter  $\zeta$  give rise to qualitatively and quantitatively distinct TOV solutions.

In order to solve the TOV equations for cold neutron-star matter ( $S/A = 0$  or  $T = 0$ ), the cold neutron-star crust developed by Baym, Pethick and Sutherland (known as *BPS crust*), which includes an inner crust, an outer crust and an atmosphere [134], was merged with the various EoSs derived from the MBF Model. For the finite temperature cases, the hot proto-neutron-star crust developed by Lattimer and Swesty (with entropy per baryon  $S/A = 4$ , acting as a thermal mantle) was applied [135].

Fig. 18 corresponds to the first set of panels used earlier in this work (SET 1): each panel shows results for a fixed value of the adjustable parameter  $\zeta$  (left:  $\zeta = 0.040$ ; right:  $\zeta = 0.129$ ), while the different thermal scenarios ( $S/A = 1$  with neutrino trapping,  $S/A = 2$  without neutrinos, and  $T = 0$ ) appear as distinct curves following the standard color and line-type conventions for the hyperon coupling schemes. The lower set of panels (SET 2) employs the complementary strategy: each panel fixes a thermodynamic condition (left:  $S/A = 1$ ,  $Y_l = 0.4$ ; center:  $S/A = 2$ ,  $\mu_\nu = 0$ ; right:  $T = 0$ ,  $\mu_\nu = 0$ ) while displaying the EoS predictions for both  $\zeta$  values simultaneously. Taken together, these figures illustrate several crucial aspects of the stellar structure problem and the role played by hyperons, thermal effects, and neutrino trapping.

The first and most general observation in Fig. 18 is that thermal conditions strongly influence the general appearance of the mass-radius relation, even though, for both values of  $\zeta$ , the  $S/A = 1$  and  $S/A = 2$  curves do not shift the maximum mass to higher values compared to the cold  $T = 0$  case; however, the radius of stars of a given mass clearly tends to be larger at finite entropy, especially for  $S/A = 1$ , where the presence of trapped neutrinos increases the lepton fraction and, consequently, the proton fraction. This composition change delays the appearance of hyperons and modifies the stiffness of the EoS at intermediate densities.

The second striking feature is the consistent effect of  $\zeta$  across all thermodynamic regimes. For  $\zeta = 0.040$  (left panels in Fig. 18), the EoS is stiffer, leading to larger radii and higher maximum masses. Conversely, for  $\zeta = 0.129$  (right panels), the softening of the EoS is manifest: maximum masses are reduced, and the mass-radius curves shift downward and inward. These differences are especially pronounced in hyperonic matter, where the interplay between the scalar and vector meson fields is more delicate. The lower pair of panels makes these trends particularly clear, since the solid and dashed curves for  $\zeta = 0.040$  and  $\zeta = 0.129$  appear together. In all cases, the  $\zeta = 0.040$  configurations reach the highest maximum masses, above  $2 M_{\odot}$ , while  $\zeta = 0.129$  curves terminate

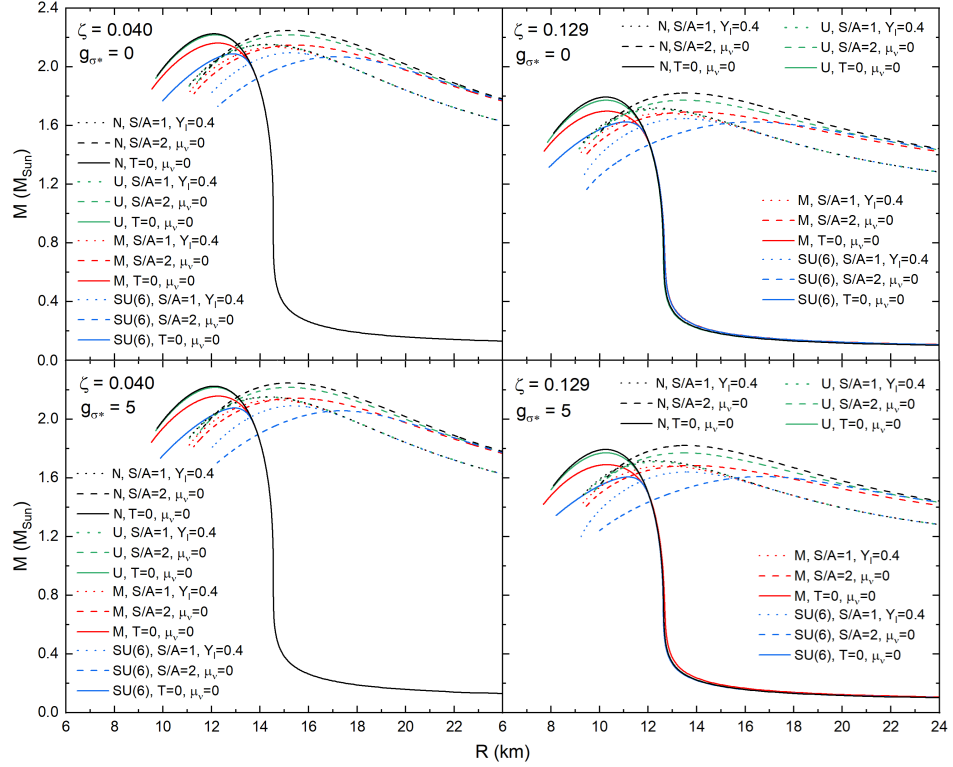


FIG. 18. **SET 1 (Mass-radius diagram):** Gravitational mass ( $M$ ) as a function of radius ( $R$ ) for different proto-neutron star evolution snapshots, particle composition, and hyperon couplings. The different panels show different MBF (left vs. right) and strange scalar meson parameterizations (top vs. bottom).

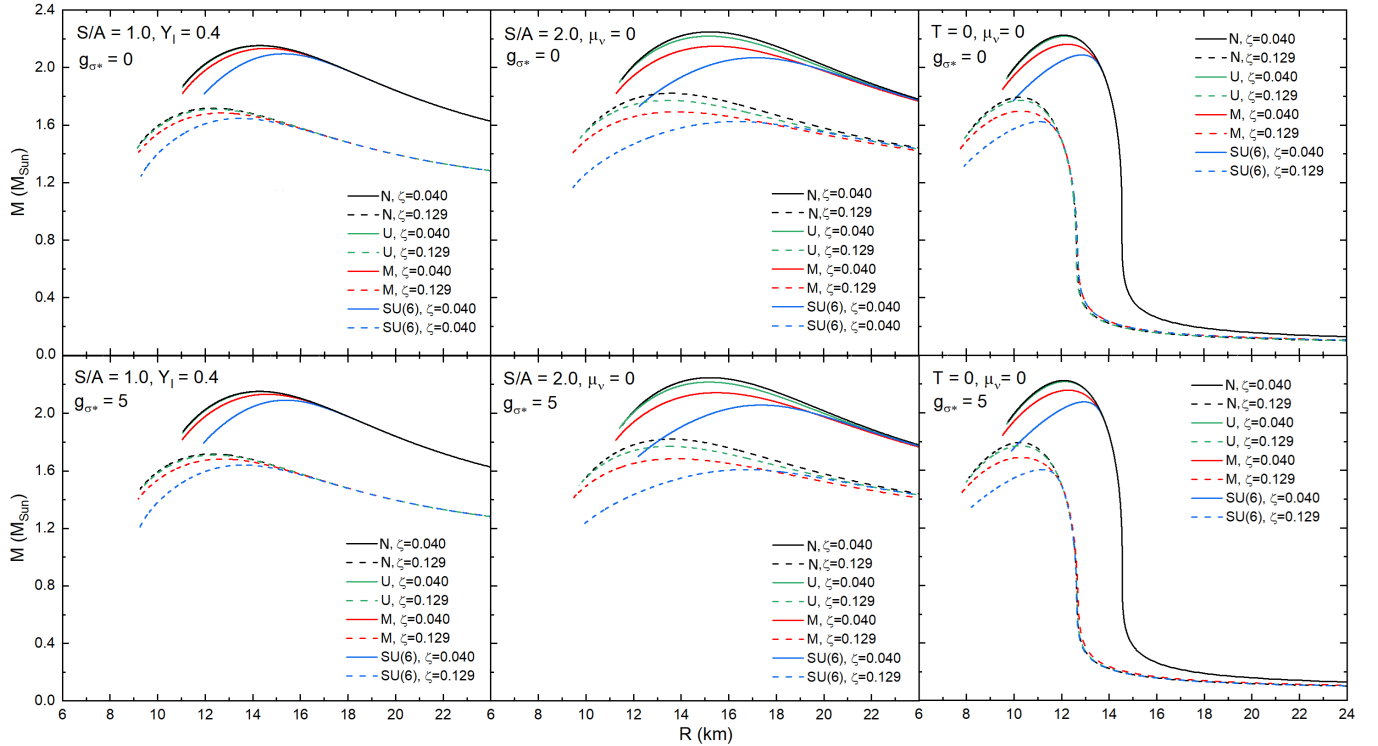


FIG. 19. **SET 2 (Mass-radius diagram):** Same as Fig. 18 but now the different panels show different evolution snapshots (left/center/right) and strange scalar meson parameterizations (top vs. bottom).

TABLE VI. Maximum star mass and the corresponding radius for different configurations of the MBF Model and three scenarios of entropy per baryon ( $S/A$ ). Here,  $N$  stands for pure nucleonic matter. These results consider  $g_{\sigma^*} = 0$ .

S/A	$\zeta$	$SU(6)$	$M$	$U$	$N$
1	0.040	2.10 $M_{\text{Sun}}$	2.13 $M_{\text{Sun}}$	2.15 $M_{\text{Sun}}$	2.15 $M_{\text{Sun}}$
		15.29 km	14.59 km	14.33 km	14.31 km
1	0.129	1.65 $M_{\text{Sun}}$	1.68 $M_{\text{Sun}}$	1.71 $M_{\text{Sun}}$	1.72 $M_{\text{Sun}}$
		13.46 km	12.71 km	12.38 km	12.32 km
2	0.040	2.07 $M_{\text{Sun}}$	2.15 $M_{\text{Sun}}$	2.22 $M_{\text{Sun}}$	2.25 $M_{\text{Sun}}$
		17.15 km	15.52 km	15.17 km	15.22 km
2	0.129	1.62 $M_{\text{Sun}}$	1.69 $M_{\text{Sun}}$	1.77 $M_{\text{Sun}}$	1.82 $M_{\text{Sun}}$
		16.31 km	13.81 km	13.50 km	13.55 km
0	0.040	2.10 $M_{\text{Sun}}$	2.16 $M_{\text{Sun}}$	2.22 $M_{\text{Sun}}$	2.22 $M_{\text{Sun}}$
		12.87 km	12.27 km	12.14 km	12.10 km
0	0.129	1.62 $M_{\text{Sun}}$	1.70 $M_{\text{Sun}}$	1.77 $M_{\text{Sun}}$	1.79 $M_{\text{Sun}}$
		11.08 km	10.30 km	10.26 km	10.25 km

earlier, always below  $2 M_{\text{Sun}}$ . Results for the maximum mass (and the corresponding radii) are shown in Table VI.

Hyperons remain a central agent in shaping the mass-radius curves, especially in the framework of RMF models [136–141]. In our results, this trait can be spotted in Fig. 18. For both  $\zeta$  values, pure nucleonic matter (black curves) yields the largest maximum masses and radii. As hyperonic couplings become weaker – progressing from universal (green) to Moszkowski (red) to  $SU(6)$  (blue) schemes –, the EoS becomes progressively softer, lowering the maximum mass and pushing the curves downward. This hierarchy is most visible in the cold  $T = 0$  case (right panels in Fig. 19), where thermal support is absent and the presence of hyperons can reduce the maximum mass more pronouncedly. For  $S/A = 1$  (left panels in Fig. 19), however, neutrino trapping shifts the onset of hyperons to higher densities, delaying the softening of the EoS. As a result, the differences between the nucleonic and hyperonic curves are somewhat reduced in this regime. In contrast, for  $S/A = 2$  (left panels in Fig. 19) and especially for  $T = 0$ , hyperons appear earlier, and the differences among the coupling schemes become more pronounced.

An important structural characteristic is the behavior of the curves beyond their maximum mass points. The steep vertical drop seen in each set of curves signals the approach to the radial instability predicted by the Tolman–Oppenheimer–Volkoff equations. The density at which this instability sets in depends sensitively on both  $\zeta$  and the hyperon prescription. In models with strong softening—such as  $SU(6)$  couplings combined with  $\zeta = 0.129$ , the star becomes unstable at comparatively low central densities, severely limiting the maximum attainable mass (right panels in Fig. 18). This reinforces the idea that hyperons, without additional repulsive interactions, naturally tend to reduce the maximum mass of NSs.

The thermal snapshots shown in Fig. 19 reflect the

evolutionary sequence of a PNS. The  $S/A = 1$  configuration with trapped neutrinos corresponds to an early stage immediately after core bounce, with relatively large radii ( $\sim 12 - 15$  km). The  $S/A = 2$  case, representing a later stage after partial deleptonization, exhibits increased thermal support and larger radii ( $\sim 14 - 17$  km). Finally, the  $T = 0$  panel depicts the long-term cold NS, whose maximum mass is similar to the previous cases with smaller radii ( $\sim 10 - 13$  km).

Furthermore, just as in the calculations of the basic properties of nuclear matter, a comparison between the upper and lower panels of Figs. 18 and 19 reveals that, in the framework of the MBF Model, the presence of the strange scalar meson  $g_{\sigma^*}$  has a very subtle effect on the global properties of NS and PNS.

In summary, these mass-radius relations capture in a single set of plots the essential physical mechanisms governing neutron-star structure: the competition between thermal pressure and degeneracy pressure, the role of neutrino trapping in delaying hyperonization, the softening induced by hyperons, and the systematic influence of the adjustable parameter  $\zeta$ . The complementary use of fixed- $\zeta$  and fixed-entropy panels provides both a structural overview and a dynamic, evolutionary interpretation of proto-neutron-star matter within the MBF Model.

Finally, Fig. 20 presents a comparison of our results for  $T = 0$  with the astrophysical constraints on the mass-radius relation provided by NICER and LIGO/Virgo measurements (worth to note that NICER data and, in principle, LIGO/Virgo data are valid for cold NSs, without trapped neutrinos).

Since 2010, several NSs with masses exceeding  $2 M_{\text{Sun}}$  have been observed. Two pioneering observations are those of PSR J1614-2230, with a mass of  $1.97 \pm 0.04 M_{\text{Sun}}$  [143] and an estimated radius of  $13 \pm 2$  km [144], and PSR J0348+0432, with a mass of  $2.01 \pm 0.04 M_{\text{Sun}}$  [112] and an estimated radius of  $12.07$  km [139]. A significant milestone was the observation of PSR J0740+6620, the heaviest NICER pulsar, with a mass of  $2.08 \pm 0.07 M_{\text{Sun}}$  [113] and an estimated radius of  $13_{-0.98}^{+1.30}$  km [145], which was the record holder for the heaviest NS until 2022, when the title was taken by PSR J0952-0607 with a reported mass of  $2.35 \pm 0.17 M_{\text{Sun}}$  [146] and an estimated radius of  $12.39_{-0.98}^{+1.30}$  km [147]. It is also important to record, at the other extreme, the lightest pulsar observed by the NICER telescope: PSR J0030+0451, with a mass of  $1.44 \pm 0.14 M_{\text{Sun}}$  and an estimated radius of  $13.02_{-1.06}^{+1.24}$  km [33, 34].

Another relevant source of data for the mass-radius relation is the a gravitational wave event GW170817 observed by the LIGO and Virgo detectors in 2017 [35]. The wave was produced by the last moments of the inspiral of a binary pair of neutron stars, ending with their merger. Combining these observations with a quasi-universal relation between the maximum mass of nonrotating stellar models and the maximum mass that can be supported through uniform rotation, the neutron-star mass  $M$  was estimated to be in the range  $2.01_{-0.04}^{+0.04} M_{\text{Sun}} \leq M \lesssim$

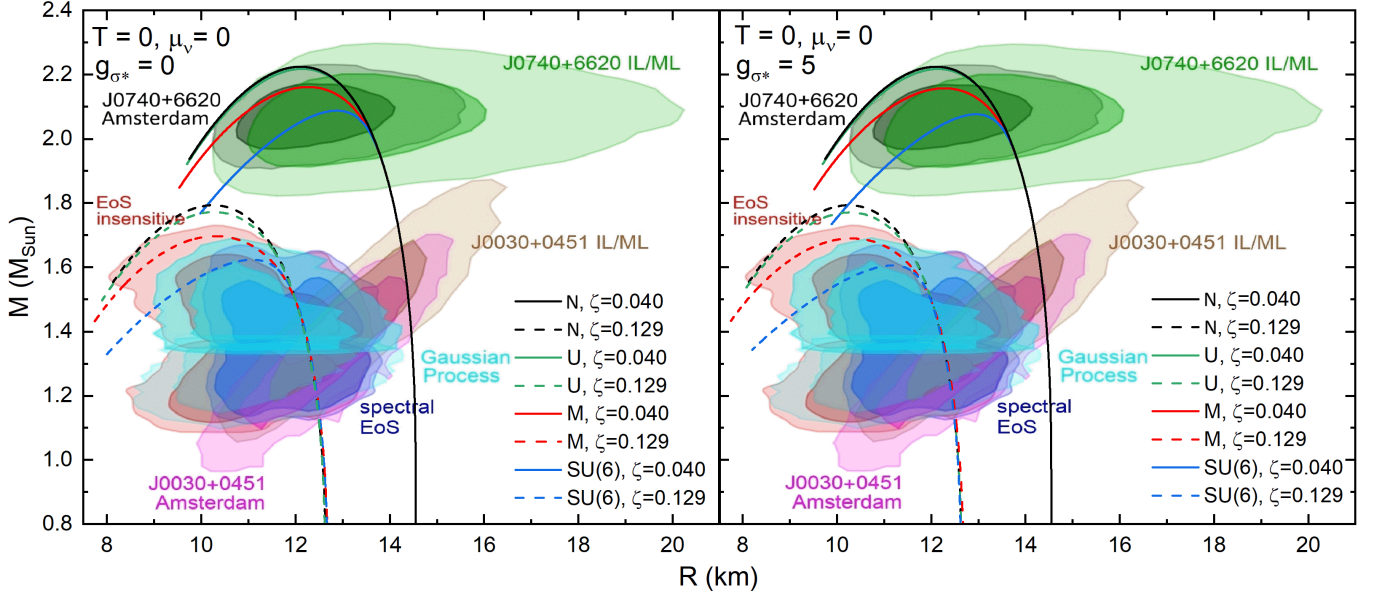


FIG. 20. Mass-radius diagram predicted by the MBF Model for fully evolved NSs, compared with multimessenger observational constraints. Solid and dashed curves represent, respectively, the  $\zeta = 0.040$  and  $\zeta = 0.129$  MBF parameterizations for different configurations (pure nucleonic matter  $N$ , and the  $U$ ,  $M$ , and  $SU(6)$  coupling schemes for hyperons). The different panels show different strange scalar meson parameterizations. The shaded contours in the background, extracted from reference [142], summarize current astrophysical inferences: NICER measurements for PSR J0030+0451 (brown) and PSR J0740+6620 (green) from both the Amsterdam and Illinois/Maryland groups; the EoS-insensitive constraints from GW170817 (old pink); the spectral-EoS constraints (dark blue); and the Gaussian Process reconstruction combining GW170817 and heavy-pulsar mass measurements (light blue). All contours show the 68% and 95% confidence regions.

$2.16^{+0.17}_{-0.15} M_{\text{Sun}}$  [36]. In reference [148], tidal deformabilities and masses of GW170817 were used to infer the radii of the objects in the binary system, adopting a spectral parameterization for the EoS, leading to  $11.9 \pm 1.4$  km. An alternative approach follows the procedure of reference [149] and uses an EoS that is insensitive to the dependence between the tidal deformability and the mass-radius relation, leading to inferred radii of  $10.8^{+2.0}_{-1.7}$  km and  $10.7^{+2.1}_{-1.5}$  km. In this calculation, uncertainty in the EoS-insensitive relation was modeled as Gaussian white noise in the relation. A different EoS-insensitive relation was used in [148] to determine the common neutron-star radius, which was reported as  $10.7^{+2.1}_{-1.6}$  km.

The regions (contours) in the background of Fig. 20, extracted from reference [142], summarize some of these astrophysical data. The universal-relation constraint (EoS-insensitive, colored in old pink) and the spectral-EoS constraint (colored in dark blue) are obtained using GW170817 data. The Gaussian Process constraint (colored in light blue) is obtained by combining GW170817, PSR 1614-2230, PSR 0348+0432, and PSR 0740+6620 (mass only) data. NICER constraints from both the Amsterdam and Illinois/Maryland groups are shown for both J0030+0451 (colored in brown) and J0740+6620 (colored in green). Shaded regions show the 68% and 95% confidence region.

Although these different methods produce posterior distributions for the mass and radius of GW170817 that

look different, they are statistically consistent. Importantly, one cannot simply overlay an EoS mass-radius curve on these contours and decide by eye whether the EoS is ruled out, because every point on the plane (even outside the 68% or 95% regions) still carries nonzero posterior weight; therefore, a proper Bayesian comparison would be required. Nevertheless, even a less rigorous comparison between the curves describing the mass-radius relationship of the MBF model and these contours can serve as a first evaluation of our results.

A closer inspection of Fig. 20 reveals that the configurations with  $\zeta = 0.040$  (solid lines) behave much more favorably in light of the current observational landscape. In particular, all coupling schemes at  $\zeta = 0.040$  yield sequences that comfortably surpass the  $2 M_{\text{Sun}}$  threshold, with both the purely nucleonic and the hyperonic curves reaching maximum masses compatible with (or even slightly exceeding) the region favored by the heaviest NICER pulsar (PSR J0740+6620). These models also intersect the lightest NICER pulsar (PSR J0030+0451) bands in the radius range  $R \simeq 14 - 14.5$  km for canonical stars, indicating that their predictions for intermediate masses remain consistent with the NICER constraints.

For the cases including hyperons, the differences between coupling prescriptions become visibly more pronounced. The  $M$  and  $SU(6)$  schemes at  $\zeta = 0.040$  do reduce the maximum mass relative to the purely nucleonic baseline, but the suppression is moderate enough

that their sequences still lie within the astrophysically preferred region.

In contrast, despite being consistent with the constraints from both GW170817 and the lightest NICER pulsar (PSR J0030+0451), the  $\zeta = 0.129$  curves (dashed lines) exhibit a considerable softening of the EoS, causing the maximum mass to fall well below the observed limits for the heaviest NICER pulsar (PSR J0740+6620) and placing these models in clear tension with present data. This emphasizes that the hyperonic sector of the MBF Model is highly sensitive to both the choice of coupling scheme and the value of  $\zeta$ , reinforcing the need for a controlled treatment of many-body effects when modeling dense baryonic matter.

Moreover, we note that for all parameterizations the predicted radii of low-mass stars lie within the wide NICER contours for PSR J0030+0451, while the high-mass end of the mass-radius curve serves as the most stringent discriminator among the models. Taken together, these comparisons indicate that the MBF Model with  $\zeta = 0.040$  provides a better overall agreement with current observational constraints, whereas the softer  $\zeta = 0.129$  configurations are strongly disfavored, especially when hyperons are present.

It is always pertinent to remind that, depending on our choices for the adjustable parameter  $\zeta$  and the meson-hyperon coupling scheme, the MBF Model has enough flexibility to reproduce a variety of EOSs and, consequently, fit many different mass-radius curves between the blue dashed lines ( $\zeta = 0.129$  with  $SU(6)$  coupling) and the black dashed lines ( $\zeta = 0.040$  for pure nucleonic matter) in Fig. 20. In particular, the MBF Model proves capable of passing the test posed by the so-called *hyperon puzzle*, i.e., the challenge to reconcile these measurements of neutron-star masses above  $2 M_{\text{Sun}}$  with the presence of hyperons [150].

This analysis thus highlights both the predictive capability of the MBF framework and the constraining power of modern multimessenger observations in probing the microphysics of dense matter.

## V. SUMMARY AND OUTLOOK

In this work we have carried out a comprehensive extension of the RMF effective model known as MBF Model, applying it for the first time to study finite-temperature matter and different hyperon-meson coupling prescriptions within the same theoretical framework. This allowed us to investigate in a unified manner how the characteristic parameterizations of the model (representing many-body interactions), thermal effects and hyperonic interactions modify the microscopic and macroscopic properties of dense baryonic matter relevant for neutron-star physics.

We constructed equations of state for both nucleonic and hyperonic compositions of dense matter at finite temperature and examined their thermodynamic behavior in

detail. From these EoSs we evaluated several quantities of central importance for hot and dense matter: the speed of sound, the compressibility, and the adiabatic index, all of which encode the stiffness of the underlying interaction and the response of matter under compression. These calculations corroborate that the MBF Model is useful for constructing a variety of EoSs within the phenomenological range, from the stiffest ( $\zeta = 0.040$ ) to the softest ( $\zeta = 0.129$ ). In the presence of hyperons, the coupling scheme adopted has significant impact on the stiffness of the EoS; namely, the universal coupling scheme ( $U$ ) provides stiffer equations of state, while the  $SU(6)$  coupling scheme gives the softest; moreover, hadronic matter in the universal coupling scheme ( $U$ ) and plain nuclear matter (without hyperons) present similar behavior in all these quantities. In all cases examined, the adiabatic index is always above the limit for stability, and the results for the speed of sound show that the MBF Model strictly respects causality, even in the presence of strong vector interactions. Additionally, these three quantities (speed of sound, compressibility, and adiabatic index) exhibit peaks and bumps in their dependence on the baryon density, due to the appearance of new hyperon degrees of freedom; nonetheless, these non-monotonic features are softened as temperature increases because, in this case, hyperons are already present at low densities.

The temperature profiles at fixed entropy per baryon were also obtained, illustrating how temperature gradients develop inside the stellar interior and how they depend on the chosen hyperon-meson coupling scheme and on the value of the adjustable parameter  $\zeta$  that governs the many-body interactions in the MBF Model. Here, the differences of behavior between pure nucleonic matter and all the coupling schemes for hyperons are more pronounced. These results demonstrate that, although hyperons tend to soften the EoS, the many-body interactions generated by the MBF Model can counterbalance this effect in a controlled way, particularly for the  $\zeta = 0.040$  parameterization.

The astrophysical consequences of the MBF Model were then explored by solving the Tolman-Oppenheimer-Volkoff (TOV) equations both for cold and hot beta-equilibrated matter. For cold neutron stars, while the  $\zeta = 0.129$  parameterization reproduces general radius trends from multimessenger observations, it fails to sustain the high masses observed in heavy pulsars, especially when hyperons are included (as a matter of fact, the maximum masses for  $\zeta = 0.040$  are  $\sim 25\%$  greater than for  $\zeta = 0.129$ ). The stiffest parameterization  $\zeta = 0.040$ , on the other hand, simultaneously satisfies the mass and radius constraints for both nucleonic and hyperonic compositions, and thus emerges as a phenomenologically viable version of the MBF framework in its current form. Worth it to stress that these two values for  $\zeta$  are the extreme phenomenological values for one standard parameterization of the MBF Model (namely, the scalar version of the model); as a consequence, given a suitable choice of parameters, the MBF Model presents the necessary flexi-

bility to provide virtually any EoS in between and, therefore, adapt itself to reproduce the desired astrophysical constraints.

Regarding the behavior of the TOV solutions at  $T \neq 0$ , the thermal snapshots obtained from our EoSs mimic the evolutionary sequence of a proto-neutron star: configurations with trapped neutrinos and moderate entropy per baryon ( $S/A \simeq 1$ ) exhibit larger radii and are thermally puffed-up compared to their cold counterparts, while higher-entropy snapshots ( $S/A \simeq 2$ ) show even more pronounced thermal support. Neutrino trapping delays hyperonization and therefore tends to stiffen the EoS at early times, partially compensating the softening caused by new degrees of freedom; as a consequence the early (hot) sequences can sustain radii and, in some cases, maximum masses comparable to or even above the cold equilibrium sequence. In short, while the cooling process has a minor impact on the maximum mass predicted across the different parameterizations, the radius decreases  $\sim 25\%$ . These finite-temperature results underline the importance of a self-consistent thermal treatment when connecting proto-neutron-star evolutionary stages to the final cold neutron-star configuration.

Taken together, our results for nuclear matter properties and global stellar properties clarify the interplay between thermal effects, many-body forces, and hyperonic degrees of freedom in determining the structure and stability of dense matter. They also demonstrate the adaptability of the MBF Model to accommodate various scenarios relevant for neutron stars, including those with significant thermal content.

Several extensions of the present study are natural and promising. A first step is the inclusion of the full spin-3/2 baryon decuplet, which may compete with or alter the onset of hyperons at high densities and temperatures. Another important development is the incorporation of thermal mesons in the formalism, i.e., meson fields whose mean value is obtained self-consistently at finite temperature (following the Bose-Einstein distribution), which can significantly influence the EoS in hot environments like binary mergers. Finally, the addition of strong magnetic fields – relevant for magnetars and for post-merger remnants – will allow the MBF Model to address anisotropic pressures, the appearance of oscillatory behavior (de Haas-van Alphen-like) in thermodynamic quantities, and other effects characteristic of magnetized dense matter.

In conclusion, this work establishes the finite temperature, hyperon-inclusive MBF Model as a robust and versatile tool for exploring the thermodynamics and astrophysical manifestations of dense baryon matter. With the extensions outlined above, the model will be equipped to provide an even more complete description of the extreme conditions probed in modern astrophysical observations.

The data presented in this work are available upon request and can be obtained by contacting the corresponding author.

## ACKNOWLEDGMENTS

This work was partially supported by the Department of Energy under grant DE-SC0024700; National Science Foundation under grants MUSES OAC2103680 and NP3M PHY2116686; Coordenação de Aperfeiçoamento de Pessoal de Nível Superior (CAPES) Finance Code 001; Conselho Nacional de Desenvolvimento Científico e Tecnológico (CNPq) under grants 312032/2023-4, 402963/2024-5, and 445182/2024-5; Fundação de Amparo à Pesquisa do Estado do Rio Grande do Sul (FAPERGS) under grant 24/2551-0001285-0; Instituto Nacional de Ciência e Tecnologia - Física Nuclear e Aplicações (INCT - FNA) under grants 464898/2014-5 and 408419/2024-5; and Serrapilheira Institute under grant Serra2211-42230. We wish to thank the following researchers, for offering comments, suggestions and encouragement throughout the making of this work: Germán Lugones, Sidney dos Santos Avancini, Dyana Cristine Duarte, Marcus Emmanuel Benghi Pinto, Carlos Conde Ocázquez, André da Silva Schneider, Adriana Raduta, and Yuhan Wang. R.L.S.F. and R.B.J. acknowledge the kind hospitality of the Center for Nuclear Research at Kent State University, where part of this work was done.

## Appendix A: Limits of the MBF Model

In this appendix, we demonstrate how the MBF model reduces to the Walecka and ZM models for specific choices of the adjustable parameters.

Although the meson–baryon interaction in Eq. (4) is written in a form that resembles a minimal Yukawa coupling, the field-dependent parameters  $\Pi_{\lambda b}$  encode a non-minimal structure that can be made explicit by a suitable redefinition of the baryon fields. In this sense, the MBF Model realizes a generalized derivative coupling between meson fields and baryonic currents, in the spirit of the original proposal by Zimányi and Moszkowski [15]. To illustrate this point, let us focus on the Lagrangian density for each baryon species  $b$ , which, according to (4) and (5), can be written as:

$$\mathcal{L}_b = \bar{\psi}_b \left[ \gamma_\mu \left( i\partial^\mu - \Pi_{\xi b} g_{\omega b} \omega^\mu - \Pi_{\eta b} g_{\phi b} \phi^\mu - \frac{1}{2} \Pi_{\kappa b} g_{\varrho b} \boldsymbol{\tau} \cdot \boldsymbol{\varrho}^\mu \right) - \left( m_b - \Pi_{\zeta b} g_{\sigma b} \sigma - \Pi_{\zeta b} g_{\sigma^* b} \sigma^* - \frac{1}{2} \Pi_{\zeta b} g_{\delta b} \boldsymbol{\tau} \cdot \boldsymbol{\delta} \right) \right] \psi_b. \quad (A1)$$

Clearly, in the above expression, a Walecka-like model (with minimal coupling) is obtained by setting  $\xi = \kappa = \eta = \zeta = 0$ , which leads to  $\Pi_{\xi b} = \Pi_{\kappa b} = \Pi_{\eta b} = \Pi_{\zeta b} = 1$ . On the other hand, a ZM-like model (with a classical derivative coupling), is obtained by setting  $\xi = \kappa = \eta = 0$

and  $\zeta = 1$ , which gives  $\Pi_{\xi b} = \Pi_{\kappa b} = \Pi_{\eta b} = 1$  and

$$\Pi_{\zeta b} \equiv \Pi_b^{ZM} = \left( 1 + \frac{g_{\sigma b} \sigma + g_{\sigma^* b} \sigma^* + \frac{1}{2} g_{\delta b} \boldsymbol{\tau} \cdot \boldsymbol{\delta}}{m_b} \right)^{-1}. \quad (\text{A2})$$

In this case, the Lagrangian density for each baryon species  $b$ , reads:

$$\mathcal{L}_b^{ZM} = \bar{\psi}_b \left\{ \gamma_\mu \left( i \partial^\mu - g_{\omega b} \omega^\mu - g_{\phi b} \phi^\mu - \frac{1}{2} g_{\varrho b} \boldsymbol{\tau} \cdot \boldsymbol{\varrho}^\mu \right) - \left[ m_b - \Pi_b^{ZM} \left( g_{\sigma b} \sigma + g_{\sigma^* b} \sigma^* + \frac{1}{2} g_{\delta b} \boldsymbol{\tau} \cdot \boldsymbol{\delta} \right) \right] \right\} \psi_b. \quad (\text{A3})$$

By rescaling the baryon field,

$$\psi_b \rightarrow \psi_b / \sqrt{\Pi_b^{ZM}}, \quad (\text{A4})$$

the above Lagrangian density can be rewritten as:

$$\mathcal{L}_b^{ZM} = -\bar{\psi}_b m_b \psi_b + (\Pi_b^{ZM})^{-1} \left( \bar{\psi}_b i \gamma_\mu \partial^\mu \psi_b - g_{\omega b} \bar{\psi}_b \gamma_\mu \psi_b \omega^\mu - g_{\phi b} \bar{\psi}_b \gamma_\mu \psi_b \phi^\mu - \frac{1}{2} g_{\varrho b} \bar{\psi}_b \gamma_\mu \psi_b \boldsymbol{\tau} \cdot \boldsymbol{\varrho}^\mu \right), \quad (\text{A5})$$

which has exactly the same form as the Lagrangian density proposed by Zimanyi and Moszkowski [15], with additional mesons. If  $\Pi_b^{ZM}$  is replaced in this expression, according to (A2), it can be seen that what was essentially done was to replace the minimal Yukawa coupling  $(g_{\sigma b} \sigma + g_{\sigma^* b} \sigma^* + \frac{1}{2} g_{\delta b} \boldsymbol{\tau} \cdot \boldsymbol{\delta}) \bar{\psi}_b \psi_b$  with a derivative coupling  $[(g_{\sigma b} \sigma + g_{\sigma^* b} \sigma^* + \frac{1}{2} g_{\delta b} \boldsymbol{\tau} \cdot \boldsymbol{\delta}) / m_b] \bar{\psi}_b \gamma_\mu \partial^\mu \psi_b$ . Therefore, the MBF Model can be interpreted as a generalized derivative-coupling framework, continuously interpolating between the ZM Model and the standard RMF theory established by Walecka, with the parameter  $\xi$ ,  $\kappa$ ,  $\eta$  and  $\zeta$  controlling the strength and nonlinearity of the effective derivative interaction.

## Appendix B: Calculation of the Coupling Constants

In this appendix, we present the method for determining the coupling constants for the nucleons  $g_\sigma$ ,  $g_\omega$ ,  $g_\varrho$ , and  $g_\delta$  in the MBF Model. This calculation produces the values shown in Table IV. After choosing one specific value for the adjustable parameter  $\zeta$ , the calculation proceeds as follows:

**STEP 1:** At saturation, the cold isospin-symmetric nuclear matter has vanishing pressure [151], and is populated only by nucleons ( $N$ ), not by leptons nor hyperons. Also, due to isospin symmetry, the mean values of the isovector mesons  $\varrho$  and  $\delta$  are zero. Moreover, at  $T = 0$ , the integrals in (41) can be performed analytically, re-

sulting:

$$\begin{aligned} p = & -\frac{1}{2} m_\sigma^2 \sigma_0^2 + \frac{1}{2} m_\omega^2 \omega_0^2 \\ & + \frac{2}{3\pi^2} \left[ \left( \frac{1}{4} (k_F)_0^3 - \frac{3}{8} (m_N^*)_0^2 (k_F)_0 \right) \sqrt{(k_F)_0^2 + (m_N^*)_0^2} \right. \\ & \left. + \frac{3}{8} (m_N^*)_0^4 \ln \left( \frac{(k_F)_0 + \sqrt{(k_F)_0^2 + (m_N^*)_0^2}}{(m_N^*)_0} \right) \right] = 0, \end{aligned} \quad (\text{B1})$$

where  $(k_F)_0$  and  $(m_N^*)_0$  represent, respectively, the Fermi momentum of the nucleons and the effective mass of the nucleons, both at saturation. In this equation, the value of the effective mass at saturation  $(m_N^*)_0$  is written in terms of the constant  $g_\sigma$  and the field  $\sigma_0$ , according to expression (26):

$$(m_N^*)_0 = m_N - \Pi_\zeta g_\sigma \sigma_0, \quad (\text{B2})$$

where  $m_N$  is the rest mass of the nucleon and where the parametric term  $\Pi_\zeta$ , given by (24), has reduced to

$$\Pi_\zeta = \left( 1 + \frac{g_\sigma \sigma_0}{\zeta m_N} \right)^{-\zeta}. \quad (\text{B3})$$

The Fermi momentum  $(k_F)_0$  can be obtained from the experimental value of the saturation density  $n_0$ , after evaluating the integral in expression (36):

$$n_0 = \frac{2(k_F)_0^3}{3\pi^2} \rightarrow (k_F)_0 = \left( \frac{3\pi^2 n_0}{2} \right)^{\frac{1}{3}}. \quad (\text{B4})$$

Furthermore,  $\omega_0$  can be written in terms of the coupling constant  $g_\omega$  using the second equation of motion in (23) and the experimental value of the saturation density  $n_0$ :

$$\omega_0 = \frac{1}{m_\omega^2} g_\omega n_0. \quad (\text{B5})$$

The value  $\varepsilon_0$  of energy density at saturation at  $T = 0$  can be obtained from expressions (38) and (40):

$$\begin{aligned} \varepsilon_0 = & \frac{1}{2} m_\sigma^2 \sigma_0^2 + \frac{1}{2} m_\omega^2 \omega_0^2 \\ & + \frac{2}{\pi^2} \left[ \left( \frac{1}{4} (k_F)_0^3 + \frac{1}{8} (m_N^*)_0^2 (k_F)_0 \right) \sqrt{(k_F)_0^2 + (m_N^*)_0^2} \right. \\ & \left. - \frac{1}{8} (m_N^*)_0^4 \ln \left( \frac{(k_F)_0 + \sqrt{(k_F)_0^2 + (m_N^*)_0^2}}{(m_N^*)_0} \right) \right]. \end{aligned} \quad (\text{B6})$$

In this formula, once again, the substitutions indicated by equations (B4) and (B5) are made, in order to exchange the variables  $(k_F)_0$  and  $\omega_0$  for  $n_0$  and  $g_\omega$ ; furthermore, the value of  $\varepsilon_0$  can be determined by knowing the experimental value of the binding energy per baryon ( $B/A$ ),

the density of nuclear matter at saturation ( $n_0$ ) and the rest mass of the nucleon ( $m_N$ ), according to:

$$\frac{B}{A} = \frac{\varepsilon_0}{n_0} - m_N \rightarrow \varepsilon_0 = n_0(m_N + B/A). \quad (\text{B7})$$

Finally, the third equation of this system is the equation of motion of the scalar field, according to (23):

$$\sigma_0 = \frac{1}{m_\sigma^2} \left[ g_\sigma (\Pi_\zeta) - \frac{g_\sigma^2}{m_N} (\Pi_\zeta)^{\frac{\zeta+1}{\zeta}} \sigma_0 \right] n_s, \quad (\text{B8})$$

where the parametric term  $\Pi_\zeta$  also assumes the simplified form presented in (B3), and the scalar density is determined according to (37):

$$n_s = \frac{1}{\pi^2} \left[ (k_F)_0 (m_N^*)_0 \sqrt{(k_F)_0^2 + (m_N^*)_0^2} \right. \\ \left. - (m_N^*)_0^3 \ln \left( \frac{(k_F)_0 + \sqrt{(k_F)_0^2 + (m_N^*)_0^2}}{(m_N^*)_0} \right) \right], \quad (\text{B9})$$

where, again, the momentum  $(k_F)_0$  is written in terms of the density  $n_0$  using relation (B4).

Thus, (B1), (B6) and (B8) make up a system of three equations and three variables ( $\sigma_0$ ,  $g_\sigma$  and  $g_\omega$ ) that must be solved numerically for each chosen value of the adjustable parameter  $\zeta$  of the scalar (S) version of MBF Model. The values obtained for  $\sigma_0$ ,  $g_\sigma$  and  $g_\omega$  then allow the calculation of the effective mass of the nucleon  $(m_N^*)_0$ , using equation (B2), and also the compressibility for symmetric nuclear matter at saturation  $K_0$ , which (at  $T = 0$ ) is related to the curvature of the EoS by:

$$K_0 = 9n_B^2 \left[ \frac{d^2(\varepsilon/n_B)}{dn_B^2} \right]_{n_B=n_0}. \quad (\text{B10})$$

In the present work, for these calculations, we consider a saturation density  $n_0 = 0.15 \text{ fm}^{-3}$  (in agreement with [122, 152, 153]) and a binding energy per baryon  $B/A = -15.75 \text{ MeV}$  (a value which lies in the range usually adopted in literature, e.g., [32, 154], and not far from the result presented in [155]).

**STEP 2:** In order to determine the coupling constants of the nucleon with respect to the isovector mesons, it is necessary to consider the EoS of cold asymmetric nuclear

matter (still in the absence of leptons) and solve the system of equations of the symmetry energy

$$a_{sym}^0 = \frac{1}{2} \left[ \frac{d^2(\varepsilon/n_B)}{dt^2} \right]_{t=0}, \quad (\text{B11})$$

and its slope

$$L_0 = 3n_0 \left( \frac{da_{sym}}{dn_B} \right)_{n_B=n_0}, \quad (\text{B12})$$

to find the corresponding values of  $(g_\varrho/m_\varrho)$  and  $(g_\delta/m_\delta)$ . In equation (B11), the asymmetry between protons ( $p$ ) and neutrons ( $n$ ) is quantified by  $t = (n_{B_p} - n_{B_n})/n_B$ .

In this context, it is necessary to employ the appropriate relation to describe the asymmetric nuclear matter at saturation, according to (38) and (40):

$$\varepsilon = \frac{1}{2} m_\sigma^2 \sigma_0^2 + \frac{1}{2} m_\omega^2 \omega_0^2 + \frac{1}{2} m_\varrho^2 \varrho_0^3 + \frac{1}{2} m_\delta^2 \delta_0^3 \\ + \frac{1}{\pi^2} \left[ \int_0^{k_{F_n}} dk k^2 \sqrt{k^2 + (m_n^*)^2} \right. \\ \left. + \int_0^{k_{F_p}} dk k^2 \sqrt{k^2 + (m_p^*)^2} \right], \quad (\text{B13})$$

where  $k_{F_n}$  and  $k_{F_p}$  represent, respectively, the Fermi momentum for neutrons and the protons, respectively.

Thus, equations (B11) and (B12), together with the equations of motion of the fields  $\varrho_0^3$  and  $\delta_0^3$ , given by the equations of motion (23), combine into a system of four equations to be solved for the variables  $g_\varrho$ ,  $g_\delta$ ,  $\varrho_0^3$  and  $\delta_0^3$ . Note that, within this procedure, the effective masses of the nucleons and the fields  $\sigma_0$  and  $\omega_0$  must be recalculated in this new scenario of asymmetric matter, according to equations (23), taking their interdependence into account. In fact, for each choice of the parameter  $\zeta$ , there will be a new solution, setting the coupling constants, the effective mass of the nucleons and the compressibility as functions of the adjustable parameter in the MBF Model.

Considering the phenomenologically acceptable values for  $(m_N^*)_0$  ([156, 157]),  $K_0$  ([122, 158–163]),  $a_{sym}^0$  ([164–166]) and  $L_0$  ([164, 167, 168]), these two steps allow us to build a map of the meson-nucleon coupling constants. Additionally, due to the rapid convergence of the adjustable parameter (6) to the exponential form shown in (8), the range of values for the adjustable parameter  $\zeta$  is quite narrow, and Table IV presents the coupling constants for different values of  $\zeta$  within the phenomenological range.

---

[1] M. Gell-Mann, A Schematic Model of Baryons and Mesons, *Phys. Lett.* **8**, 214 (1964).

[2] G. Zweig, *An SU(3) model for strong interaction symmetry and its breaking*, Tech. Rep. (CERN, Geneva, 1964).

[3] M. Creutz, *Quarks, Gluons and Lattices* (Oxford University Press, 1983).

[4] O. Philipsen, Lattice calculations at non-zero chemical potential: The QCD phase diagram, PoS **CONFINE-MENT8**, 011 (2008).

[5] P. de Forcrand, Simulating QCD at finite density, PoS **LAT2009**, 010 (2009), arXiv:1005.0539 [hep-lat].

[6] J. Ghiglieri, A. Kurkela, M. Strickland, and A. Vuorinen, Perturbative Thermal QCD: Formalism and Applications, Phys. Rept. **880**, 1 (2020), arXiv:2002.10188 [hep-ph].

[7] N. Haque, A. Bandyopadhyay, J. O. Andersen, M. G. Mustafa, M. Strickland, and N. Su, Three-loop HTLpt thermodynamics at finite temperature and chemical potential, JHEP (05), 027, arXiv:1402.6907 [hep-ph].

[8] T. Gorda, A. Kurkela, R. Paatelainen, S. Säppi, and A. Vuorinen, Soft Interactions in Cold Quark Matter, Phys. Rev. Lett. **127**, 162003 (2021), arXiv:2103.05658 [hep-ph].

[9] M. H. Johnson and E. Teller, Classical field theory of nuclear forces, Phys. Rev. **98**, 783 (1955).

[10] H.-P. Duerr, Relativistic effects in nuclear forces, Phys. Rev. **103**, 469 (1956).

[11] H. Yukawa, On the interaction of elementary particles, Proc. Phys. Math. Soc. Jap. **17**, 48 (1935).

[12] J. D. Walecka, A theory of highly condensed matter, Annals Phys. **83**, 491 (1974).

[13] B. D. Serot and J. D. Walecka, *Advances in Nuclear Physics* (Plenum Press, New York, 1986) v. 16.

[14] J. Boguta and A. R. Bodmer, Relativistic Calculation of Nuclear Matter and the Nuclear Surface, Nucl. Phys. A **292**, 413 (1977).

[15] J. Zimanyi and S. A. Moszkowski, Nuclear equation of state with derivative scalar coupling, Phys. Rev. C **42**, 1416 (1990).

[16] A. Delfino, C. T. Coelho, and M. Malheiro, Relativistic nuclear matter with alternative derivative coupling models, Phys. Rev. C **51**, 2188 (1995).

[17] A. R. Taurines, C. A. Z. Vasconcellos, M. Malheiro, and M. Chiapparini, Neutron stars with parametrized meson couplings, Mod. Phys. Lett. A **15**, 1789 (2000).

[18] A. R. Taurines, C. A. Z. Vasconcellos, M. Malheiro, and M. Chiapparini, Neutron stars in a class of nonlinear relativistic models, Phys. Rev. C **63**, 065801 (2001).

[19] R. C. Duncan and C. Thompson, Formation of Very Strongly Magnetized Neutron Stars: Implications for Gamma-Ray Bursts, Astrophys. J. Lett. **392**, L9 (1992).

[20] C. Thompson and R. C. Duncan, The Soft Gamma Repeaters as Very Strongly Magnetized Neutron Stars. II. Quiescent Neutrino, X-Ray, and Alfvén Wave Emission, Astrophys. J. **473**, 322 (1996).

[21] Q.-H. Peng and H. Tong, The physics of strong magnetic fields in neutron stars, Mon. Not. Roy. Astron. Soc. **378**, 159 (2007), arXiv:0706.0060 [astro-ph].

[22] V. Dexheimer and S. Schramm, Proto-Neutron and Neutron Stars in a Chiral SU(3) Model, Astrophys. J. **683**, 943 (2008), arXiv:0802.1999 [astro-ph].

[23] J. Lattimer, Neutron stars and the nuclear matter equation of state, Annual Review of Nuclear and Particle Science **71**, 433 (2021).

[24] G. Baym, H. A. Bethe, and C. J. Pethick, Neutron star matter, Nucl. Phys. A **175**, 225 (1971).

[25] G. Baym, Pion condensation in nuclear and neutron star matter, Phys. Rev. Lett. **30**, 1340 (1973).

[26] D. B. Kaplan and A. E. Nelson, Strange Goings on in Dense Nucleonic Matter, Phys. Lett. B **175**, 57 (1986).

[27] A. G. Cameron, Neutron Star Models., Astrophys. J. **130**, 884 (1959).

[28] V. A. Ambartsumyan and G. S. Saakyan, The Degen-  
erate Superdense Gas of Elementary Particles, Sov. Astron. **4**, 187 (1960).

[29] D. D. Ivanenko and D. F. Kurdgelaidze, Hypothesis concerning quark stars, Astrophysics **1**, 251 (1965).

[30] N. Itoh, Hydrostatic Equilibrium of Hypothetical Quark Stars, Prog. Theor. Phys. **44**, 291 (1970).

[31] K. Fukushima and T. Hatsuda, The phase diagram of dense qcd, Reports on Progress in Physics **74**, 014001 (2010).

[32] N. K. Glendenning, *Compact stars: nuclear physics, particle physics and general relativity* (Springer-Verlag, New York, 2000).

[33] T. E. Riley *et al.*, A *NICER* View of PSR J0030+0451: Millisecond Pulsar Parameter Estimation, Astrophys. J. Lett. **887**, L21 (2019), arXiv:1912.05702 [astro-ph.HE].

[34] M. C. Miller *et al.*, PSR J0030+0451 Mass and Radius from *NICER* Data and Implications for the Properties of Neutron Star Matter, Astrophys. J. Lett. **887**, L24 (2019), arXiv:1912.05705 [astro-ph.HE].

[35] B. P. Abbott *et al.* (LIGO Scientific, Virgo), GW170817: Observation of Gravitational Waves from a Binary Neutron Star Inspiral, Phys. Rev. Lett. **119**, 161101 (2017), arXiv:1710.05832 [gr-qc].

[36] L. Rezzolla, E. R. Most, and L. R. Weih, Using gravitational-wave observations and quasi-universal relations to constrain the maximum mass of neutron stars, Astrophys. J. Lett. **852**, L25 (2018), arXiv:1711.00314 [astro-ph.HE].

[37] W. Koepf, M. M. Sharma, and P. Ring, Scalar coupling in relativistic mean field theory and properties of nuclei and nuclear matter, Nucl. Phys. A **533**, 95 (1991).

[38] V. A. Dexheimer, C. A. Z. Vasconcellos, and B. E. J. Bodmann, On the Density Dependent Nuclear Matter Compressibility, Phys. Rev. C **77**, 065803 (2008), arXiv:0708.0131 [astro-ph].

[39] R. O. Gomes, V. Dexheimer, S. Schramm, and C. A. Z. Vasconcellos, Many-body forces in the equation of state of hyperonic matter, Astrophys. J. **808**, 8 (2015), arXiv:1411.4875 [astro-ph.SR].

[40] R. B. Jacobsen, C. A. Z. Vasconcellos, B. E. J. Bodmann, and F. Fernandez, Quark-Gluon Plasma in Neutron Stars, in *3rd International Workshop on Astronomy and Relativistic Astrophysics* (2010) pp. 55–59.

[41] R. O. Gomes, B. Franzon, V. Dexheimer, and S. Schramm, Many-body forces in magnetic neutron stars, Astrophys. J. **850**, 20 (2017), arXiv:1709.01017 [nucl-th].

[42] S. Navas *et al.* (Particle Data Group), Review of particle physics, Phys. Rev. D **110**, 030001 (2024).

[43] J. R. Pelaez, From controversy to precision on the sigma meson: a review on the status of the non-ordinary  $f_0(500)$  resonance, Phys. Rept. **658**, 1 (2016), arXiv:1510.00653 [hep-ph].

[44] C. Fuchs, H. Lenske, and H. H. Wolter, Density dependent hadron field theory, Phys. Rev. C **52**, 3043 (1995), arXiv:nucl-th/9507044.

[45] S. Typel and H. H. Wolter, Relativistic mean field calculations with density dependent meson nucleon coupling, Nucl. Phys. A **656**, 331 (1999).

[46] G. Frohberg, K. Maslov, V. Dexheimer, J. Grefa, J. Jahan, C. Ratti, and T. E. Restrepo, Relativistic mean-field model with density- and isospin-density-dependent couplings, arXiv (2025), arXiv:2511.15646 [nucl-th].

[47] K. Huang, J. Hu, Y. Zhang, and H. Shen, Investigation

on the Hyperonic Star in Relativistic Mean-field Model, *Nucl. Phys. Rev.* **39**, 135 (2022), arXiv:2203.12357 [nucl-th].

[48] H.-F. Zhu, G.-Z. Liu, X. Wu, and Y.-F. Yuan, New solution to the hyperon puzzle of neutron stars: Quantum many-body effects, *Phys. Rev. D* 10.1103/gxry-v5h7 (2026).

[49] M. Hempel, V. Dexheimer, S. Schramm, and I. Iosilevskiy, Noncongruence of the nuclear liquid-gas and deconfinement phase transitions, *Phys. Rev. C* **88**, 014906 (2013), arXiv:1302.2835 [nucl-th].

[50] J. W. Negele, Nuclear mean-field theory, *Phys. Today*; (United States) **38**:4, 10.1063/1.881019 (1985).

[51] S. A. Moszkowski, Energy of neutron-star matter, *Phys. Rev. D* **9**, 1613 (1974).

[52] C. B. Dover and A. Gal, Hyperon nucleus potentials, *Prog. Part. Nucl. Phys.* **12**, 171 (1985).

[53] J. Schaffner, C. B. Dover, A. Gal, C. Greiner, D. J. Millener, and H. Stoecker, Multiply strange nuclear systems, *Annals Phys.* **235**, 35 (1994).

[54] N. K. Glendenning and S. A. Moszkowski, Reconciliation of neutron star masses and binding of the lambda in hypernuclei, *Phys. Rev. Lett.* **67**, 2414 (1991).

[55] J. Schaffner, H. Stoecker, and C. Greiner, Metastable exotic multihypernuclear objects, *Phys. Rev. C* **46**, 322 (1992).

[56] S. Weissenborn, D. Chatterjee, and J. Schaffner-Bielich, Hyperons and massive neutron stars: the role of hyperon potentials, *Nucl. Phys. A* **881**, 62 (2012), arXiv:1111.6049 [astro-ph.HE].

[57] J. Schaffner and I. N. Mishustin, Hyperon rich matter in neutron stars, *Phys. Rev. C* **53**, 1416 (1996), arXiv:nucl-th/9506011.

[58] P. J. Ellis, R. Knorren, and M. Prakash, Kaon condensation in neutron star matter with hyperons, *Phys. Lett. B* **349**, 11 (1995), arXiv:nucl-th/9502033.

[59] M. Prakash, I. Bombaci, M. Prakash, P. J. Ellis, J. M. Lattimer, and R. Knorren, Composition and structure of protoneutron stars, *Phys. Rept.* **280**, 1 (1997), arXiv:nucl-th/9603042.

[60] J. A. Pons, S. Reddy, M. Prakash, J. M. Lattimer, and J. A. Miralles, Evolution of protoneutron stars, *Astrophys. J.* **513**, 780 (1999), arXiv:astro-ph/9807040.

[61] I. Bednarek and R. Manka, Properties of a protoneutron star in the effective field theory, *Phys. Rev. C* **73**, 045804 (2006), arXiv:nucl-th/0601022.

[62] J. O. Goussard, P. Haensel, and J. L. Zdunik, Rapid differential rotation of protoneutron stars and constraints on radio pulsars periods, *Astron. Astrophys.* **330**, 1005 (1998), arXiv:astro-ph/9711347.

[63] J. A. Pons, S. Reddy, P. J. Ellis, M. Prakash, and J. M. Lattimer, Kaon condensation in proto neutron star matter, *Phys. Rev. C* **62**, 035803 (2000), arXiv:nucl-th/0003008.

[64] V. Dexheimer, D. P. Menezes, and M. Strickland, The influence of strong magnetic fields on proto-quark stars, *J. Phys. G* **41**, 015203 (2014), arXiv:1210.4526 [nucl-th].

[65] D. Kumar, T. Malik, H. Mishra, and C. Providência, Constraints on maximum neutron star mass from protoneutron star evolution, *Phys. Rev. D* **112**, 063042 (2025), arXiv:2505.18888 [nucl-th].

[66] J. R. Stone, V. Dexheimer, P. A. M. Guichon, A. W. Thomas, and S. Typel, Equation of state of hot dense hyperonic matter in the Quark-Meson-Coupling (QMC- A) model, *Mon. Not. Roy. Astron. Soc.* **502**, 3476 (2021), arXiv:1906.11100 [nucl-th].

[67] A. Burrows and J. M. Lattimer, The Birth of Neutron Stars, *Astrophys. J.* **307**, 178 (1986).

[68] T. Fischer, S. C. Whitehouse, A. Mezzacappa, F.-K. Thielemann, and M. Liebendörfer, Protoneutron star evolution and the neutrino-driven wind in general relativistic neutrino radiation hydrodynamics simulations, *Astronomy and Astrophysics* **517**, A80 (2010).

[69] L. Hüdepohl, B. Müller, H.-T. Janka, A. Marek, and G. G. Raffelt, Neutrino Signal of Electron-Capture Supernovae from Core Collapse to Cooling, *Phys. Rev. Lett.* **104**, 251101 (2010), arXiv:0912.0260 [astro-ph.SR].

[70] B. Peres, M. Oertel, and J. Novak, Influence of pions and hyperons on stellar black hole formation, *Phys. Rev. D* **87**, 043006 (2013).

[71] M. Hempel, O. Heinemann, A. Yudin, I. Iosilevskiy, M. Liebendörfer, and F.-K. Thielemann, Hot third family of compact stars and the possibility of core-collapse supernova explosions, *Phys. Rev. D* **94**, 103001 (2016), arXiv:1511.06551 [nucl-th].

[72] J. Roark, X. Du, C. Constantinou, V. Dexheimer, A. W. Steiner, and J. R. Stone, Hyperons and quarks in protoneutron stars, *Mon. Not. Roy. Astron. Soc.* **486**, 5441 (2019), arXiv:1812.08157 [astro-ph.HE].

[73] A. Shrivastava, P. Char, S. Gautam, and S. Banik, Systematic study of scalar, vector, and mixed density dependencies in relativistic mean-field descriptions of hyperonic matter in neutron stars (2025), arXiv:2511.01505 [nucl-th].

[74] S. Balberg, I. Lichtenstadt, and G. B. Cook, Roles of hyperons in neutron stars, *Astrophys. J. Suppl.* **121**, 515 (1999), arXiv:astro-ph/9810361.

[75] N. K. Glendenning, Neutron stars are giant hypernuclei?, *Astrophysical Journal* **293**, 470 (1985).

[76] R. J. Furnstahl, B. D. Serot, and H. Tang, A chiral effective lagrangian for nuclei, *Nuclear Physics A* **615**, 441 (1997).

[77] F. J. Fattoyev and C. J. Horowitz, Relativistic effective interaction for nuclei, giant resonances, and neutron stars, *Physical Review C* **82**, 055803 (2010).

[78] S. Kunkel, S. Wystub, and J. Schaffner-Bielich, Determining the minimal mass of a proto-neutron star with chirally constrained nuclear equations of state, *Phys. Rev. C* **111**, 035807 (2025), arXiv:2411.14930 [nucl-th].

[79] A. E. B. Pasqualotto, R. L. S. Farias, W. R. Tavares, S. S. Avancini, and G. Krein, Causality violation and the speed of sound of hot and dense quark matter in the Nambu–Jona-Lasinio model, *Phys. Rev. D* **107**, 096017 (2023), arXiv:2301.10721 [hep-ph].

[80] M. Dutra, O. Loureco, and D. P. Menezes, Stellar properties and nuclear matter constraints, *Phys. Rev. C* **93**, 025806 (2016), [Erratum: *Phys. Rev. C* 94, 049901 (2016)], arXiv:1510.02060 [astro-ph.HE].

[81] L. McLerran and S. Reddy, Quarkyonic Matter and Neutron Stars, *Phys. Rev. Lett.* **122**, 122701 (2019), arXiv:1811.12503 [nucl-th].

[82] P. Bedaque and A. W. Steiner, Sound velocity bound and neutron stars, *Phys. Rev. Lett.* **114**, 031103 (2015).

[83] E. Annala, T. Gorda, A. Kurkela, J. Nättilä, and A. Vuorinen, Evidence for quark-matter cores in massive neutron stars, *Nature Phys.* **16**, 907 (2020), arXiv:1903.09121 [astro-ph.HE].

[84] M. Ferreira, R. Câmara Pereira, and C. Providência, Quark matter in light neutron stars, *Phys. Rev. D* **102**, 083030 (2020), arXiv:2008.12563 [nucl-th].

[85] P. Jakobus, A. Motornenko, R. O. Gomes, J. Steinheimer, and H. Stoecker, The possibility of twin star solutions in a model based on lattice QCD thermodynamics, *Eur. Phys. J. C* **81**, 41 (2021), arXiv:2004.07026 [nucl-th].

[86] A. Zacchi and J. Schaffner-Bielich, Implications of the fermion vacuum term in the extended SU(3) quark meson model on compact star properties, *Phys. Rev. D* **100**, 123024 (2019), arXiv:1909.12071 [nucl-th].

[87] T. Zhao and J. M. Lattimer, Quarkyonic Matter Equation of State in Beta-Equilibrium, *Phys. Rev. D* **102**, 023021 (2020), arXiv:2004.08293 [astro-ph.HE].

[88] T. Minamikawa, T. Kojo, and M. Harada, Quark-hadron crossover equations of state for neutron stars: constraining the chiral invariant mass in a parity doublet model, *Phys. Rev. C* **103**, 045205 (2021), arXiv:2011.13684 [nucl-th].

[89] M. Hippert, E. S. Fraga, and J. Noronha, Insights on the peak in the speed of sound of ultradense matter, *Phys. Rev. D* **104**, 034011 (2021), arXiv:2105.04535 [nucl-th].

[90] R. D. Pisarski, Remarks on nuclear matter: How an  $\omega_0$  condensate can spike the speed of sound, and a model of  $Z(3)$  baryons, *Phys. Rev. D* **103**, L071504 (2021), arXiv:2101.05813 [nucl-th].

[91] J. I. Kapusta and T. Welle, Neutron stars with a crossover equation of state, *Phys. Rev. C* **104**, L012801 (2021), arXiv:2103.16633 [nucl-th].

[92] R. Somasundaram and J. Margueron, Impact of massive neutron star radii on the nature of phase transitions in dense matter, *EPL* **138**, 14002 (2022), arXiv:2104.13612 [astro-ph.HE].

[93] G. Malfatti, M. G. Orsaria, I. F. Ranea-Sandoval, G. A. Contrera, and F. Weber, Delta baryons and diquark formation in the cores of neutron stars, *Phys. Rev. D* **102**, 063008 (2020), arXiv:2008.06459 [astro-ph.HE].

[94] S. Sen and L. Sivertsen, Mass and Radius Relations of Quarkyonic Stars Using an Excluded-volume Model, *Astrophys. J.* **915**, 109 (2021), arXiv:2011.04681 [astro-ph.HE].

[95] H. Tan, T. Dore, V. Dexheimer, J. Noronha-Hostler, and N. Yunes, Extreme matter meets extreme gravity: Ultraheavy neutron stars with phase transitions, *Phys. Rev. D* **105**, 023018 (2022), arXiv:2106.03890 [astro-ph.HE].

[96] P. Parui, N. Chaudhuri, P. Roy, and S. Sarkar, Compressibility and speed of sound in magnetized nuclear matter with broken scale invariance, *Phys. Rev. D* **112**, 076027 (2025), arXiv:2509.15700 [nucl-th].

[97] C. Brown, V. Dexheimer, R. B. Jacobsen, and R. Luciano Sonego Farias, Approaching the Conformal Limit of Quark Matter with Different Chemical Potentials, *Symmetry* **16**, 852 (2024), arXiv:2405.01032 [hep-ph].

[98] T. Gorda, A. Kurkela, P. Romatschke, S. Säppi, and A. Vuorinen, Next-to-Next-to-Next-to-Leading Order Pressure of Cold Quark Matter: Leading Logarithm, *Phys. Rev. Lett.* **121**, 202701 (2018), arXiv:1807.04120 [hep-ph].

[99] S. Altiparmak, C. Ecker, and L. Rezzolla, On the Sound Speed in Neutron Stars, *Astrophys. J. Lett.* **939**, L34 (2022), arXiv:2203.14974 [astro-ph.HE].

[100] S. Carignano, L. Lepori, A. Mammarella, M. Mannarelli, and G. Pagliaroli, Scrutinizing the pion condensed phase, *Eur. Phys. J. A* **53**, 35 (2017), arXiv:1610.06097 [hep-ph].

[101] B. S. Lopes, D. C. Duarte, R. L. S. Farias, and R. O. Ramos, Speed of sound peak in isospin qcd: A natural prediction of the medium separation scheme, *Phys. Rev. D* **112**, L091903 (2025).

[102] A. Ayala, B. S. Lopes, R. L. Farias, and L. C. Parra, On the origin of the peak of the sound velocity for isospin imbalanced strongly interacting matter, *Physics Letters B* **864**, 139396 (2025).

[103] A. Ayala, A. Bandyopadhyay, R. L. S. Farias, L. A. Hernández, and J. L. Hernández, Qcd equation of state at finite isospin density from the linear sigma model with quarks: The cold case, *Phys. Rev. D* **107**, 074027 (2023).

[104] S. Hands, S. Kim, and J.-I. Skulander, Deconfinement in dense 2-color QCD, *Eur. Phys. J. C* **48**, 193 (2006), arXiv:hep-lat/0604004.

[105] A. E. B. Pasqualotto, D. C. Duarte, R. L. S. Farias, and R. O. Ramos, Speed of sound peak in two-color dense QCD: confronting effective models with lattice data, arXiv preprint (2025), arXiv:2510.10198 [hep-ph].

[106] F. X. Azeredo, A. E. B. Pasqualotto, B. S. Lopes, D. C. Duarte, and R. L. S. Farias, Violation of the conformal limit at finite density: Insights from effective models and lattice qcd, *Symmetry* **18**, 10.3390/sym18020220 (2026).

[107] J. Margueron, H. Hansen, P. Proust, and G. Chanfray, Quarkyonic stars with isospin-flavor asymmetry, *Phys. Rev. C* **104**, 055803 (2021), arXiv:2103.10209 [nucl-th].

[108] D. C. Duarte, S. Hernandez-Ortiz, K. S. Jeong, and L. D. McLerran, Quarkyonic effective field theory, quark-nucleon duality, and ghosts, *Phys. Rev. D* **104**, L091901 (2021), arXiv:2103.05679 [nucl-th].

[109] C. Ecker, C. Hoyos, N. Jokela, D. Rodríguez Fernández, and A. Vuorinen, Stiff phases in strongly coupled gauge theories with holographic duals, *JHEP* **(11)**, 031, arXiv:1707.00521 [hep-th].

[110] T. Demircik, C. Ecker, and M. Järvinen, Dense and Hot QCD at Strong Coupling, *Phys. Rev. X* **12**, 041012 (2022), arXiv:2112.12157 [hep-ph].

[111] N. Kovensky, A. Poole, and A. Schmitt, Building a realistic neutron star from holography, *Phys. Rev. D* **105**, 034022 (2022), arXiv:2111.03374 [hep-ph].

[112] J. Antoniadis *et al.*, A Massive Pulsar in a Compact Relativistic Binary, *Science* **340**, 6131 (2013), arXiv:1304.6875 [astro-ph.HE].

[113] H. T. Cromartie *et al.* (NANOGrav), Relativistic Shapiro delay measurements of an extremely massive millisecond pulsar, *Nature Astron.* **4**, 72 (2019), arXiv:1904.06759 [astro-ph.HE].

[114] E. Fonseca *et al.*, Refined Mass and Geometric Measurements of the High-mass PSR J0740+6620, *Astrophys. J. Lett.* **915**, L12 (2021), arXiv:2104.00880 [astro-ph.HE].

[115] B. Margalit and B. D. Metzger, Constraining the Maximum Mass of Neutron Stars From Multi-Messenger Observations of GW170817, *Astrophys. J. Lett.* **850**, L19 (2017), arXiv:1710.05938 [astro-ph.HE].

[116] M. Ruiz, S. L. Shapiro, and A. Tsokaros, GW170817, General Relativistic Magnetohydrodynamic Simulations, and the Neutron Star Maximum Mass, *Phys. Rev. D* **97**, 021501 (2018), arXiv:1711.00473 [astro-ph.HE].

[117] M. Shibata, E. Zhou, K. Kiuchi, and S. Fujibayashi,

Constraint on the maximum mass of neutron stars using GW170817 event, Phys. Rev. D **100**, 023015 (2019), arXiv:1905.03656 [astro-ph.HE].

[118] A. Nathanail, E. R. Most, and L. Rezzolla, GW170817 and GW190814: tension on the maximum mass, Astrophys. J. Lett. **908**, L28 (2021), arXiv:2101.01735 [astro-ph.HE].

[119] I. Tews, J. Carlson, S. Gandolfi, and S. Reddy, Constraining the speed of sound inside neutron stars with chiral effective field theory interactions and observations, Astrophys. J. **860**, 149 (2018), arXiv:1801.01923 [nucl-th].

[120] A. R. Raduta, F. Nacu, and M. Oertel, Equations of state for hot neutron stars, Eur. Phys. J. A **57**, 329 (2021), arXiv:2109.00251 [nucl-th].

[121] T. Miyatsu, M.-K. Cheoun, K. Kim, and K. Saito, Equation of state for hyperonic neutron-star matter in SU(3) flavor symmetry, Symmetry **17**, 1872 (2025), arXiv:2509.16559 [nucl-th].

[122] J. P. Blaizot, Nuclear Compressibilities, Phys. Rept. **64**, 171 (1980).

[123] J. Rikovska Stone, J. C. Miller, R. Konciewicz, P. D. Stevenson, and M. R. Strayer, Nuclear matter and neutron-star properties calculated with the Skyrme interaction, Phys. Rev. C **68**, 034324 (2003).

[124] A. Perego, D. Logoteta, D. Radice, S. Bernuzzi, R. Kashyap, A. Das, S. Padamata, and A. Prakash, Probing the Incompressibility of Nuclear Matter at Ultrahigh Density through the Prompt Collapse of Asymmetric Neutron Star Binaries, Phys. Rev. Lett. **129**, 032701 (2022), arXiv:2112.05864 [astro-ph.HE].

[125] A. Akmal, V. R. Pandharipande, and D. G. Ravenhall, Equation of state of nucleon matter and neutron star structure, Phys. Rev. C **58**, 1804 (1998).

[126] N. Chamel and P. Haensel, Physics of Neutron Star Crusts, Living Rev. Rel. **11**, 10 (2008), arXiv:0812.3955 [astro-ph].

[127] R. H. Casali and D. P. Menezes, Adiabatic index of hot and cold compact objects, Brazilian Journal of Physics **40**, 166 (2010).

[128] P. Haensel, K. P. Levenfish, and D. G. Yakovlev, Adiabatic index of dense matter and damping of neutron star pulsations, Astron. Astrophys. **394**, 213 (2002), arXiv:astro-ph/0208078.

[129] S. Chandrasekhar, *Hydrodynamic and hydromagnetic stability* (Oxford-Clarendon Press and New York-Oxford Univ. Press, 1961).

[130] M. Onsi, H. Przysiezniak, and J. M. Pearson, Equation of state of homogeneous nuclear matter and the symmetry coefficient, Phys. Rev. C **50**, 460 (1994).

[131] H. Kochanovski, A. Ramos, and L. Tolos, Finite-temperature equation of state with hyperons, EPJ Web Conf. **274**, 07004 (2022), arXiv:2211.04855 [nucl-th].

[132] R. C. Tolman, Static solutions of Einstein's field equations for spheres of fluid, Phys. Rev. **55**, 364 (1939).

[133] J. R. Oppenheimer and G. M. Volkoff, On massive neutron cores, Phys. Rev. **55**, 374 (1939).

[134] G. Baym, C. Pethick, and P. Sutherland, The ground state of matter at high densities: Equation of state and stellar models., Astrophys. J. 170: No. 2, 299-317(1 Dec 1971). 10.1086/151216 (1970).

[135] J. M. Lattimer and F. Douglas Swesty, A generalized equation of state for hot, dense matter, Nuclear Physics A **535**, 331 (1991).

[136] G. Colucci and A. Sedrakian, Equation of state of hypernuclear matter: tuning hyperon-scalar-meson couplings, J. Phys. Conf. Ser. **496**, 012003 (2014), arXiv:1401.1653 [nucl-th].

[137] M. Oertel, C. Providência, F. Gulminelli, and A. R. Raduta, Hyperons in neutron star matter within relativistic mean-field models, J. Phys. G **42**, 075202 (2015), arXiv:1412.4545 [nucl-th].

[138] X.-F. Zhao, The hyperons in the massive neutron star PSR J0348+0432, Chin. J. Phys. **53**, 6 (2015), arXiv:1712.08854 [nucl-th].

[139] X.-F. Zhao, The properties of the massive neutron star PSR J0348+0432, Int. J. Mod. Phys. D **24**, 1550058 (2015), arXiv:1712.08860 [nucl-th].

[140] X.-F. Zhao, Can the massive neutron star PSR J0348+0432 be a hyperon star?, Acta Phys. Polon. B **48**, 171 (2017), arXiv:1712.08870 [nucl-th].

[141] S. Banik and D. Bandyopadhyay, Dense Matter in Neutron Star: Lessons from GW170817 (2020) pp. 85–94, arXiv:1712.09760 [astro-ph.HE].

[142] R. Kumar *et al.* (MUSES), Theoretical and experimental constraints for the equation of state of dense and hot matter, Living Rev. Rel. **27**, 3 (2024), arXiv:2303.17021 [nucl-th].

[143] P. Demorest, T. Pennucci, S. Ransom, M. S. E. Roberts, and J. W. T. Hessels, A two-solar-mass neutron star measured using Shapiro delay, Nature **467**, 1081–1083 (2010).

[144] P. Demorest, T. Pennucci, S. Ransom, M. Roberts, and J. Hessels, Shapiro Delay Measurement of a Two Solar Mass Neutron Star, Nature **467**, 1081 (2010), arXiv:1010.5788 [astro-ph.HE].

[145] T. E. Riley *et al.*, A NICER View of the Massive Pulsar PSR J0740+6620 Informed by Radio Timing and XMM-Newton Spectroscopy, Astrophys. J. Lett. **918**, L27 (2021), arXiv:2105.06980 [astro-ph.HE].

[146] R. W. Romani, D. Kandel, A. V. Filippenko, T. G. Brink, and W. Zheng, PSR J0952–0607: The Fastest and Heaviest Known Galactic Neutron Star, Astrophys. J. Lett. **934**, L17 (2022), arXiv:2207.05124 [astro-ph.HE].

[147] R. Kumar, M. Kumar, V. Thakur, S. Kumar, P. Kumar, A. Sharma, B. K. Agrawal, and S. K. Dhiman, Observational constraint from the heaviest pulsar PSR J0952-0607 on the equation of state of dense matter in relativistic mean field model, Phys. Rev. C **107**, 055805 (2023), arXiv:2306.05097 [nucl-th].

[148] S. De, D. Finstad, J. M. Lattimer, D. A. Brown, E. Berger, and C. M. Biwer, Tidal deformabilities and radii of neutron stars from the observation of gw170817, Phys. Rev. Lett. **121**, 091102 (2018).

[149] K. Yagi and N. Yunes, Approximate universal relations for neutron stars and quark stars, Physics Reports **681**, 1 (2017), approximate Universal Relations for Neutron Stars and Quark Stars.

[150] D. Chatterjee and I. Vidaña, Do hyperons exist in the interior of neutron stars?, Eur. Phys. J. A **52**, 29 (2016), arXiv:1510.06306 [nucl-th].

[151] N. M. Hugenholtz and L. van Hove, A theorem on the single particle energy in a Fermi gas with interaction, Physica **24**, 363 (1958).

[152] T. Gross-Boelting, C. Fuchs, and A. Faessler, Dirac structure of the nucleus-nucleus potential in heavy ion collisions, Prog. Part. Nucl. Phys. **42**, 65 (1999),

arXiv:nucl-th/9812002.

[153] D. Adhikari *et al.* (PREX), Accurate Determination of the Neutron Skin Thickness of  $^{208}\text{Pb}$  through Parity-Violation in Electron Scattering, *Phys. Rev. Lett.* **126**, 172502 (2021), arXiv:2102.10767 [nucl-ex].

[154] F. Weber, R. Negreiros, P. Rosenfield, and M. Stejner, Pulsars as Astrophysical Laboratories for Nuclear and Particle Physics, *Prog. Part. Nucl. Phys.* **59**, 94 (2007), arXiv:astro-ph/0612054.

[155] W. D. Myers and W. J. Swiatecki, Nuclear masses and deformations, *Nucl. Phys.* **81**, 1 (1966).

[156] C. H. Johnson, D. J. Horen, and C. Mahaux, Unified description of the neutron- Pb-208 mean field between -20 and + 165 MeV from the dispersion relation constraint, *Phys. Rev. C* **36**, 2252 (1987).

[157] M. Jaminon and C. Mahaux, Effective Masses in Relativistic Approaches to the Nucleon Nucleus Mean Field, *Phys. Rev. C* **40**, 354 (1989).

[158] H. Krivine, J. Treiner, and O. Bohigas, Derivation of a fluid-dynamical lagrangian and electric giant resonances, *Nucl. Phys. A* **336**, 155 (1980).

[159] J. R. Stone, N. J. Stone, and S. A. Moszkowski, Incompressibility in finite nuclei and nuclear matter, *Phys. Rev. C* **89**, 044316 (2014), arXiv:1404.0744 [nucl-th].

[160] G. Colo, U. Garg, and H. Sagawa, Symmetry energy from the nuclear collective motion: constraints from dipole, quadrupole, monopole and spin-dipole resonances, *Eur. Phys. J. A* **50**, 26 (2014), arXiv:1309.1572 [nucl-th].

[161] G. Colo, N. Van Giai, J. Meyer, K. Bennaceur, and P. Bonche, Microscopic determination of the nuclear incompressibility within the nonrelativistic framework, *Phys. Rev. C* **70**, 024307 (2004), arXiv:nucl-th/0403086.

[162] B. G. Todd-Rutel and J. Piekarewicz, Neutron-Rich Nuclei and Neutron Stars: A New Accurately Calibrated Interaction for the Study of Neutron-Rich Matter, *Phys. Rev. Lett.* **95**, 122501 (2005), arXiv:nucl-th/0504034.

[163] B. K. Agrawal, S. Shlomo, and V. K. Au, Nuclear matter incompressibility coefficient in relativistic and nonrelativistic microscopic models, *Phys. Rev. C* **68**, 031304 (2003), arXiv:nucl-th/0308042.

[164] M. B. Tsang *et al.*, Constraints on the symmetry energy and neutron skins from experiments and theory, *Phys. Rev. C* **86**, 015803 (2012), arXiv:1204.0466 [nucl-ex].

[165] J. M. Lattimer and Y. Lim, Constraining the Symmetry Parameters of the Nuclear Interaction, *Astrophys. J.* **771**, 51 (2013), arXiv:1203.4286 [nucl-th].

[166] C. J. Horowitz, E. F. Brown, Y. Kim, W. G. Lynch, R. Michaels, A. Ono, J. Piekarewicz, M. B. Tsang, and H. H. Wolter, A way forward in the study of the symmetry energy: experiment, theory, and observation, *J. Phys. G* **41**, 093001 (2014), arXiv:1401.5839 [nucl-th].

[167] B. T. Reed, F. J. Fattoyev, C. J. Horowitz, and J. Piekarewicz, Implications of PREX-2 on the Equation of State of Neutron-Rich Matter, *Phys. Rev. Lett.* **126**, 172503 (2021), arXiv:2101.03193 [nucl-th].

[168] B.-A. Li, P. G. Krastev, D.-H. Wen, and N.-B. Zhang, Towards Understanding Astrophysical Effects of Nuclear Symmetry Energy, *Eur. Phys. J. A* **55**, 117 (2019), arXiv:1905.13175 [nucl-th].